

Fetch-limited, strongly forced wind waves in waters with frazil and grease ice - spectral modelling and satellite observations in an Antarctic coastal polynya

Agnieszka Herman¹ and Katarzyna Bradtke²

¹Polish Academy of Sciences

²University of Gdansk

September 13, 2023

Abstract

Sea ice-waves interactions have been widely studied in the marginal ice zone, at relatively low wind speeds and wave frequencies. Here, we focus on very different conditions typical of coastal polynyas: extremely high wind speeds and locally-generated, short, steep waves. We overview available parameterizations of relevant physical processes (nonlinear wave-wave interactions, energy input by wind, whitecapping and ice-related dissipation) and discuss modifications necessary to adjust them to polynya conditions. We use satellite-derived data and spectral modelling to analyze waves in ten polynya events in the Terra Nova Bay, Antarctica. We estimate the wind-input reduction factor over ice in the wave-energy balance equation at 0.56. By calibrating the model to satellite observations we show that exact treatment of quadruplet wave-wave interactions (as opposed to the default Discrete Interaction Approximation) is necessary to fit the model to data, and that the power $n > 4$ in the sea-ice source term $S_{ice} \sim f^n$ (where f denotes wave frequency) is required to reproduce the observed very strong attenuation in spectral tail in frazil streaks. We use a very-high resolution satellite image of a fragment of one of the polynyas to determine whitecap fraction. We show that there are more than twofold differences in whitecap fraction over ice-free and ice-covered regions, and that the model produces realistic whitecap fractions without any tuning of the whitecapping source term. Finally, we estimate the polynya-area-integrated wind input, energy dissipation due to whitecapping, and whitecap fraction to be on average below 25%, 10% and 30%, respectively, of the corresponding open-water values.

1 **Fetch-limited, strongly forced wind waves in waters**
2 **with frazil and grease ice — spectral modelling and**
3 **satellite observations in an Antarctic coastal polynya**

4 **Agnieszka Herman¹, Katarzyna Bradtke²**

5 ¹Institute of Oceanology, Polish Academy of Sciences, Sopot, Poland
6 ²Faculty of Oceanography and Geography, University of Gdansk, Poland

7 **Key Points:**

- 8 • Spectral wave model tuned to reproduce satellite-derived wave properties (peak
9 period, whitecap fraction) in Terra Nova Bay Polynya.
10 • Frazil streaks in polynyas modify wind waves by reducing whitecapping and en-
11 ergy input from wind and increasing viscous dissipation.
12 • Nonlinear wave–wave interactions are crucial in both ice-covered and ice-free ar-
13 eas.

Corresponding author: Agnieszka Herman, agaherman@iopan.pl

Abstract

Sea ice–waves interactions have been widely studied in the marginal ice zone, at relatively low wind speeds and wave frequencies. Here, we focus on very different conditions typical of coastal polynyas: extremely high wind speeds and locally-generated, short, steep waves. We overview available parameterizations of relevant physical processes (nonlinear wave–wave interactions, energy input by wind, whitecapping and ice-related dissipation) and discuss modifications necessary to adjust them to polynya conditions. We use satellite-derived data and spectral modelling to analyze waves in ten polynya events in the Terra Nova Bay, Antarctica. We estimate the wind-input reduction factor over ice in the wave-energy balance equation at 0.56. By calibrating the model to satellite observations we show that exact treatment of quadruplet wave–wave interactions (as opposed to the default Discrete Interaction Approximation) is necessary to fit the model to data, and that the power $n > 4$ in the sea-ice source term $S_{\text{ice}} \sim f^n$ (where f denotes wave frequency) is required to reproduce the observed very strong attenuation in spectral tail in frazil streaks. We use a very-high resolution satellite image of a fragment of one of the polynyas to determine whitecap fraction. We show that there are more than twofold differences in whitecap fraction over ice-free and ice-covered regions, and that the model produces realistic whitecap fractions without any tuning of the whitecapping source term. Finally, we estimate the polynya-area-integrated wind input, energy dissipation due to whitecapping, and whitecap fraction to be on average below 25%, 10% and 30%, respectively, of the corresponding open-water values.

Plain Language Summary

As ocean waves propagate through areas covered with sea ice, they both affect and are affected by the ice. Until recently, wave–ice interactions have been analyzed in the so-called marginal ice zone (MIZ), the external part of sea ice cover neighboring the open ocean. In this work, we study a largely unexplored case of wave–ice interactions that take place in Antarctic coastal polynyas at extremely high wind speeds (often exceeding 100 kph) and low air temperatures (often below -20°C). These waves are very different from those in the MIZ and therefore allow us to learn new aspects of the physics of wave growth and dissipation in sea ice. In our study we use numerical wave modeling and satellite data analysis, and seek optimal combinations of model settings to reproduce the observations. For example, we determine a scaling factor that describes how the energy input from wind is reduced over polynyas due to the presence of the ice. We also show that sea ice reduces wave breaking – and that the model is able to reproduce this effect. Taken together, our results contribute not only to a better understanding of polynya dynamics, but also to more reliable modeling of waves in sea ice in general.

1 Introduction

Interactions between sea ice and ocean surface waves have been in recent years extensively studied theoretically, observationally and numerically (Squire, 2018, 2020; Liu et al., 2020; Shen, 2022, and references there). Significance of waves–ice interactions for short-term dynamics of sea ice and the upper ocean, and for longer-term evolution of sea ice cover in (sub)polar regions has been demonstrated in a number of studies (e.g., Roach et al., 2018, 2019; Boutin et al., 2020). The main focus of waves-in-ice research has been on attenuation of ocean waves in sea ice, caused by energy-conserving scattering and/or dissipation within and under the ice. Importantly, the evolution of wave energy spectra in sea ice is usually analyzed on a component-by-component basis, that is, attenuation coefficients are estimated from pairs of observed spectra at two different locations separately for individual frequency bins (e.g., Cheng et al., 2017; Stopa, Sutherland, & Ardhuin, 2018; Kohout et al., 2020; Alberello et al., 2022), disregarding energy exchange between spectral components that is crucial for evolution of ocean surface waves in open

64 water (e.g., Holthuijsen, 2007). These empirically determined apparent attenuation co-
 65 efficients are then implemented in spectral wave models (e.g., Collins & Rogers, 2017;
 66 Rogers, 2019). Not surprisingly, measurements made in different ice types (frazil, grease
 67 ice, pancakes, ice floes, etc.) and ice thickness lead to different estimations of those co-
 68 efficients (see Rogers, Meylan, & Kohout, 2018, for an overview). A more serious prob-
 69 lem with this approach is that the apparent attenuation represents not only sea-ice re-
 70 lated scattering and dissipation, but is a net effect of all processes involved, including
 71 wind-wave growth, dissipation unrelated to ice, and nonlinear wave-wave interactions.
 72 Arguably, disentangling sea ice effects from the net attenuation requires a combination
 73 of process-oriented observations and theoretical models capturing the underlying physics.
 74 In spite of some recent progress in this respect (see, e.g., Voermans et al., 2019; Smith
 75 & Thomson, 2019a, 2019b; Herman, 2021), the goal of making the spectral wave mod-
 76 els in sea ice comparably versatile as they are in open water remains a big challenge.

77 In attempts to achieve that goal it is important to collect data from a wide range
 78 of waves-in-ice conditions. At present, a serious limitation is the fact that our understand-
 79 ing of sea ice-waves interactions is based exclusively on data from and models of the marginal
 80 ice zone (MIZ; Dumont, 2022). The focus on the MIZ implies that our observations and
 81 modelling efforts are limited to a certain range of conditions typical for this environment.
 82 In particular, waves in the MIZ tend to have low u_*/c ratios (where u_* denotes the fric-
 83 tion velocity of the wind at the sea surface, and c is wave phase speed; the ratio u_*/c
 84 is an inverse of the wave age). In the MIZ typically $u_*/c \ll 0.1$ for wave frequencies
 85 at and close to the spectral peak. This means that these waves are weakly forced by wind
 86 (Janssen et al., 1989) and, consequently, have low steepness and do not break. As a re-
 87 sult, in the spectral energy balance the wind input and wave breaking terms are domi-
 88 nated by terms representing dissipation and scattering in sea ice. It is noteworthy that
 89 situations deviating from that picture (e.g., those with negative apparent attenuation
 90 indicating dominance of wave growth over dissipation) are often removed from the ob-
 91 servations prior to the analysis (e.g., Cheng et al., 2017).

92 As a step towards broadening the picture and extending wave-ice interactions anal-
 93 yses to a wider range of conditions, we turn our attention towards a setting with features
 94 that in many ways are the opposite of the MIZ-typical conditions described above: coastal
 95 (or latent heat) polynyas during catabatic wind events (Morales Maqueda et al., 2004).
 96 Polynya openings are associated with very high wind speeds, often exceeding $30 \text{ m}\cdot\text{s}^{-1}$,
 97 and advection of very cold and dry continental air masses, resulting in offshore drift of
 98 the ice pack and extremely high ocean-atmosphere turbulent heat and moisture fluxes
 99 (up to $2000 \text{ W}\cdot\text{m}^{-2}$; Guest, 2021a, 2021b). All these factors combined lead to strong tur-
 100 bulance and convective, wind- and wave-induced mixing in the ocean mixed layer (OML;
 101 Herman et al., 2020), and to intense frazil ice formation (Thompson et al., 2020; Nakata
 102 et al., 2021). Crucially for this study, waves in coastal polynyas are young, fetch-limited,
 103 strongly forced ($u_*/c > 0.1$), and therefore short and steep, with a strong tendency to
 104 break. Over most of polynya area, energy input from the wind dominates over the net
 105 dissipation, so that the wave energy grows with offshore distance in spite of increasing
 106 ice concentration. Moreover, the sea surface in polynyas is a complex mosaic of open-
 107 water areas and patches of young (frazil, grease and shuga) ice forming characteristic elon-
 108 gated streaks (Eicken & Lange, 1989; Ciappa & Pietranera, 2013; Hollands & Dierking,
 109 2016; Thompson et al., 2020). The properties of those streaks in one of the most widely
 110 studied Antarctic coastal polynyas, the Terra Nova Bay Polynya (TNBP; Fig. 1), have
 111 been recently analyzed by Bradtke and Herman (2023). One of the findings of this pre-
 112 vious study was a significant slowdown of the observed wave growth in the analyzed polynya
 113 events in comparison to the expected open-water wave growth under given wind condi-
 114 tions, an effect that can be attributed only to wave-ice interactions. Inspired by this find-
 115 ing, in this work we conduct an extensive analysis of wave evolution in a series of TNBP
 116 events, based on the results from Bradtke and Herman (2023), an additional satellite data
 117 source providing information on wave breaking patterns, and spectral wave modelling.

118 The overall influence of frazil streaks on waves and, more generally, on the sea sur-
 119 face properties has been described in several earlier studies based on qualitative visual
 120 observations (e.g., Ciappa & Pietranera, 2013; Hollands & Dierking, 2016; Ackley et al.,
 121 2022). Rapid attenuation of short waves in streaks, attributable to a high bulk viscos-
 122 ity of grease ice, leads to a reduction of surface roughness (and thus wind friction veloc-
 123 ity u_*), decrease of the mean wave steepness, and weakening of wave breaking and white-
 124 cap generation (Ackley et al., 2022), thus reducing the sea spray generation and the spray-
 125 associated component of the ocean-atmosphere turbulent heat flux (Guest, 2021b). The
 126 question how to quantify and parameterize these effects and, crucially, how they influ-
 127 ence the spatial evolution of the polynya wave field – with feedbacks to sea ice thermo-
 128 dynamics and dynamics – remains to be answered. In this study, we make the first at-
 129 tempt at estimating the role of individual source terms in the wave-energy balance in
 130 shaping the polynya wave fields. We use the satellite-derived ice concentration and wave
 131 data from Bradtke and Herman (2023), combined with wind fields from a regional weather
 132 model, to set up and calibrate a spectral wave model of the TNBP, for ten polynya events
 133 from the period 2016–2021. We review the available formulations of the relevant source
 134 terms – wind input, deep-water dissipation, quadruplet wave-wave interactions, and at-
 135 tenuation in sea ice – and seek the combination of model settings that best reproduces
 136 observations. We also discuss the (numerous) uncertainties and limitations of the avail-
 137 able observations and models. In our analysis, we pay particular attention to the influ-
 138 ence of frazil streaks on wave breaking. To this end, we adopted an image filtering tech-
 139 nique for detection of breakers in very-high resolution (0.5 m) visible satellite images of
 140 the sea surface. We then compare the spatial variability of two different, but closely re-
 141 lated variables – the satellite-derived surface area fraction covered by breakers, and the
 142 simulated wave energy dissipation due to whitecapping – and estimate the reduction of
 143 the total (polynya-surface-integrated) energy dissipation due to the presence of sea ice.

144 2 Data Sources and Processing

145 2.1 Ice concentration, wave properties and wind data

146 As mentioned in the introduction, this analysis is based on the data and results of
 147 Bradtke and Herman (2023). From the set of satellite images analyzed there, ten have
 148 been selected for the present study (Table 1, Supplementary Fig. S1), based on their suf-
 149 ficiently large spatial extent (given the images’ resolution of 10 m, no reliable wave in-
 150 formation can be obtained from nearshore areas and from relatively small polynyas due
 151 to too small wavelength-to-pixel-size ratios). The ten images were obtained with two satel-
 152 lite sensors: OLI (Operational Land Imager) and MSI (Multispectral Instrument) on board
 153 Landsat-8 and Sentinel-2 satellites, respectively. All details related to image processing
 154 and analysis can be found in Bradtke and Herman (2023) and are not repeated here. The
 155 data used in this study include, for each polynya, maps of polynya extent, ice concen-
 156 tration A , and peak wavelength L_p (and the corresponding deep-water wave period T_p
 157 and frequency $f_p = T_p^{-1}$). As discussed in Bradtke and Herman (2023), the peak wave-
 158 length, together with wave direction at the spectral peak (not considered here), are two
 159 spectral characteristics that can be robustly determined from visible satellite imagery.
 160 Indisputably, the lack of information on wave heights and the shape of the tails of the
 161 spectra is a serious limitation. However, as the analysis in the following sections will show,
 162 spatial variability of T_p alone provides valuable insight into the properties of the under-
 163 lying wave field and, crucially, constrains the possible combinations of the adjustable pa-
 164 rameters in spectral modelling, thus allowing inferences about individual physical pro-
 165 cesses at play.

166 The results of the Antarctic Mesoscale Prediction System (AMPS; Powers et al.,
 167 2012, <https://www.earthsystemgrid.org/project/amps.html>) are used as a source
 168 of surface atmospheric data. Results from a nested subdomain (the so called Ross Island
 169 grid) are used, with resolution of 1.1 km in 2016 and 0.89 km in 2019–2021. For each

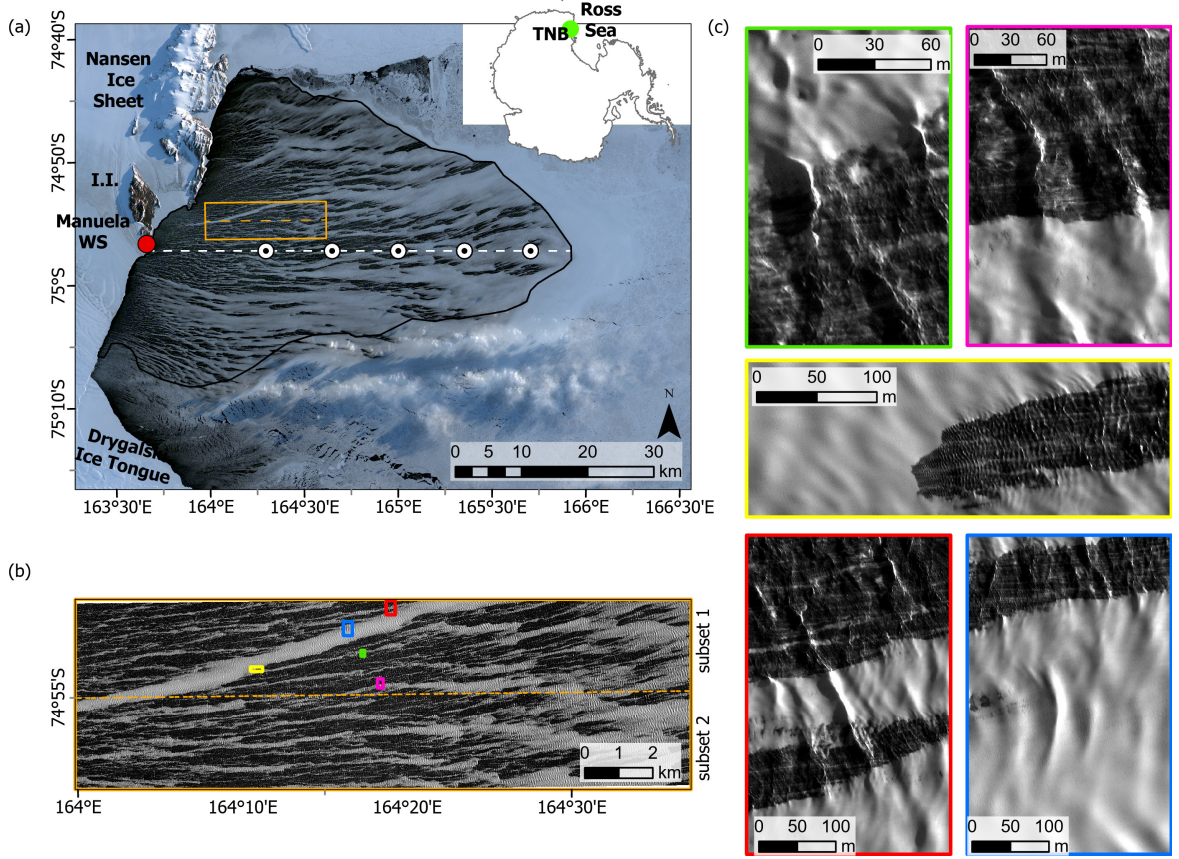


Figure 1. (a) Location of the TNBP and spatial distribution of sea ice on 19 Sep. 2019 on the Sentinel-2 MSI RGB composite (Copernicus Sentinel data 2019); the outline of the polynya and the location of the Manuela weather station on Inexpressible Island (I.I.) are marked with the black polygon and red dot, respectively. The orange rectangle shows extent of the analyzed subsets of WorldView-2 Panchromatic image (imagery © 2019 Maxar Technologies), fragments of which are zoomed in panels (b) and (c). The dashed white line and white dots in (a) show the location of the transect and points at which the results are analyzed in section 4.

Table 1. Summary of polynya events analyzed in this study

Date	Time (UTC)	Sensor	$T_{a,M}$ (°C)	$U_{w,M}$ (m·s ⁻¹)	$\theta_{w,M}$ (degr)	S_p (km ²)	L_e (km)	L_c (km)
2016-10-05	2120	MSI	-22.5	24.1	260	1043	36.2	63.7
2016-10-06	2050	MSI	-24.6	25.4	262	740	40.8	62.3
2016-10-17	2050	OLI	-21.4	28.4	261	1110	33.8	46.7
2016-10-22	2110	MSI	-22.3	21.3	259	975	28.3	46.8
2016-10-24	2100	OLI	-17.4	28.7	257	1762	53.3	55.2
2019-09-19	2100	MSI	-26.5	33.8	258	1920	56.3	50.0
2019-09-29	2110	OLI	-23.4	32.4	250	1729	45.4	57.9
2020-10-19	2100	OLI	-26.2	23.5	261	674	36.2	46.9
2020-10-26	2100	OLI	-20.6	23.3	266	1648	39.5	65.7
2021-10-07	2130	MSI	-23.2	28.1	272	736	35.5	52.2

$T_{a,M}$, $U_{w,M}$, $\theta_{w,M}$ – air temperature, wind speed and direction, respectively, at the Manuela weather station; S_p – polynya surface area; L_e and L_c – polynya extent in cross-shore and along-shore direction, respectively.

170 polynya, 9-hour forecasts from 12 UTC valid for 21 UTC were selected, i.e., the time clos-
 171 est to the acquisition time of the satellite scenes (Table 1). The 2-m AMPS wind vec-
 172 tors were recomputed onto the 10-m height with the algorithm based on the Monin–Obukhov
 173 similarity theory, as described in Guest (2021b). (Note that the measured wind data from
 174 the Manuela weather station in Table 1 are provided for informative purpose only; the
 175 wave modelling is based exclusively on the spatially-variable AMPS wind fields.)

176 2.2 Wave breaking patterns

177 The only additional source of satellite data used here, but not in Bradtke and Her-
 178 man (2023), is a very-high resolution panchromatic (PAN) satellite image taken by the
 179 WorldView-2 (WV2) satellite (imagery © 2019 Maxar Technologies) showing a fragment
 180 of the polynya from 19. Sep. 2019 (see Figs. 1 and 2 for a location and for zoomed frag-
 181 ments). The image was acquired at 21:22 UTC, i.e., 22 minutes after the correspond-
 182 ing MSI image, but considering the stable wind and air temperature forcing on that day
 183 it is reasonable to assume that the wave and sea ice conditions were very similar as well.
 184 We analyze a fragment of the scene taken by the satellite which covers an area of $18.3 \times 5.5 \text{ km}^2$.
 185 We use the standard LV2A product, without atmospheric correction, georeferenced and
 186 resampled to a grid of 0.5-m (the viewing geometry provides effective resolution of 0.53 m)
 187 in UTM zone 58S projection. Due to the small size of the analyzed area and cloudless
 188 sky, it can be assumed that the influence of the atmosphere on the image brightness is
 189 spatially homogeneous. During the satellite overpass the sea surface was illuminated by
 190 the Sun from a direction of 54.1° (azimuth angle) and an elevation angle of 7.7° . With
 191 the predominant direction of wave propagation towards the east (see Supplementary Fig.
 192 S1), this geometry of illumination causes shadowing of the windward slopes of steep waves.
 193 This makes it easier to identify them on a satellite image. However, the limited avail-
 194 ability of light makes it impossible to analyze features occurring in shadowed areas of
 195 open water.

196 As can be seen on the WV2 image (Fig. 2), whitecaps strongly contrast with darker
 197 water, even if the water reflectance is raised by frazil ice. The lighting conditions make
 198 also the very bright crests of steep waves clearly visible against the background of the
 199 frazil streaks. Therefore, in order to detect potential breakers in the analyzed image, we
 200 were looking for sharp contrast between neighboring pixels by applying a moving-window
 201 filter that calculates the sum of differences between a given pixel and the eight nearest
 202 pixels in the directions between 225° and 315° (SW to NW). Initially, the panchromatic
 203 image was de-noised with an edge-preserving filter. Pixels for which the calculated con-
 204 trast value was higher than the image average by more than 3 standard deviations (the
 205 same threshold for the whole image) were identified as sharply contrasted objects. To
 206 limit false alarms, only those objects that met the size criterion (more than 3 pixels con-
 207 nected by sides or corners) and contained bright pixels (the brightness threshold was de-
 208 termined by unsupervised ISODATA classification of the de-noised PAN image) were con-
 209 sidered as potential breakers (Fig. 2). In the next step, the surface area of pixels recog-
 210 nized as breakers was used to calculate whitecap fraction W within $200 \times 200 \text{ m}^2$ grid cells
 211 snapped to the grid of the wave model (see further section 3.3); and zonal fraction W_X
 212 was calculated in vertical zones 200 m wide, oriented perpendicularly to the x_{UTM} axis.
 213 Due to differences in spatial patterns of frazil streaks in the upper and lower parts of the
 214 PAN image, it was divided into 2 subsets (see Fig. 1b) and zonal statistics were calcu-
 215 lated for each of them separately. Finally, ice–water mask derived from WV2 data was
 216 used to calculate whitecap fraction W_X separately for ice-free and ice-covered regions,
 217 respectively.

218 Due to the lack of independent observations that could be used to validate our al-
 219 gorithm, its adjustable parameters have been selected in such a way that, first, the out-
 220 lines of detected breakers (Fig. 2) correspond as close as possible to a visual assessment
 221 by a human observer, and second, if any bias in the results is present, it is towards overde-

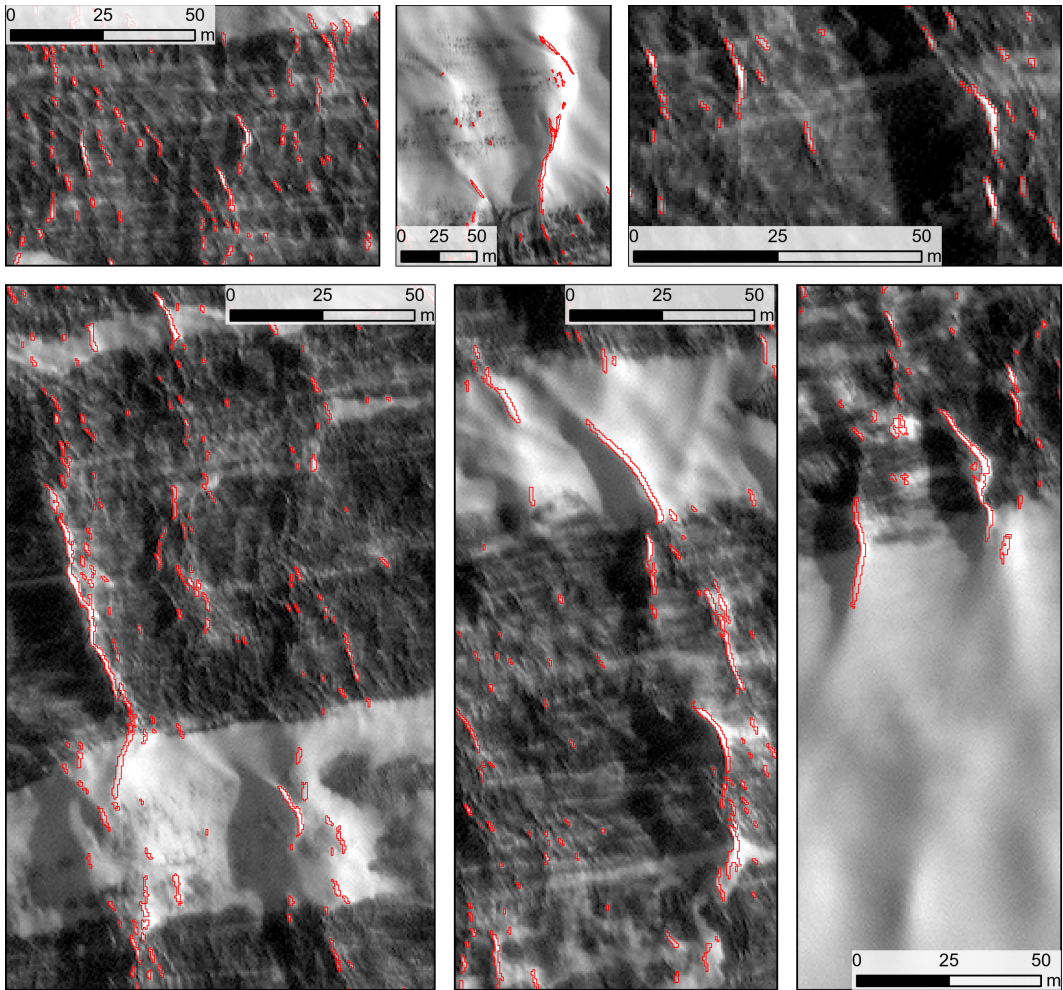


Figure 2. Zoomed fragments of WorldView-2 Panchromatic image (Imagery ©2019 Maxar Technologies) showing variability in pixel brightness due to the presence of frazil ice, waves and effects of their breaking. Outlines of detected breakers are marked in red.

222 tecton in ice and underdetection in water rather than *vice versa*. Thus, in spite of un-
 223 avoidable uncertainties, the differences between ice-covered and ice-free regions can be
 224 treated as reliable and under- rather than overestimated.

225 Image processing and visualization was performed with the Trimble eCognition De-
 226 veloper and ESRI ArcGIS Pro software.

227 3 Spectral Wave Modeling

228 3.1 Definitions and assumptions

229 Let us consider a stationary wave field described by spatially variable wave energy
 230 spectra $E(\mathbf{x}, f, \theta)$, where \mathbf{x} is location in horizontal space, and f, θ are wave frequency
 231 and propagation direction, respectively. Let us further assume that the waves are forced
 232 by time-independent wind with 10-m speed $u_{10}(\mathbf{x})$ and direction $\theta_w(\mathbf{x})$, and that the wa-
 233 ter depth is large, so that refraction, bottom friction and other processes related to wave-

234 bottom interactions can be omitted. The wind-induced, tidal and other currents are omit-
 235 ted as well. Finally, let the sea ice concentration be described by $A(\mathbf{x})$.

236 Under these assumptions, the wave energy conservation equation (e.g., Holthuijsen,
 237 2007) reduces to:

$$\mathbf{c}_g \cdot \nabla E = [1 - A + a_{\text{in}}A]S_{\text{in}} + S_{\text{ds}} + S_{\text{nl}} + AS_{\text{ice}}, \quad (1)$$

238 where $\mathbf{c}_g = c_g[\cos \theta, \sin \theta]$, $c_g = d\sigma/dk$ is the group velocity, and the angular frequency
 239 $\sigma = 2\pi f$ and wave number k fulfill the deep-water dispersion relation $\sigma^2 = gk$, with
 240 g gravitational acceleration. No changes of the dispersion relation due to the presence
 241 of frazil/grease ice are considered here – an assumption consistent with that of a low thick-
 242 ness and low Reynolds number of frazil/grease ice in streaks (e.g., Collins et al., 2017,
 243 note that observations and models of wave dispersion in frazil ice referred to in this and
 244 similar papers are limited to frazil/pancakes mixtures typical for freezing conditions in
 245 the MIZ – ice type that can be found in the outermost regions of polynyas, but not in
 246 their central parts of interest here). The source terms on the right-hand side of (1) de-
 247 scribe energy generation by wind S_{in} , deep-water dissipation S_{ds} , quadruplet wave–wave
 248 interactions S_{nl} , and attenuation by sea ice S_{ice} . As can be seen in (1), S_{ice} is scaled with
 249 ice concentration A . The coefficient $a_{\text{in}} \in [0, 1]$ allows for analogous scaling of S_{in} : the
 250 wind input is unaffected by ice if $a_{\text{in}} = 1$ and it equals zero over ice if $a_{\text{in}} = 0$. The
 251 two remaining source terms, S_{ds} , S_{nl} , are unaffected by the presence of the ice. Justi-
 252 fication for this treatment of source terms is provided below.

253 3.2 Overview of source terms formulations

254 In most spectral wave models (e.g., SWAN, WaveWatchIII, or WAM), several dif-
 255 ferent formulations of each source term in (1) are implemented. Their optimal choice de-
 256 pends on a particular application (domain size, water depth, expected u_*/c ratios, pres-
 257 ence of swell, etc.). Reviewing those formulations is out of the scope of this paper. In-
 258 stead, we concentrate here on selected parameterizations suitable for polynya conditions,
 259 with focus on those available in SWAN (Simulating Waves Nearshore; Booij et al., 1999),
 260 which is the model used in our simulations. Whenever several choices seem adequate,
 261 the more widely used ones (or, preferably, default) are selected.

262 3.2.1 S_{nl}

263 Starting with the S_{nl} term, it is important to recall that the nonlinear wave–wave
 264 interactions are inherently related to the dispersion relation of waves or, more precisely,
 265 to the existence of certain combinations of wavenumber vectors and wave frequencies among
 266 the components of the wave energy spectra (resonance conditions; see, e.g., Holthuijsen,
 267 2007). Therefore, as long as the assumptions made in section 3.1 hold (large water depth
 268 and validity of the open-water dispersion relation in frazil streaks), it is reasonable to
 269 assume that the quadruplet wave–wave interactions remain “active” and can be com-
 270 puted in the same way in ice-covered and ice-free areas (it should be noted, however,
 271 that in different ice types different types of nonlinear interactions may occur, e.g. tri-
 272 ads in fields of large floes in which hydroelastic effects are significant, see, e.g., Deike et
 273 al., 2017).

274 In SWAN and other spectral wave models, the DIA (discrete interaction approx-
 275 imation) by Hasselmann et al. (1985) is the default way of computing S_{nl} . Out of the
 276 very large number of quadruplet combinations in a given energy spectrum, DIA consid-
 277 ers only two quadruplets for each spectral component (see SWAN Team, 2022, for de-
 278 tails of DIA and its implementation in SWAN). Without making premature references
 279 to our model setup and simulations, we remark here that in spite of many attempts, we
 280 were unable to calibrate SWAN to the data when using DIA: the simulated wave peri-
 281 ods were strongly biased in a way that could not be reduced by any reasonable combi-

282 nation of tunable coefficients. Replacing the DIA with the near-exact method (Van Vled-
 283 der, 2006) removed the problems, suggesting that a careful treatment of quadruplet in-
 284 teractions is crucial for reproducing wave growth in polynyas (and in similar settings)
 285 with spectral wave models. This finding is not surprising if one considers the crucial role
 286 of nonlinear wave–wave interactions in modifying waves propagating through oil spills.
 287 Although energy dissipation within the oil layer is limited to very short waves, with fre-
 288 quencies well over 1 Hz (with particularly strong attenuation in the range 3.5–6.8 Hz due
 289 to Marangoni resonance), transfer of energy from lower frequencies to that highly dis-
 290 sipative frequency range by quadruplets leads to a very effective dissipation mechanism,
 291 attenuating waves with frequencies as low as 0.7 Hz (Alpers & Hühnerfuss, 1989; Bene-
 292 tazzo et al., 2019). How relevant similar combinations of processes are for sea ice remains
 293 to be studied. Notably, the importance of nonlinear interactions (combined with wind
 294 input) in reproducing the observed apparent attenuation rates of high-amplitude waves
 295 in the MIZ under storm conditions has been shown by Li et al. (2015).

296 3.2.2 S_{in} and S_{ds}

297 For S_{in} and S_{ds} – the two source terms that are very closely related in spectral wave
 298 models (Holthuijsen, 2007) – the formulation of Van der Westhuijsen et al. (2007) is se-
 299 lected. It combines wind input of Yan (1987) with nonlinear saturation-based whitecap-
 300 ping based on Alves and Banner (2003) and dissipation due to non-breaking waves based
 301 on Komen et al. (1984). Contrary to earlier models of whitecapping, which computed
 302 breaking probability from spectral-mean wave steepness (Komen et al., 1984), the for-
 303 mulation of Alves and Banner (2003) and the modified version of Van der Westhuijsen
 304 et al. (2007) used in SWAN make use of the observed links between wave breaking and
 305 wave groups. Accordingly, the so-called spectral saturation $B(k)$ – a measure of wave
 306 steepness – is computed from directionally-integrated spectrum $\bar{E}(f) \equiv \int_{\theta=0}^{2\pi} E(f, \theta) d\theta$
 307 within narrow frequency bands. Thus, dissipation is local in the wavenumber space. This
 308 is particularly relevant for the present case: it allows for breaking of short, steep, fast-
 309 growing waves in open-water patches between frazil streaks, even if the longer waves at
 310 the peak of the spectrum have milder slopes, so that the spectral-average wave steep-
 311 ness does not exceed the critical value. The older algorithms fail to reproduce this case
 312 of breaking limited to the narrow frequency range of the spectrum. Importantly as well,
 313 although S_{ds} is routinely referred to as the ‘whitecapping source term’, it is in fact sup-
 314 posed to represent all (largely unknown) deep-water dissipation mechanisms, including
 315 turbulence. S_{ds} is thus computed as a weighted sum of two contributions, whitecapping
 316 S_{wc} and dissipation unrelated to wave breaking S_{nbr} :

$$S_{\text{ds}} = f_{\text{br}} S_{\text{wc}} + (1 - f_{\text{br}}) S_{\text{nbr}}, \quad (2)$$

317 where $f_{\text{br}} \in [0, 1]$. For S_{wc} we have:

$$S_{\text{wc}} = -C_{\text{ds}} \left[\frac{B(k)}{B_r} \right]^{p/2} (gk)^{1/2} E(f, \theta), \quad (3)$$

318 where the saturation $B(k) = c_g k^3 \bar{E}(f)$, and C_{ds} , B_r and p are tuning coefficients (see
 319 SWAN Team, 2022, for their treatment in SWAN). Details of calculation of S_{nbr} and f_{br}
 320 can be found in the SWAN documentation. Crucially, in strongly forced, short waves an-
 321 alyzed here, $f_{\text{br}} \simeq 1$ over the whole energy-carrying wave frequency range (f between,
 322 approximately, 0.13 and 0.6 Hz), i.e., both around the peak and in the tail of the spec-
 323 trum (0.13 Hz is the lowest peak frequency found in satellite images analyzed in this study).
 324 Thus, $S_{\text{ds}} \simeq S_{\text{wc}}$. Under different conditions, when $f_{\text{br}} < 1$ and the contribution of
 325 S_{nbr} to S_{ds} is substantial, it might be suitable to multiply S_{nbr} by ice concentration A
 326 in order to turn off S_{nbr} over ice (reflecting the fact that frazil and grease ice suppresses
 327 turbulence due to its large viscosity). In our simulations it did not produce any notice-
 328 able differences in the results.

329 In general, very little is known about wave breaking in frazil and grease ice. As dis-
 330 cussed further in section 4.2 and as can be seen in Figs. 1 and 2, long waves do occasion-
 331 ally break within ice streaks in TNBP, although much less frequently than in the sur-
 332 rounding open water. As in the case of S_{nl} , we may seek analogies with oil slicks, for which
 333 available observations suggest that the oil’s high (and legendary) effectiveness in sup-
 334 pressing wave breaking is a secondary effect of other processes rather than a direct me-
 335 chanical response of the waves to the oil presence (e.g., Cox et al., 2017). For spectral
 336 modelling it means that – provided other source terms are properly computed – the ef-
 337 fect of reduced whitecap dissipation in ice-covered areas should be obtained as a mod-
 338 elling result in spite of S_{wc} being computed in the same way everywhere (note that this
 339 is the default setting in SWAN).

340 As for the wind input term S_{in} , its general form is:

$$S_{\text{in}} = \beta_{\text{in}} E, \quad \text{where} \quad \beta_{\text{in}} \equiv \beta_{\text{in}}(u_*/c, \theta_{\text{rel}}) \quad (4)$$

341 and where θ_{rel} is the angle between wind direction and propagation direction of the given
 342 spectral component. In the model of Yan (1987):

$$\beta_{\text{in}} = \max \left\{ \left[a_1 \left(\frac{u_*}{c} \right)^2 + a_2 \frac{u_*}{c} + a_3 \right] \cos \theta_{\text{rel}} + a_4, 0 \right\}. \quad (5)$$

343 The coefficients used in SWAN (recalibrated from the original ones by Van der West-
 344 huijsen et al., 2007) are: $a_1 = 4.0 \cdot 10^{-2}$, $a_2 = 5.52 \cdot 10^{-3}$, $a_3 = 5.2 \cdot 10^{-5}$, $a_4 = -3.02 \cdot$
 345 10^{-4} . An important advantage of this model is that, contrary to the earlier ones formu-
 346 lated for low wind speeds, it is suitable for strongly forced waves as well. As will be shown
 347 below, in polynyas this condition is fulfilled over most of both geographic and spectral
 348 space (i.e., the majority of polynya surface area, and energy-carrying wave frequency range),
 349 with an exception of the longest waves at the downwind end of the polynya.

350 For a given 10-m wind speed u_{10} , change in S_{in} due to the presence of sea ice may
 351 result from three factors: (i) change of the form of the β_{in} function (5); (ii) change of the
 352 wave phase speed c due to a modified dispersion relation in ice; and (iii) change of u_*
 353 due to a modified roughness of the surface. If we assume that expression (5) remains valid
 354 – to the best of our knowledge there are no data available that could be used to verify
 355 this assumption – and if we keep the assumption made earlier about the dispersion re-
 356 lation in polynyas, the only factor that remains is the surface drag. (Note that the in-
 357 flunce of the dispersion relation in sea ice on wind wave growth has been analyzed by
 358 Zhao & Zhang, 2020)

359 The relationship between u_* and u_{10} is $u_*^2 = C_{\text{D}} u_{10}^2$, where C_{D} is the 10-m drag
 360 coefficient. In spectral wave models, $C_{\text{D}} = C_{\text{Dn}}$, i.e. it represents the neutral drag co-
 361 efficient and it is a function of u_{10} only. The default $C_{\text{Dn}}(u_{10})$ relationship used in SWAN
 362 is by Zijlema et al. (2012), which reproduces the observed drop of surface drag at very
 363 high wind speeds (Janssen & Bidlot, 2023):

$$C_{\text{Dn}} = (0.55 + 2.97\tilde{u} - 1.49\tilde{u}^2) \cdot 10^{-3}, \quad \text{where} \quad \tilde{u} = u_{10}/u_{\text{ref}} \quad (6)$$

364 and $u_{\text{ref}} = 31.5 \text{ m}\cdot\text{s}^{-1}$ is a reference wind speed at which C_{Dn} reaches maximum. This
 365 formulation disregards possible spatial variability in surface properties, as well as effects
 366 of atmospheric stability – both factors which very likely are important in polynyas, with
 367 complicated spatial patterns of frazil–open water patches, and at air temperature T_{a} of-
 368 ten 20–30°C lower than the sea surface temperature $T_{\text{s}} \simeq -1.7^\circ\text{C}$ (see Table 2.1 for T_{a}
 369 during the analyzed events).

370 The wind drag over open ocean has been analyzed for many years under a wide range
 371 of wind and sea state conditions. Over vast areas of the oceans, especially far from the
 372 coasts and frontal zones, the assumption $C_{\text{D}} \simeq C_{\text{Dn}}$ is justified, because the air–sea tem-
 373 perature differences tend to be small. At very low air temperatures, however, the neg-

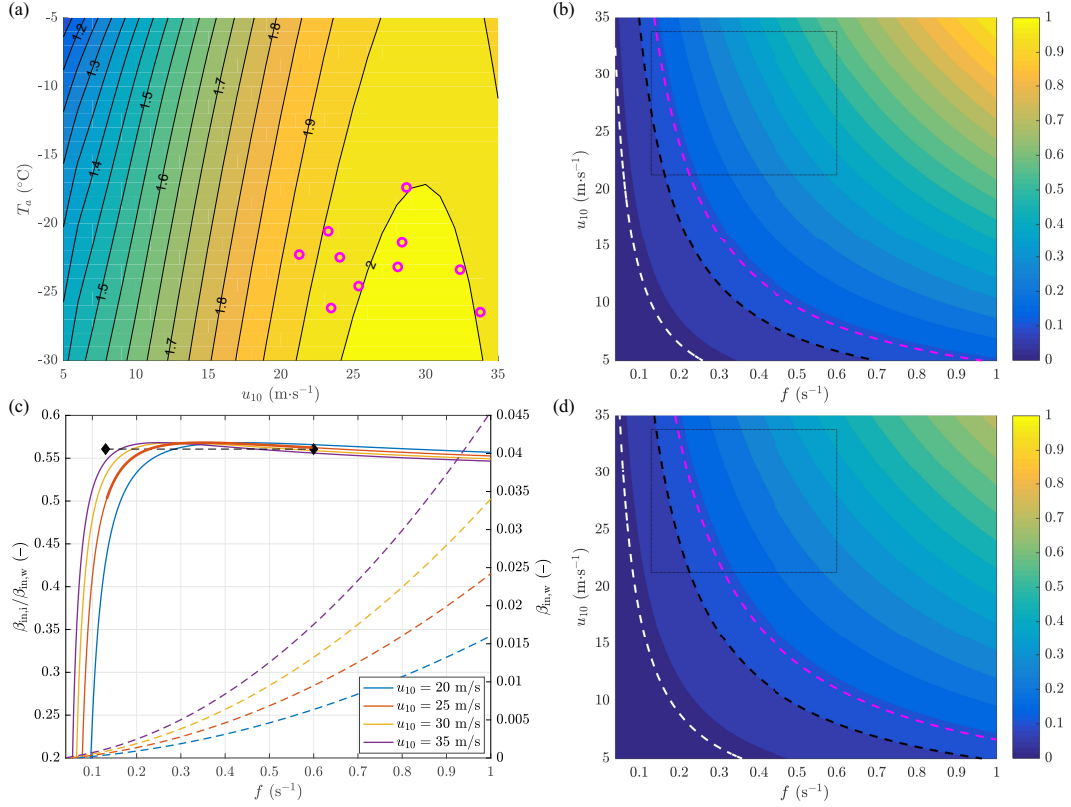


Figure 3. Surface drag and wind input over open water and sea ice. In (a), colors show the open-water surface drag coefficient $C_D(u_{10}, T_a)$ (in 10^3); magenta symbols mark the ten (u_{10}, T_a) combinations in the analyzed TNBP events (Table 1). In (b), colors show the open-water u_*/c ratio (–) in function of wave frequency f and wind speed u_{10} . The dashed contours mark: the value of $\beta_{in,w} = 0$ (white), $u_*/c = 0.1$ (black) and $u_*/c = a_2/a_1 \simeq 0.14$ (magenta). The dotted rectangle marks the approximate boundary of a region relevant for polynyas (see text for details). In (c), the ratio $\beta_{in,i}/\beta_{in,w}$ is shown for four selected values of wind speed (continuous lines; left axis), together with the corresponding curves for $\beta_{in,w}$ (dashed lines; right axis). The black line with diamonds shows the mean ratio $\beta_{in,i}/\beta_{in,w}$ at $u_{10} = 25 \text{ m}\cdot\text{s}^{-1}$ within the frequency range $f \in [0.13, 0.6] \text{ Hz}$ (thick red line). Panel (d) is analogous to (b), but for sea ice instead of open water. Note that all results in (a)–(d) are for $\theta_{rel} = 0$; they change very little for $|\theta_{rel}| < 30^\circ$.

374 active vertical stability of the lower atmosphere leads to a stronger ocean–atmosphere cou-
 375 pling and increased drag at the surface (an effect that, over polynyas, is partially reduced
 376 by very high wind speeds). For C_{Dn} given by (6), $C_D(u_{10}, T_a)$ can be determined using
 377 the Monin–Obukhov stability theory. The result is shown in Fig. 3a, together with the
 378 combinations of u_{10} and T_a in the analyzed polynya events (magenta symbols). As they
 379 all cluster at the plateau of relatively constant values of C_D , in the rest of this analy-
 380 sis we set, for the sake of simplicity, the open-water drag to $C_{Dw} = 2 \cdot 10^{-3}$.

381 Studies on the surface drag over an ice-covered ocean concentrate mainly on the
 382 Arctic ice pack and the MIZ, i.e., conditions where the surface morphology and the as-
 383 sociated form drag play an important role (e.g., Garbrecht et al., 2002; Lüpkes & Birn-
 384 baum, 2005; Lüpkes et al., 2012; Mchedlishvili et al., 2023). Observations for frazil and
 385 grease ice are rare and limited to low-wind and mildly-sloped wave conditions (see Guest,
 386 2021b, and references there). For frazil and grease ice, drag coefficients between $0.7 \cdot 10^{-3}$

387 and $1.3 \cdot 10^{-3}$ have been reported. No formula relating wind speed to surface drag, anal-
 388 ogous to (6) and valid for frazil/grease sea ice has been proposed so far. In polynyas, the
 389 sea surface in ice-covered areas is characterized by the presence of long waves (with length
 390 and amplitude similar to those in the surrounding open water) and absence of high-frequency
 391 waves (Fig. 1). It is an open question how these unique surface properties – very smooth
 392 at length scales of centimeters to meters, undulating at length scales of tens of meters
 393 – modify the bulk drag coefficient. Aware of uncertainties behind this assumption, we
 394 select the middle value from the range reported above ($1 \cdot 10^{-3}$), increase it by 5% to ac-
 395 count for stability effects analogous to those in open water (Fig. 3a), and arrive at the
 396 value $C_{Di} = 1.05 \cdot 10^{-3}$ for ice-covered parts of the polynyas.

397 With these C_{Dw} and C_{Di} , the ratio u_*/c can be computed for a range of (f, u_{10})
 398 combinations over open water and ice (Fig. 3b,d). When the wind speed is low and the
 399 waves are long (MIZ-typical conditions), u_*/c is small and, consequently, in equation (5),
 400 the second term in square brackets is larger than the first one (regions to the left of the
 401 dashed magenta lines in Fig. 3b,d). Thus, β_{in} is approximately linearly proportional to
 402 u_*/c and its values are very low (they equal zero to the left of the dashed white lines in
 403 Fig. 3b,d). Conversely, for short waves and high wind speeds, β_{in} is large and propor-
 404 tional to $(u_*/c)^2$. Crucially, over both ice and open water, most of the combinations of
 405 f and u_{10} relevant for polynyas lie in the strongly-forced regime (dotted rectangles in
 406 Fig. 3b,d). For wind speeds between, say, 20 and 35 $\text{m} \cdot \text{s}^{-1}$, the ratio $\beta_{in,i}/\beta_{in,w}$ decreases
 407 slowly with f (it approaches C_{Di}/C_{Dw} as $f \rightarrow \infty$), but it remains fairly constant for
 408 wave frequencies $f > 0.2$ Hz (Fig. 3c). It drops rapidly to very low values as f drops
 409 below 0.2 Hz, but for those long waves β_{in} itself is very small (dashed lines in Fig. 3c)
 410 – if these waves grow, its due to nonlinear wave–wave interactions and not due to direct
 411 energy input from the wind. Therefore, for the sake of simplicity, we set a_{in} in (1) to a
 412 constant value, equal to the mean $\beta_{in,i}/\beta_{in,w}$ over frequency range $f \in [0.13, 0.6]$ Hz at
 413 wind speed $u_{10} = 25 \text{ m} \cdot \text{s}^{-1}$ (a typical value for our set of TNBP events). Thus, $a_{in} =$
 414 0.56 in all our simulations, as marked with the black line in Fig. 3c.

415 By drawing an analogy to oil slicks once again, we notice that the observed ratios
 416 of u_* over slicks to that over open water are close to 0.8 (e.g., Alpers & Hühnerfuss, 1989),
 417 leading to the ratios $\beta_{in,i}/\beta_{in,w}$ of 0.66–0.67, higher than but comparable to our estimate.

418 3.2.3 S_{ice}

419 Finally, for the ice dissipation term S_{ice} in (1), an empirical expression used in both
 420 SWAN and WaveWatchIII wave models (Collins & Rogers, 2017; Rogers, 2019) has the
 421 form of a sum:

$$422 \quad S_{ice} = \alpha_{ice} E = \sum_{n=0}^{n_m} \alpha_{ice,n} f^n E, \quad (7)$$

423 where $\alpha_{ice,n}$ for $n = 1, \dots, n_m$ are coefficients that can be tuned to a particular situ-
 424 ation or set to values from one of the published studies (see, e.g., Rogers, Meylan, & Ko-
 425 hout, 2018; Rogers, Posey, et al., 2018, for an overview of available formulae). The de-
 426 fault settings in SWAN are from Meylan et al. (2014), with $\alpha_{ice,2} = 1.06 \cdot 10^{-3} \text{ s}^2 \text{ m}^{-1}$,
 427 $\alpha_{ice,4} = 2.3 \cdot 10^{-2} \text{ s}^4 \text{ m}^{-1}$ and the remaining $\alpha_{ice,n}$ equal to zero. With this set of coef-
 428 ficients, the energy attenuation in ice gradually changes slope from f^2 for long waves to
 429 f^4 in the tail of the spectrum. Several subsequent studies use this form of S_{ice} with re-
 430 tuned $\alpha_{ice,2}$ and $\alpha_{ice,4}$ (e.g., Rogers, Meylan, & Kohout, 2018; Rogers et al., 2021). Gen-
 431 erally, their values in frazil and grease ice are even a few times lower than in pancakes
 432 and ice floes. Some observations provide evidence for f^5 or f^6 in the spectral tail (Rogers
 433 et al., 2021, and references there), leading to a different combination of zero and non-
 zero coefficients in (7).

434 Notably, S_{ice} in (7), being purely empirical, does not differentiate between various
 435 physical energy dissipation mechanisms that are relevant in different ice types. The change

of slope of $\alpha_{\text{ice}}(f)$ from low to high wave frequency, described above, is often attributed to different (combinations of) physical attenuation mechanisms dominating in the long-wave and short-wave parts of the spectrum. In frazil and grease ice analyzed here, however, it seems reasonable to assume that viscous dissipation is the only relevant process and that, at least within the relatively narrow frequency range carrying most energy, a single exponent n can be used for all f .

Additional formulations of S_{ice} with dependence on ice thickness have been proposed and are implemented in SWAN. They are not considered here. As this study concentrates on the active-frazil parts of polynyas, i.e., before the ice consolidates into a relatively compact ice cover, no significant effects of ice thickness are expected. Analogously, we do not consider here a source term describing wave scattering in sea ice, as this process is not relevant in frazil and grease ice.

3.3 Model setup and simulations

The simulations in this analysis are performed with SWAN version 41.45 (<http://www.swan.tudelft.nl>). In accordance with the assumptions formulated in section 3.1, several simplifications are made in the model setup. A rectangular model domain with 200 m spatial resolution is used, with realistic coastlines, but a constant water depth of 500 m. For each polynya, two sea ice maps have been prepared, one with ice concentration within the polynya $A = 0$ (for reference, open-water model runs; see below), and one with ice concentration obtained by averaging the values of A determined in Bradtko and Herman (2023) within each 200×200 m² grid cell of the model. In both cases, the ice pack surrounding the polynya has ice concentration $A = 1$. The model is run in a stationary mode and forced with wind fields from AMPS (section 2). No currents are taken into account. In spectral space, directional resolution of 10° and 52 frequency bins logarithmically spaced between 0.05 and 1.576 Hz are used. Thus, the maximum frequency is close to six times the highest expected peak frequency (~ 0.25 Hz), and the frequency increment factor equals 1.07, as recommended for simulations with the near-exact quadruplet wave-wave interaction algorithm (SWAN Team, 2022).

In the simulations, several combinations of a_{in} , and α_{ice} are considered, as listed in Table 2. Setup S0, with $a_{\text{in}} = 1$ and $\alpha_{\text{ice}} = 0$ provides a reference, open-water test case. In setup S1, wind input over sea ice is turned off ($a_{\text{in}} = 0$) and this is the only effect ice has on waves ($S_{\text{ice}} = 0$). In setup group S2, $a_{\text{in}} = 0.56$, as determined in section 3.2. S2_0 is analogous to S1. In S2_f24 (M14) the default SWAN settings for S_{ice} are used, based on Meylan et al. (2014). In the remaining four setups the sea ice source term is fitted to observations by running the model several times with different combinations of coefficients and selecting the version that results in the best agreement between satellite-derived and simulated peak wave periods. Among many possible criteria of ‘the best’ agreement, the mean bias has been selected, as this is the main deficiency of setup S0 that we aim at removing. Thus, the optimization is stopped when the relative bias, defined as the average ratio $(T_{p,\text{obs}} - T_{p,\text{mod}})/T_{p,\text{obs}}$, does not exceed 1% (Table 2). The resulting $\alpha_{\text{ice}}(f)$ are shown in Fig. 4.

Obviously, many more combinations of non-zero $\alpha_{\text{ice},n}$ than those considered here could be tested, including those that are predicted by various theoretical models of viscous and viscoelastic dissipation in sea ice (Meylan et al., 2018). However, as we have no means to extract quantitative information on spectral tails from the available satellite imagery, insight gained from additional simulations would be rather limited. As we demonstrate in the next section, setups S2_f4, S2_f5 and S2_f6 are sufficient to illustrate the sensitivity of the model to ice-related dissipation at high wave frequencies and to formulate some important conclusions regarding frequency dependence of S_{ice} in polynyas.

Table 2. Summary of SWAN simulations: sea-ice related model parameters and model performance

Setup ID	Model parameters		Statistics of T_p			
	a_{in}	$\alpha_{ice,n}$	c.c.	bias	rel. bias	s.d.d.
S0	1	0 for all n	0.87	1.15 s	0.19	0.49 s
S1	0	0 for all n	0.80	-0.06 s	-0.01	0.39 s
S2_0	0.56	0 for all n	0.85	0.66 s	0.11	0.42 s
S2_f24 (M14)	0.56	$\alpha_{ice,2} = 1.06 \cdot 10^{-3}, \alpha_{ice,4} = 0.230 \cdot 10^{-1}$	0.84	0.34 s	0.06	0.40 s
S2_f24 (fitted)	0.56	$\alpha_{ice,2} = 0.53 \cdot 10^{-3}, \alpha_{ice,4} = 1.035 \cdot 10^{-1}$	0.80	-0.02 s	-0.003	0.43 s
S2_f4 (fitted)	0.56	$\alpha_{ice,4} = 1.2 \cdot 10^{-1}$	0.87	0.07 s	0.01	0.37 s
S2_f5 (fitted)	0.56	$\alpha_{ice,5} = 0.66$	0.86	0.04 s	0.01	0.40 s
S2_f6 (fitted)	0.56	$\alpha_{ice,6} = 3.2$	0.83	0.05 s	0.01	0.45 s

c.c. – correlation coefficient, s.d.d. – standard deviation of differences

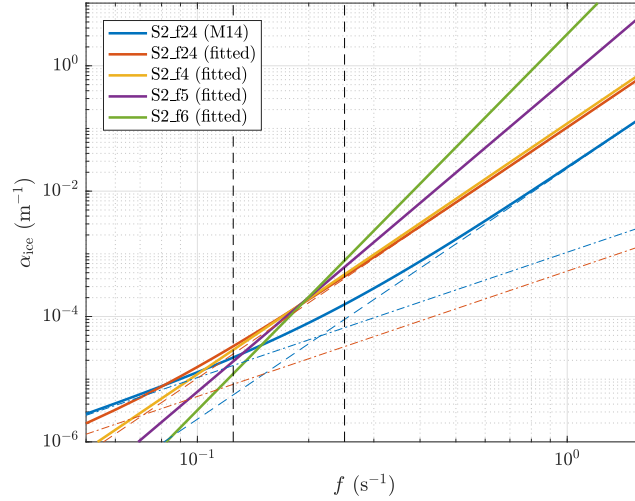


Figure 4. The five $\alpha_{ice}(f)$ curves considered in model version S2. Blue and red thin dashed lines show the components of the two versions of S2_f24 (M14 and fitted), and the black vertical lines mark the range of wave frequencies corresponding to the observed peak periods.

4 Results

In the following, we first compare the performance of the tested model setups (Table 2) in terms of their ability to reproduce the observed patterns of peak periods T_p in all ten polynya events. Subsequently, we perform a detailed analysis of the satellite observations and modelling results for the polynya from 19. Sep. 2019. It is selected for this purpose for two reasons. First, due to its very large size, it covers the whole range of observed wave periods in the analyzed dataset. Second, it is the only image for which the (nearly) simultaneous wave breaking patterns could be obtained from the WV2 image, as described in section 2.2. The whitecap fraction W and energy dissipation S_{wc} within the WV2 scene and over the whole polynya are discussed in section 4.3. Finally, in section 4.4, we return to the whole dataset of 10 polynyas and analyze global (polynya-surface averaged) statistics of individual source terms.

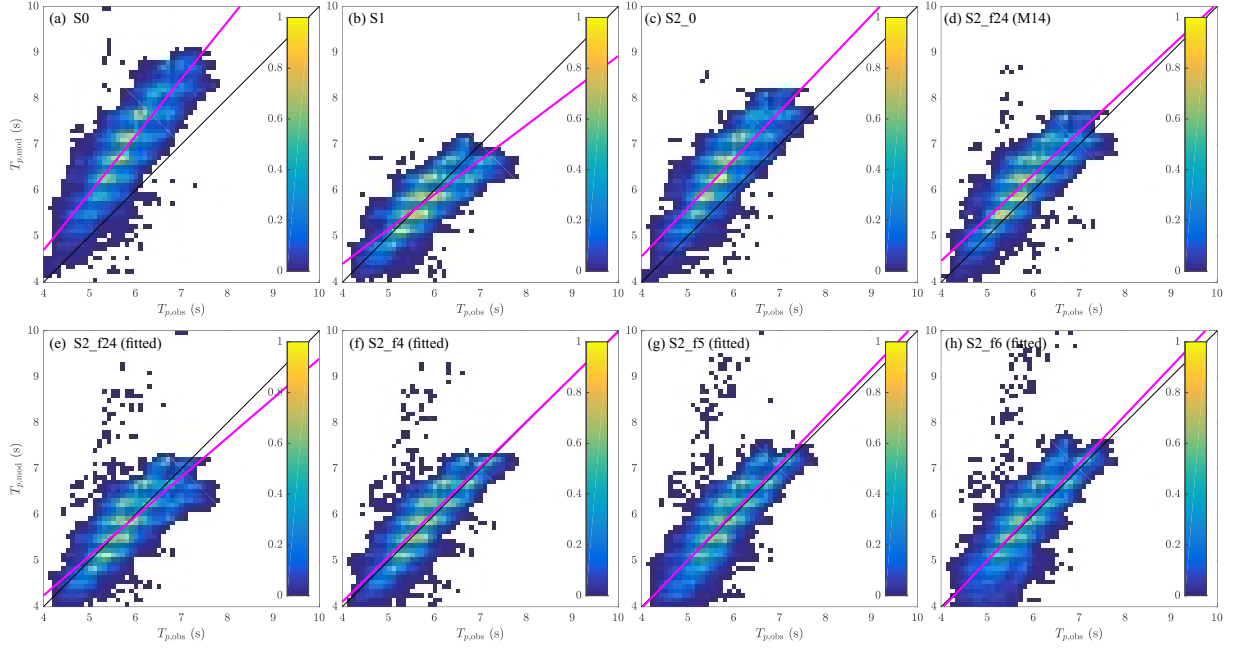


Figure 5. Scatterplots of observed and modelled peak periods, $T_{p,obs}$ and $T_{p,mod}$, from the simulations listed in Table 2. The color scale shows values in percent of the total number of data points (i.e., all values in each plot sum up to 100), and magenta lines show the linear regression to the data.

497

4.1 Performance of the tested model setups

498

499

500

501

For the purpose of model–observations comparison, the satellite-derived maps of T_p from the 10 polynyas are averaged within the meshes of the SWAN grid, resulting in a dataset of over $2.3 \cdot 10^5$ values. The observed peak periods have values between 4 and 8 s, with the mean and median equal to 5.87 s and 5.81 s, respectively.

502

503

504

505

506

507

508

509

510

511

As expected from the results of a simple one-dimensional (1D) model in Bradtke and Herman (2023), setup S0 significantly overestimates the wave periods – on average by 1.15 s or close to 20% (Table 2 and Fig. 5a). This effect occurs in spite of the well documented tendency of SWAN and other spectral models to underestimate wave periods (see, e.g., Rogers et al., 2003). Moreover, the AMPS wind speeds used as model input generally tend to be slightly lower than the wind speeds measured at the Manuela station, i.e., if there is a bias in the model forcing, it is towards too weak rather than too strong winds. Thus, as already concluded in Bradtke and Herman (2023), sea ice is the only likely factor responsible for the discrepancy between the observed wave periods and those expected in open water.

512

513

514

515

516

517

518

519

520

521

Not surprisingly, the bias is reduced in setup S1, with $a_{in} = 0$, even though no energy dissipation in sea ice is assumed. In fact, the mean bias in S1 is close to zero, and the standard deviation of differences is reduced relative to S0. However, these improvements are achieved at the cost of lowered correlation coefficients; moreover, the model clearly underestimates the large wave periods (Fig. 5b), i.e., the wave growth is inhibited in downwind parts of polynyas with high ice concentration. Obviously, the assumption behind S1 that the influence of frazil streaks is strong enough to completely shut down the wind input, but at the same time that the ice has no direct influence on waves through dissipation, seems unrealistic. However, adding to S1 any $\alpha_{ice} > 0$ would lead to an even worse model performance and to a negative bias. Hence, the lack of wind in-

522 put over ice-covered areas is an unlikely explanation for the observations and, accord-
 523 ingly, ‘deactivation’ of S_{in} over ice is not a good choice.

524 As can be seen in Table 2, setting a_{in} to 0.56 as in S2.0 reduces approximately half
 525 of the mean bias of S0 (Fig. 5c), with a still further reduction in setup S2_f24 (M14), i.e.,
 526 when the default S_{ice} SWAN setting is used (Fig. 5d). The performance can be improved
 527 further by fitting $\alpha_{\text{ice},2}$ and $\alpha_{\text{ice},4}$. However, the fitted value of $\alpha_{\text{ice},2}$ is twice as low as
 528 in the corresponding setup with M14, and $\alpha_{\text{ice},4}$ is over four times higher, meaning that
 529 the fitted α_{ice} is dominated by the f^4 term: the change of slope towards f^2 takes place
 530 at frequencies well below 0.1 Hz, i.e., outside of the range of wave frequencies found in
 531 our dataset (compare blue and red curves in Fig. 4). Indeed, dropping the $\alpha_{\text{ice},2}$ term
 532 as in S2_f4 results in the fitted value of $\alpha_{\text{ice},4}$ very close to that in S2_f24 (Table 2). More-
 533 over, although setup S2_f4 has only one fitted coefficient as opposed to two in S2_f24, it
 534 gives the best global statistics not only in terms of the mean bias, but also the correla-
 535 tion coefficient and standard deviation of differences – and it performs well in the whole
 536 range of the observed values of T_p (Fig. 5f). Therefore, the simpler version S2_f4 is pre-
 537 ferred over S2_f24.

538 Finally, the last two tested setups are S2_f5 and S2_f6, which, as expected, leads
 539 to a stronger (weaker) attenuation of the lowest (highest) wave periods (Fig. 5f–h). With
 540 increasing power n the scatter gets slightly higher and the correlation coefficient lower
 541 (Table 2), but, arguably, the differences between the global statistical measures of set-
 542 ups S2_f4, S2_f5 and S2_f6 are rather subtle. This is not surprising as the analysis so
 543 far is limited to the peak periods, i.e., the frequency range in which the strength of dis-
 544 sipation in S2_f4, S2_f5 and S2_f6 is very similar (Fig. 4). The differences between these
 545 setups can be expected to be more substantial in the tails of the wave energy spectra.
 546 Unfortunately, as stated earlier, we cannot perform any quantitative comparison between
 547 the observed and modelled spectral tails. However, as we will see in the next section, large
 548 qualitative differences between the results of S2_f4, S2_f5 and S2_f6 allow for some (care-
 549 ful) conclusions.

550 4.2 The polynya from 19. Sep. 2019

551 The polynya from 19. Sep. 2019 (Fig. 1) is the largest among the ten polynyas anal-
 552 ysed here (see S_p in Table 1). At the time the analysed satellite image was acquired, the
 553 area had been subject to prolonged strong WNW winds with speeds exceeding $20 \text{ m}\cdot\text{s}^{-1}$
 554 for ~ 36 hours, and exceeding $30 \text{ m}\cdot\text{s}^{-1}$ for close to 24 hours (not shown). As the polynya
 555 has a relatively regular, symmetric shape, it is useful to examine the wind forcing, and
 556 the observed and simulated wave properties on a transect along its central axis (white
 557 dashed line in Fig. 1; corresponding maps can be found in Supplementary Figs. S2 and
 558 S3). At 21 UTC the AMPS wind (Fig. 6a) along that line oscillates between 30 and $35 \text{ m}\cdot\text{s}^{-1}$
 559 up to a distance x of ~ 50 km from shore, and drops to 25 – $30 \text{ m}\cdot\text{s}^{-1}$ only within the last
 560 ~ 10 km of the polynya. It also gradually changes direction from WNW to WSW, but
 561 this change is not fast, in the order of 10° per 30 km. In terms of ice concentration (Fig. 6b),
 562 two clearly different regions can be distinguished: for x below and above 40 km. In the
 563 first region, the ice concentration varies strongly as the analyzed profile crosses sea-ice
 564 and open-water patches, but on average it remains rather low (mean value 0.41). In the
 565 second region, it rarely drops below one (mean value 0.98).

566 As can be seen in Fig. 6c, the no-ice setup of SWAN (S0) significantly overpredicts
 567 the peak wave period (by almost 2 s, i.e., close to 30%, in the offshore part of the polynya).
 568 It also predicts significant wave heights H_s exceeding 5 m (see Supplementary Fig. S3
 569 for corresponding maps of T_p and H_s). The three ‘best’ setups identified in section 4.1,
 570 S2_f4–S2_f6, produce almost indistinguishable $T_p(x)$ and $H_s(x)$ curves. In agreement with
 571 observations, T_p at the downwind end of the polynya exceeds 7 s (corresponding to peak
 572 wavelengths of 75–80 m). Notably, H_s reaches maximum at the end of the varying-ice-

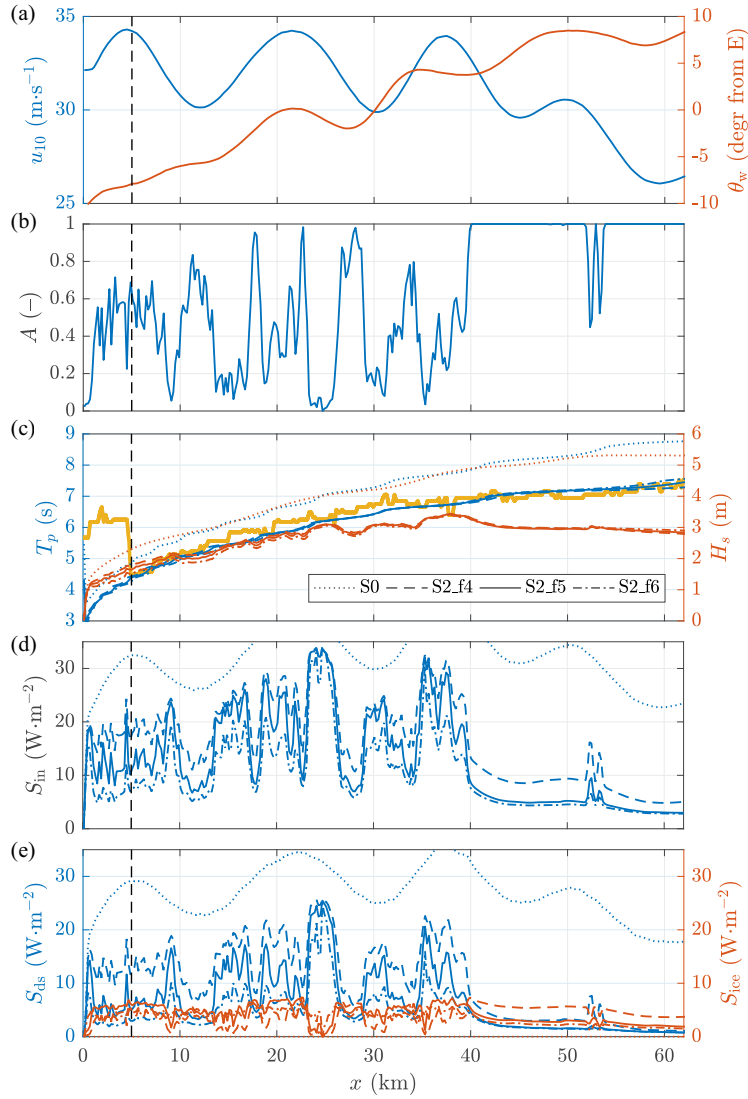


Figure 6. Wind speed u_{10} and direction θ_w (a), ice concentration A (b), significant wave height H_s and peak period T_p (c), wind input S_{in} (d), and dissipation due to wave breaking S_{ds} and in sea ice S_{ice} (e) along the central line of the polynya from 19. Sep. 2019 (see Fig. 1 for transect location). In (c)–(e), the modelling results are shown for four model setups: S0 (dotted lines), S2_f4 (dashed lines), S2_f5 (continuous lines) and S2_f6 (dash-dotted lines); thick yellow line in (c) shows the observed T_p . The black vertical dashed lines at $x = 5$ km mark the boundary of the nearshore region where no reliable wave properties could be determined from the satellite data.

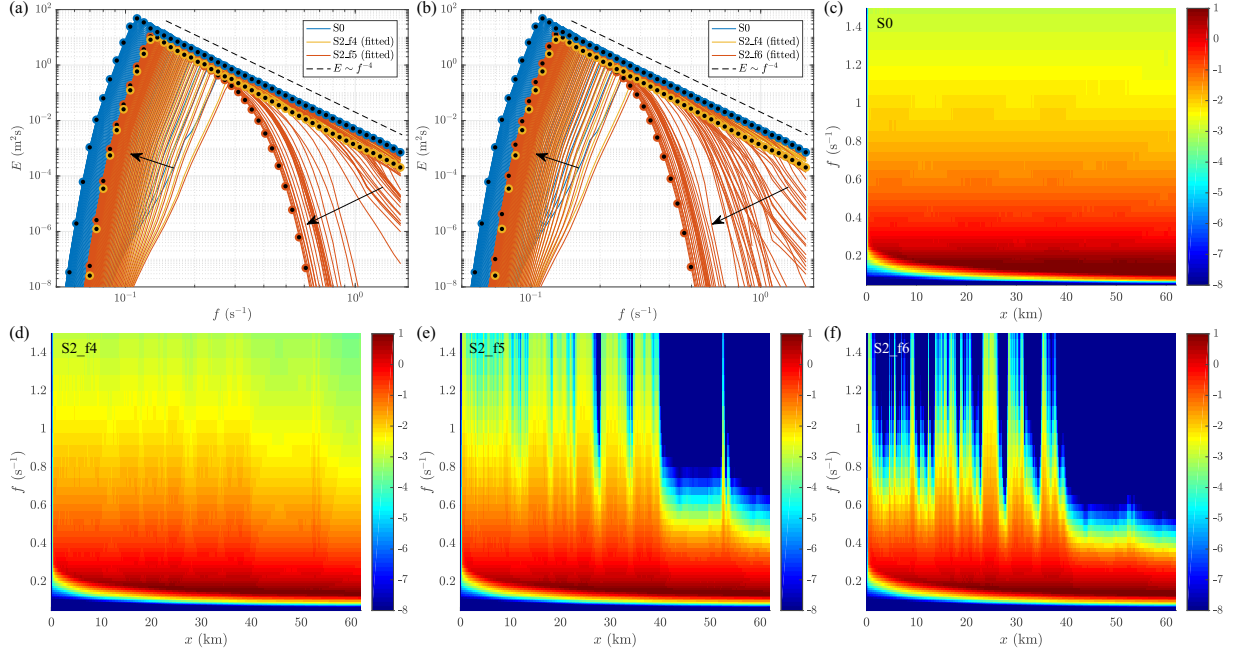


Figure 7. Wave energy spectra $\bar{E}(f)$ along the central line of the polynya from 19. Sep. 2019 (see Fig. 1 for transect location) from four model setups: S0, S2_f4, S2_f5 and S2_f6. In (a,b), every 5th spectrum along the transect is drawn for each setup (S0, S2_f4 and S2_f5 in a, S0, S2_f4 and S2_f6 in b); black arrows mark the direction of increasing x , and the dashed black line has the slope f^{-4} . In (c)–(f), colors show $\log_{10} \bar{E}$ ($\text{n m}^2\text{s}$) for S0 (c), S2_f4 (d), S2_f5 (e) and S2_f6 (f).

573 concentration zone, close to $x = 40$ km, and then stays roughly constant at ~ 3 m, in-
 574 dicated an approximate balance between wind input and dissipation.

575 In spite of very similar evolution of the spectral peaks, however, the results of the
 576 three setups differ substantially from each other for frequencies above ~ 0.4 Hz (Fig. 7).
 577 In S2_f4, the tails of the spectra remain very close those in the open-water case S0, even
 578 at the downwind end of the polynya. That is, $E \sim f^{-4}$ in the tail (Fig. 7a). In open
 579 water it is a signature of the balance between wind input and whitecapping dissipation
 580 (red and yellow curves in Fig. 8a–e; see also Fig. 6d,e). Indeed, in S2_f4 \tilde{S}_{in} and S_{ds} dom-
 581 inate in the spectral tail wherever the ice concentration is relatively low (Fig. 8h). At
 582 higher A , \tilde{S}_{ice} is comparable to S_{ds} (Fig. 8f,g) or even higher (Fig. 8i,j), but the frequency
 583 dependence of both source terms is the same – in terms of their mathematical form they
 584 are interchangeable. In S2_f5 and S2_f6, to the contrary, ice-induced dissipation of the
 585 high-frequency waves is strong enough so that they are almost entirely removed from the
 586 spectra as soon as the ice concentration exceeds ~ 0.5 . This produces spectral shapes sim-
 587 ilar to those observed in the MIZ (compare brown curves in Fig. 5a,b with, e.g., Fig. 6
 588 of Rogers et al. (2016) or Fig. 2 of Montiel et al. (2022)). As the waves propagate through
 589 the patches of grease ice and open water in the central parts of the polynya, the short
 590 waves in the spectral tail disappear and reappear as in Fig. 7e,f – an aspect of the re-
 591 sults that qualitatively agrees with what is seen in the WV2 image (Figs. 1 and 2).

592 The consequences of very strong dissipation of short waves in S2_f5 and, especially,
 593 S2_f6 are clearly seen in the plots of source terms in Fig. 8k–u. As the wave energy at
 594 frequencies higher than ~ 0.4 Hz is zero or close to zero in ice-covered locations, the wind
 595 input there is close to zero as well – as are all other source terms. Remarkably, in these

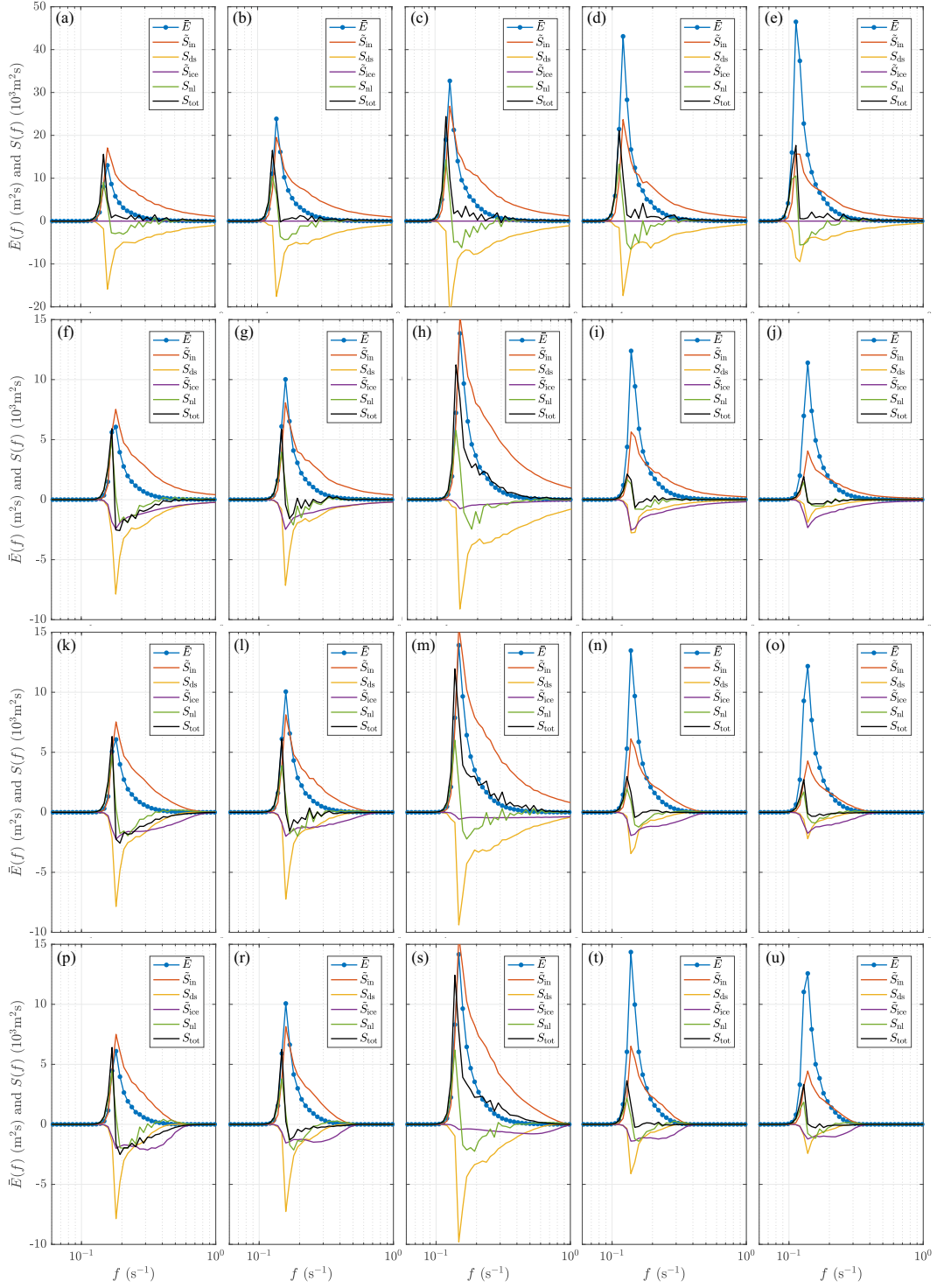


Figure 8. One-dimensional wave energy spectra $\bar{E}(f)$ and source terms at 5 locations along the central line of polynya from 19. Sep. 2019 (white dots in Fig. 1a), from model setups S0 (a–e), S2_f4 (f–j), S2_f5 (k–o) and S2_f6 (p–u). For wind input and sea ice source terms, $\tilde{S}_{in} = [1 - A + a_{in}A]S_{in}$ and $\tilde{S}_{ice} = AS_{ice}$ are shown (see equation 1). The black lines show S_{tot} , the sum of all source terms. Note different y -axis scales in (a–e) and (f–u). The ice concentration A at points 1–5 equals 0.72, 0.85, 0.29, 1.00 and 1.00, respectively.

596 areas the dissipation in sea ice is particularly strong in the range 0.2–0.4 Hz, i.e., just
 597 below the no-energy range. If the ice concentration is not too high (Fig. 8k,l,p,r), this
 598 energy sink is strengthened by whitecapping, leading to a negative overall energy bal-
 599 ance in spite of energy input from wind and, to a lesser extent, from quadruplets. At ice
 600 concentration close to 1 (Fig. 8n,o,t,u), the role of whitecapping and quadruplets becomes
 601 less significant, and the first-order energy balance is between wind input and ice dissi-
 602 pation. As a net effect, the energy spectra evolve towards narrow, swell-like shapes (see
 603 maps of directional spreading in Supplementary Fig. S3).

604 4.3 Wave breaking

605 The total surface area of breaking waves estimated from the WV2 data covers 1.08%
 606 of the whole area of the analyzed image. Their spatial distribution is inversely correlated
 607 with sea ice concentration (Fig. 9a). Considering the whole area of the WV2 image, the
 608 contribution of breaking waves to the open-water surface is 1.5%, more than twice as much
 609 as in the ice-covered areas, where it is 0.6%. Locally, however, this difference depends
 610 on the spatial pattern of frazil streaks – which can be seen when the two subsets of the
 611 WV2 area are analyzed separately (Fig. 10).

612 Over much of the lower part of the WV2 image (subset 2), the average ice concen-
 613 tration calculated in vertical sections is relatively low and remains between 0.2 and 0.4
 614 with no visible spatial trend (Fig.10). This subset shows narrow streaks of frazil ice that
 615 only begin to increase in width and merge near the center of the image and gradually
 616 form a more compact ice cover. Under these conditions, the average whitecap fraction
 617 W_X changes similarly in open water and in ice, with W_X reaching a maximum at the
 618 distance of about 14–16 km from the ice sheet. In this area, the difference between W_X
 619 in water and ice remains roughly constant. Only when the average ice concentration in-
 620 creases to about 0.5, at the distance of 21.5 km from shore, a rapid decrease of W_X in
 621 streaks and a corresponding increase in open water is observed, producing an order-of-
 622 magnitude difference between the W_X in open-water and ice-covered areas.

623 In the upper part of the image (subset 1), the variability of whitecap fraction in
 624 open water are similar (Fig. 10), with a maximum at an approximately the same distance
 625 from shore. However, the difference between W_X in open water and ice in subset 1 is gen-
 626 erally larger than in subset 2, which can be at least partly explained by the presence of
 627 the very wide and long (width ~ 500 m) ‘mega-streak’ – a dominating feature in subset 1.
 628 As can be seen in Fig. 9a, it contains almost no whitecaps, contributing to reduced W_X
 629 values.

630 The satellite-based wave breaking patterns cannot be directly compared with mod-
 631 elling results, because spectral wave models do not produce whitecap fraction as output.
 632 Therefore, a relationship between W and energy dissipation rate S_{wc} is necessary. To
 633 this end, we use formulae derived by Anguelova and Hwang (2016). Assuming that the
 634 water is deep, we have:

$$W = c_W \omega_p^4 S_{wc}, \quad (8)$$

635 where $\omega_p = 2\pi/T_p$ denotes the peak wave frequency and the coefficient c_W is a com-
 636 bination of several empirical constants: $c_W = t_b [4b\rho_w g^3 \log(c_{\max}/c_{\min})\alpha_c^4]^{-1}$. Their val-
 637 ues vary strongly between different field and laboratory experiments. Here, without any
 638 tuning, we adopt the values from Anguelova and Hwang (2016) for three out of the four
 639 coefficients: the bubble persistence time $t_b = 2$ s, the breaking strength parameter $b =$
 640 0.013, and the ratio of maximum to minimum breaker speed $c_{\max}/c_{\min} = 10$. The fourth
 641 one, $\alpha_c \in (0, 1)$, denotes the ratio of the threshold breaker speed to the peak wave phase
 642 speed. In Anguelova and Hwang (2016), $\alpha_c = 0.3$ is used based on the average from
 643 experiments analyzed in Gemmrich et al. (2008). Here, we instead use the modal value
 644 of the α_c distribution from the case in Gemmrich et al. (2008) with the highest u_*/c ra-
 645 tio, as it represents a situation closest to the one analyzed here. Thus, we set $\alpha_c = 0.35$.

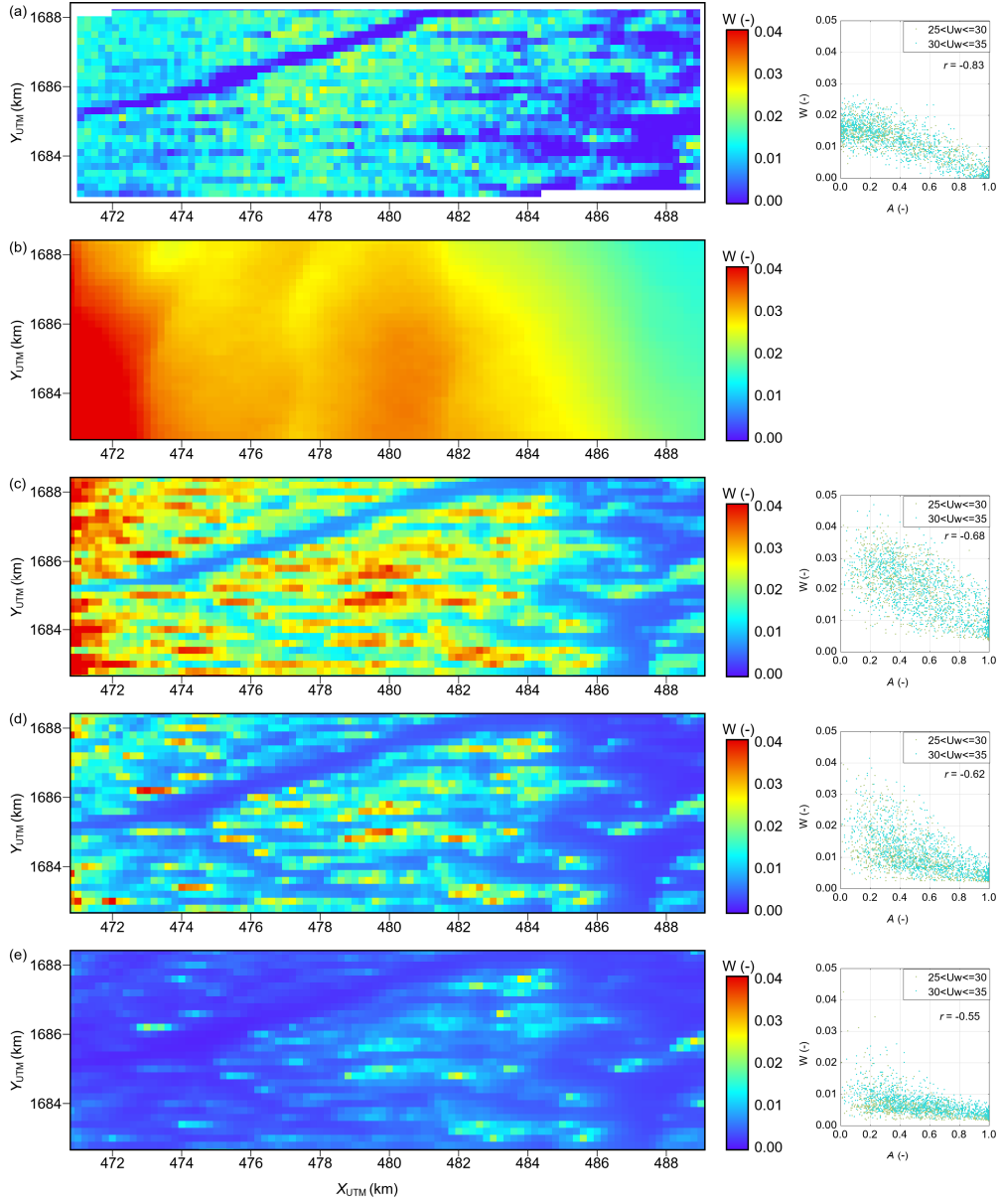


Figure 9. Observed and modelled wave breaking patterns in the area covered by the WV2 image (orange rectangle in Fig. 1). The left panels show maps of whitecap fraction W from the WV2 image (a) and from SWAN simulations with model setup S0 (b), S2_f4 (c), S2_f5 (d) and S2_f6 (e). Right panels show scatterplots of W against ice concentration A for wind speeds below and above $30 \text{ m}\cdot\text{s}^{-1}$ (green and blue dots).

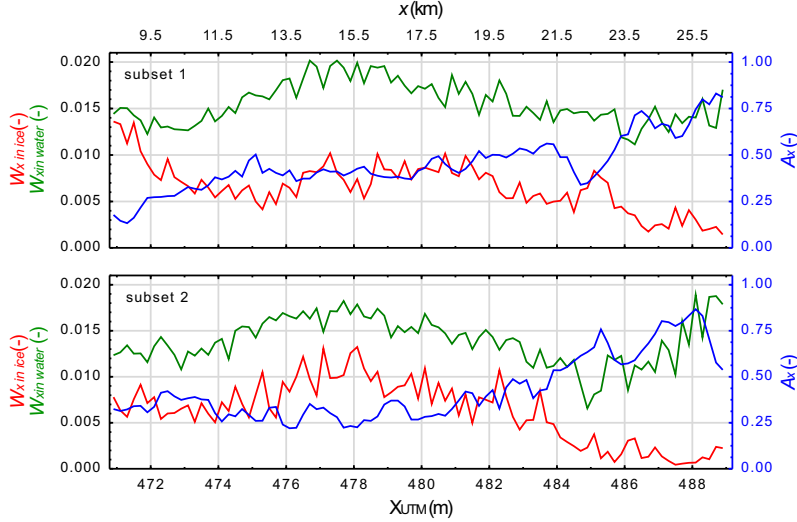


Figure 10. Average ice concentration A_X (right axes) and whitecap fraction W_X computed separately over ice-covered and ice-free regions (left axes) of subsets 1 and 2 of the analyzed WV2 image. X_{UTM} and x denote the UTM coordinates and the distance from the ice sheet, respectively.

646 The resulting maps of W in the WV2 region from model setups S0, S2_f4, S2_f5
 647 and S2_f6 are shown in Fig. 9b–e. Not surprisingly, the results of the no-ice setup S0 are
 648 completely different from satellite observations. However, the remaining three setups pro-
 649 duce spatial patterns which are very similar to the observed one – and, at a general level,
 650 very similar to each other (this is also true for the whole polynya; see Supplementary Figs.
 651 S4 and S5). The best agreement is obtained for S2_f5, which also produces very simi-
 652 lar range of values, generally with $W < 0.03$. In S2_f6, wave breaking is very weak, mostly
 653 with $W < 0.01$ and with only isolated hotspots of whitecap fractions reaching 0.02. In
 654 S2_f4, to the contrary, values exceeding 0.03 are not rare, especially in the leftmost part
 655 of the region (a feature absent in satellite-derived data).

656 It is noteworthy that that the spatial patterns of W and S_{ds} are markedly differ-
 657 ent (Supplementary Fig. S5) due to the strong wave-frequency dependence of W in equa-
 658 tion (8). For the same whitecap fraction W , energy dissipation is lower in long waves
 659 than in short waves, and *vice versa*, the same energy dissipation is associated with higher
 660 values of W when the waves are shorter. This is responsible for the clearly fetch
 661 dependence of W in our simulations: the largest values of W can be found nearshore (in
 662 all model versions, including S0), when they exceed 0.1. In the case of S_{ds} , it is predom-
 663 inantly influenced by wind speed u_{10} and ice concentration A (Supplementary Figs. S6
 664 and S7). Indeed, as Supplementary Fig. S7 shows for the example of setup S2_f5, $S_{ds}(u_{10}, A)$
 665 can be easily fit to the data, with the dependence on wind speed being $S_{ds} \sim u_{10}^{2.88}$, which
 666 is very close to the relationship $S_{ds} \sim u_{10}^3$ reported in the literature (Anguelova & Hwang,
 667 2016).

668 4.4 Global source terms statistics

669 Although the differences between setups S2_f4–S2_f6 manifest themselves mainly
 670 in the tails of the spectra, their effects are clearly visible in spectrally integrated source
 671 terms as well (see Fig. 6d,e and maps in Supplementary Fig. S4). The overall spatial pat-
 672 terns remain similar, as they are dictated by the variability of ice concentration, but the
 673 amplitude of all source terms varies strongly between setups. Consequently, the total (polynya-

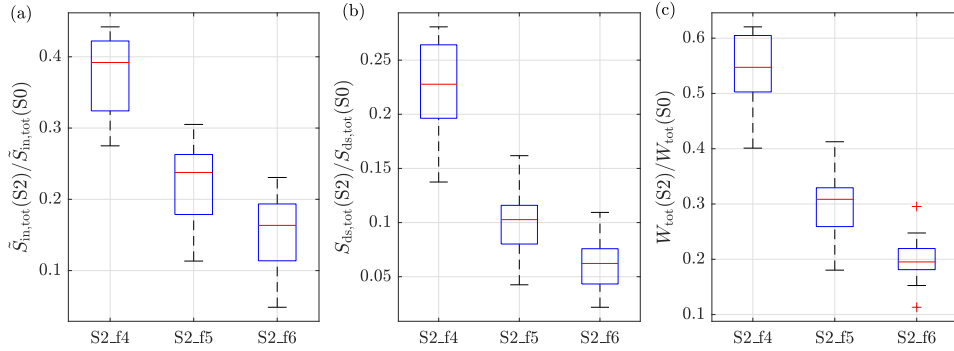


Figure 11. Box plots showing statistics of the ratios $\tilde{S}_{\text{in,tot}}(\text{S2})/\tilde{S}_{\text{in,tot}}(\text{S0})$ (a), $S_{\text{ds,tot}}(\text{S2})/S_{\text{ds,tot}}(\text{S0})$ (b) and $W_{\text{tot}}(\text{S2})/W_{\text{tot}}(\text{S0})$ (c) for the three model versions S2_f4, S2_f5 and S2_f6 and for the ten polynyas analyzed. Red lines show the median values and blue boxes mark the interquartile range.

674 integrated) energy input from wind, $\tilde{S}_{\text{in,tot}}$, as well as dissipation within sea ice $\tilde{S}_{\text{ice,tot}}$
 675 and due to whitecapping $S_{\text{ds,tot}}$ (with the associated W_{tot}), exhibit very large differences
 676 between the ice-free and ice-influenced model versions, hinting at the crucial role of sea
 677 ice in modifying polynyas' ocean–atmosphere interactions.

678 The box plots in Fig. 11 show statistics of the ratios of those global variables in
 679 ice-influenced and ice-free model runs, for the ten polynyas analyzed. Although some vari-
 680 ability between the ten cases is present, the results are fairly robust (notably, there is
 681 no significant correlation between the analyzed ratios and polynya size). Considering that,
 682 based on the analysis so far, model settings S2_f5 and S2_f6 best describe available ob-
 683 servations, it is save to conclude that the polynya-wide wind input is typically reduced
 684 to below 25% of that over open water, the energy dissipation due to whitecapping is re-
 685 duced to below 10%, and the corresponding coverage of sea surface by whitecaps is re-
 686 duced to below 30%. These (conservative) estimates decrease with increasing exponent
 687 n in the S_{ice} source term. Consequences of the lowered wind input and whitecapping are
 688 briefly discussed in the next section.

689 5 Discussion and conclusions

690 This study has shown that wind waves in coastal polynyas with frazil streaks are
 691 significantly modified by sea ice – and that the role of ice is much more complex than
 692 simply dissipating wave energy through viscous processes in a spectral-component-by-
 693 component manner. Rather, the net effect of sea ice is a combined result of dissipation,
 694 reduced wind input, reduced whitecapping, and modified nonlinear energy transfer within
 695 energy spectra. The ‘patchiness’ of the grease ice cover, typical of polynyas, and the as-
 696 sociated alternating removal and re-generation of short waves in the tail of the spectrum
 697 play here a particular role. Regarding the four relevant source terms in the wave energy
 698 balance equation, the main conclusions of this study are:

- 699 • Contrary to the common ‘binary’ treatment of S_{in} in waves-in-ice modelling (e.g.,
 700 Li et al., 2015; Cheng et al., 2017; Rogers et al., 2016, 2021), wind input over grease
 701 ice is neither equal to that over open water ($a_{\text{in}} = 1$) nor zero ($a_{\text{in}} = 0$). Un-
 702 der conditions of strongly forced waves analyzed here, a constant value of the wind
 703 reduction factor $a_{\text{in}} = 0.56$ has been determined based on theoretical arguments
 704 and led to a satisfactory model performance. However, as detailed in section 3.2,
 705 a_{in} is in fact a function of wind speed and wave frequency. Using a simple param-

eterization with constant α_{in} seems reasonable considering very limited observational data on wave growth in ice covered waters, but the analysis in this study provides a general framework for more complex formulations in the future, applicable over a wider range of wave ages and frequencies. Regarding the largely unknown variability of the surface drag coefficient C_{Dn} over grease ice in presence of waves, a promising direction of further research might be analogous to parameterizations of surface drag used in modelling of oil spills, in which the net roughness length is computed as a weighted sum of three components, associated with an aerodynamically smooth surface, long waves and short waves, respectively, and the weight of the last component is different over oil and water, reflecting very strong attenuation of short waves in oil-covered regions (Bourassa et al., 1999; Zheng et al., 2013; Blair et al., 2023).

- Whitecapping is strongly reduced in regions where frazil streaks are present – not only within streaks themselves, but also in open-water areas between them – confirming existing qualitative observations from TNBP (Guest, 2021a, 2021b; Ackley et al., 2022). Crucially, in the model this effect is obtained without any modifications to the formulation of the S_{ds} term. Rather, reduced whitecapping is a consequence of reduced wave steepness, which in turn results from reduced wind input and from dissipation in sea ice. This does not mean, however, that the open-water formulations of S_{ds} used in the present spectral wave models are fully adequate for grease ice regions. It seems likely that the critical steepness used to compute S_{wc} in equation (3) is slightly higher in water covered with grease ice than in open water. Moreover, at the same sea surface area fraction covered with breakers in open water and in grease ice, the amount of dissipated wave energy might be different due to suppressed turbulence and air bubble formation in the latter case.
- As long as the developing ice cover is thin and the open-water dispersion relation holds, the quadruplet wave–wave interactions remain unaffected and can be computed in the same way as in open water. However, in combination with strong ice-related dissipation in the high-frequency part of the spectrum, their role in regions covered with frazil streaks becomes particularly important. In our simulations, there were substantial differences between the results obtained with DIA and with the quasi-exact method. When using DIA, the very strong positive bias of the wave periods could not be reduced by any reasonable combination of adjustable coefficients. With the quasi-exact method, the bias was much smaller and the model calibration unproblematic. Obviously, considering the fact that the computational costs of computing quadruplets in an exact way are over 10^3 times higher than those of DIA, our finding cannot be treated as a recommendation for waves-in-ice modelling, especially in operational or climate applications. However, one should be aware of biases and uncertainties associated with the usage of DIA, and of the danger related to the interpretation of the results of DIA-based models, in which S_{ice} and possibly other source terms must compensate DIA-related biases.
- We did not find any evidence of the change of slope n of the sea ice source term with wave frequency. The most straightforward interpretation is that a single physical mechanism is responsible for energy dissipation in the analyzed case, with viscous or viscoelastic dissipation the most likely candidates. Crucially, although with the observational data at our disposal we were not able to determine the value of n , we show that $n > 4$ is necessary for a sufficiently strong attenuation in the tail of the spectrum, i.e., for preventing the slope in the tail from reaching the $E \sim f^{-4}$ shape, typical for open water. Very importantly, this finding does not contradict observations of $n < 4$ in earlier studies (Meylan et al., 2018, and references there), where it refers to the apparent attenuation from pairs of measured spectra.
- Considering the previous conclusion together with the comparison between the satellite-derived and modelled wave breaking patterns, $n = 5$ seems to produce the best

761 results – but this should be treated as an indication rather than a firm conclusion
 762 (and, obviously, n does not have to be a natural number).

- 763 • On average, the presence of frazil and grease ice in the analyzed polynyas leads
 764 to a reduction of the total wind input to less than 25% of that over open water,
 765 and to the reduction of whitecapping dissipation to less than 10%, with the cor-
 766 responding reduction of the surface area fraction covered with whitecaps to be-
 767 low 30%. Exact values of those ratios depend on the value of n in the S_{ice} term
 768 and thus on the intensity of sea ice dissipation.

769 Some of the above conclusions are specific for polynya conditions. As noted sev-
 770 eral times throughout this paper, waves in the MIZ typically have lower frequency, are
 771 weakly forced by wind, and propagate through a wider variety of ice types. Neverthe-
 772 less, at several locations where wave–ice interactions have been studied, the conditions
 773 are in between those of an ‘ideal’ MIZ and of a coastal polynya. The Beaufort Sea in the
 774 summer and autumn is a good example (Rogers et al., 2016; Smith & Thomson, 2016):
 775 the wind fetch is relatively short, frequent low pressure systems are associated with high
 776 wind speeds, and a typical ice type is a thin frazil-pancake mixture. Therefore, a proper
 777 treatment of the S_{in} and, close to the ice edge, S_{ds} terms is important for reliable spec-
 778 tral modelling, and the present study provides important clues to the formulation of those
 779 terms. On the other hand, some of the assumptions made here might be unsuitable for
 780 the MIZ. The contribution of nonbreaking-waves dissipation S_{nbr} to the total S_{ds} is just
 781 one example – it is negligible in a coastal polynya, where whitecapping dominates over
 782 other dissipation mechanisms ($f_{br} \simeq 1$ in equation (2)), but the opposite might be true
 783 for the MIZ, where the waves do not break, but turbulent dissipation in the under-ice
 784 boundary layer (Voermans et al., 2019; Herman, 2021) dominates the S_{ds} term.

785 Our study provides also a very good example of limitations for model development
 786 caused by the lack of sufficient observational data. Performing wave-in-ice measurements
 787 in the MIZ is very challenging. In coastal polynyas, it is even more difficult due to, first,
 788 extreme weather conditions (very high wind speeds, very low air temperatures), and sec-
 789 ond, short wavelengths, requiring higher spatial (in the case of satellite and airborne im-
 790 agery) and temporal (in the case of wave buoys and other in situ sensors) resolution. In
 791 the TNBP and other coastal polynyas, peak wavelengths only rarely exceed 80–90 m and
 792 are lower than that over most of the polynya area. Thus, the usage of many popular syn-
 793 thetic aperture radar (SAR) data sources to retrieve wave energy spectra (e.g., Stopa,
 794 Ardhuin, et al., 2018; Wadhams et al., 2018) becomes problematic, as their resolution
 795 is comparable with wavelength. Even if peak wavelengths can be determined with suf-
 796 ficient accuracy, estimation of the spectral tails is unreliable. This study has shown that,
 797 although spatial variability of peak periods (and other wave properties at the spectral
 798 peak) provides a very valuable information on the underlying physics, there are limita-
 799 tions to this approach and the knowledge of spectral tails is crucial for making inferences
 800 about the frequency dependence of physical processes shaping the energy spectra. No-
 801 tably, collecting *in situ* wave data from polynyas is challenging as well, e.g., in the case
 802 of wave buoys a serious problem is contamination of measured velocities from heavy buoy
 803 tilting, heaving, as well as very fast drift (exceeding 1 m/s; Ackley et al., 2022). In gen-
 804 eral, the question facing both observations and modelling is whether and how data anal-
 805 ysis methods, (semi)empirical parameterizations etc., formulated and tested under ‘typ-
 806 ical’ conditions, can be transferred to the extreme conditions of polynyas without vio-
 807 lating their underlying assumptions. In particular, in the case of spectral wave modelling,
 808 it is an open issue how expressions (4)–(6) can be made more adequate for polynya events.
 809 A related challenge is reconciling information from observations and models. In this study,
 810 we obtained two different measures of wave breaking in the analyzed area – one in the
 811 form of whitecap fraction W (from a visible satellite image), and one in the form of en-
 812 ergy dissipated per unit surface area S_{wc} (from a spectral wave model). The $W(S_{wc})$ for-
 813 mula from Anguelova and Hwang (2016) with default coefficients happens to produce
 814 model-based values of W very close to those determined from satellite data. However,

815 this and similar relationships suffer from the same problems as the ones mentioned above:
816 the wind speeds in this study are outside the range of observations used to formulate them.

817 Finally, it is worth commenting on the consequences of the significantly reduced
818 wind input and whitecapping dissipation due to the presence of sea ice in polynyas. One
819 of them are lower rates of sea spray production (due to both lower whitecap fractions
820 W and, likely, less intense bubble and spray generation in breaking waves when grease
821 ice is present), which has been shown to contribute large part of the total ocean–atmosphere
822 turbulent heat flux at high wind speeds. Thus, suppressed whitecapping should lead to
823 significantly lower ocean mixed layer heat loss and, consequently, lower sea ice produc-
824 tion rates.

825 Data Availability Statement

826 The code of SWAN model is freely available at <http://www.swan.tudelft.nl>. In-
827 put files necessary to reproduce our simulations, together with modeling results, can be
828 found at <https://zenodo.org/record/8308164> (Herman & Bradtke, 2023).

829 Acknowledgments

830 This work has been financed by Polish National Science Centre projects no. 2018/31/B/ST10/00195
831 (“Observations and modeling of sea ice interactions with the atmospheric and oceanic
832 boundary layers”) and 2022/47/B/ST10/01129 (“Sea ice, waves and turbulence – from
833 laboratory scale to improved large-scale modelling”), and by the University of Gdansk,
834 Laboratory of Physical Oceanography, DS 531-OA02-D425-23. All calculations were car-
835 ried out at the Academic Computer Centre (TASK) in Gdańsk, Poland.

836 References

- 837 Ackley, S., Smith, M., Guest, P., Herman, A., & Shen, H. (2022). Winds, waves and
838 ice formation in a coastal polynya. In *Proc. 26th iahr international symposium*
839 *on ice*. IAHR. (Montréal, Canada, 19–23 June 2022)
- 840 Alberello, A., Bennetts, L., Onorato, M., Vichi, M., MacHutchon, K., Eayrs, C.,
841 ... Toffoli, A. (2022). Three-dimensional imaging of waves and floes in
842 the marginal ice zone during a cyclone. *Nature Comm.*, *13*, 4590. doi:
843 10.1038/s41467-022-32036-2
- 844 Alpers, W., & Hühnerfuss, H. (1989). The damping of ocean waves by surface films:
845 a new look at an old problem. *J. Geophys. Res.*, *94*, 6251–6265. doi: 10.1029/
846 JC094iC05p06251
- 847 Alves, J., & Banner, M. (2003). Performance of a saturation-based dissipation-rate
848 source term in modelling the fetch-limited evolution of wind waves. *J. Phys.*
849 *Oceanogr.*, *33*, 1274–1298. doi: 10.1175/1520-0485(2003)033<1274:POASDS>2.0
850 .CO;2
- 851 Anguelova, M., & Hwang, P. (2016). Using energy dissipation rate to obtain active
852 whitecap fraction. *J. Phys. Oceanogr.*, *46*, 461–481. doi: 10.1175/JPO-D-15
853 -0069.1
- 854 Benetazzo, A., Cavaleri, L., Ma, H., Jiang, S., Bergamasco, F., Jiang, W., ...
855 Qiao, F. (2019). Analysis of the effect of fish oil on wind waves and im-
856 plications for air–water interaction studies. *Ocean Sci.*, *15*, 725–743. doi:
857 10.5194/os-15-725-2019
- 858 Blair, D., Zheng, Y., & Bourassa, M. (2023). The effect of surface oil on ocean wind
859 stress. *Earth*, *4*, 345–364. doi: 10.3390/earth4020019
- 860 Booij, N., Ris, R., & Holthuijsen, L. (1999). A third-generation wave model for
861 coastal regions: 1. Model description and validation. *J. Geophys. Res.*, *104C*,
862 7649–7666. doi: 10.1029/98JC02622

- 863 Bourassa, M., Vincent, D., & Wood, W. (1999). A flux parameterization including
 864 the effects of capillary waves and sea state. *J. Atmos. Sci.*, *56*, 1123–1139. doi:
 865 10.1175/1520-0469(1999)056<1123:AFPITE>2.0.CO;2
- 866 Boutin, G., Lique, C., Arduin, F., Rousset, C., Talandier, C., Accensi, M., &
 867 Girard-Arduin, F. (2020). Towards a coupled model to investigate wave–sea
 868 ice interactions in the Arctic marginal ice zone. *The Cryosphere*, *14*, 709–735.
 869 doi: 10.5194/tc-14-709-2020
- 870 Bradtke, K., & Herman, A. (2023). Spatial characteristics of frazil streaks in the
 871 Terra Nova Bay polynya from high-resolution visible satellite imagery. *The*
 872 *Cryosphere*, *17*, 2073–2094. doi: 10.5194/tc-17-2073-2023
- 873 Cheng, S., Rogers, W., Thomson, J., Smith, M., Doble, M., Wadhams, P., . . . Shen,
 874 H. (2017). Calibrating a viscoelastic sea ice model for wave propagation in
 875 the Arctic fall marginal ice zone. *J. Geophys. Res.*, *122*, 8740–8793. doi:
 876 10.1002/2017JC013275
- 877 Ciappa, A., & Pietranera, L. (2013). High resolution observations of the Terra Nova
 878 Bay polynya using COSMO-SkyMed X-SAR and other satellite imagery. *J.*
 879 *Marine Systems*, *113–114*, 42–51. doi: 10.1016/j.jmarsys.2012.12.004
- 880 Collins, C., & Rogers, W. (2017). *A source term for wave attenuation by sea ice in*
 881 *WAVEWATCH III: IC4* (Tech. Rep. Nos. NRL/MR/7320–17-9726). Naval Re-
 882 search Laboratory. (25 pp.)
- 883 Collins, C., Rogers, W., & Lund, B. (2017). An investigation into the dispersion of
 884 ocean surface waves in sea ice. *Ocean Dynamics*, *67*, 263–280. doi: 10.1007/
 885 s10236-016-1021-4
- 886 Cox, C., Zhang, X., & Duda, T. (2017). Suppressing breakers with polar oil films:
 887 Using an epic sea rescue to model wave energy budgets. *Geophys. Res. Lett.*,
 888 *44*, 1414–1421. doi: 10.1002/2016GL071505
- 889 Deike, L., Berhanu, M., & Falcon, E. (2017). Experimental observation of hydroe-
 890 lastic three-wave interactions. *Phys. Rev. Fluids*, *2*, 064803. doi: 10.1103/
 891 PhysRevFluids.2.064803
- 892 Dumont, D. (2022). Marginal ice zone dynamics: history, definitions and research
 893 perspectives. *Phil. Trans. Royal Soc. A*, *380*, 20210253. doi: 10.1098/rsta.2021
 894 .0253
- 895 Eicken, H., & Lange, M. (1989). Development and properties of sea ice in the coastal
 896 regime of the Southeastern Weddell Sea. *J. Geophys. Res.*, *94*, 8193–8206. doi:
 897 10.1029/JC094iC06p08193
- 898 Garbrecht, T., Lüpkes, C., Hartmann, J., & Wolff, M. (2002). Atmospheric drag co-
 899 efficients over sea ice – validation of a parameterisation concept. *Tellus*, *54A*,
 900 205–219.
- 901 Gemmrich, J., Banner, M., & Garrett, C. (2008). Spectrally resolved energy dissipa-
 902 tion rate and momentum flux of breaking waves. *J. Phys. Oceanogr.*, *38*, 1296–
 903 1312. doi: 10.1175/2007JPO3762.1
- 904 Guest, P. (2021a). Inside katabatic winds over the Terra Nova Bay Polynya: 1.
 905 Atmospheric jet and surface conditions. *J. Geophys. Res.: Atmospheres*, *126*,
 906 e2021JD034902. doi: 10.1029/2021JD034902
- 907 Guest, P. (2021b). Inside katabatic winds over the Terra Nova Bay Polynya: 2.
 908 Dynamic and thermodynamic analyses. *J. Geophys. Res.: Atmospheres*, *126*,
 909 e2021JD034904. doi: 10.1029/2021JD034904
- 910 Hasselmann, S., Hasselmann, K., Allender, J., & Barnett, T. (1985). Compu-
 911 tations and parameterizations of the nonlinear energy transfer in a grav-
 912 ity wave spectrum. Part II: Parameterizations of the nonlinear transfer
 913 for application in wave models. *J. Phys. Oceanogr.*, *15*, 1378–1391. doi:
 914 10.1175/1520-0485(1985)015<1378:CAPOTN>2.0.CO;2
- 915 Herman, A. (2021). Spectral wave energy dissipation due to under-ice turbulence. *J.*
 916 *Phys. Oceanogr.*, *51*, 1177–1186. doi: 10.1175/JPO-D-20-0171.1
- 917 Herman, A., & Bradtke, K. (2023). *SWAN wave model simulations of the Terra*

- 918 *Nova Bay Polynya*. Data set, Zenodo. doi: 10.5281/zenodo.8308164
- 919 Herman, A., Dojczman, M., & Świszcz, K. (2020). High-resolution simulations of in-
 920 teractions between surface ocean dynamics and frazil ice. *The Cryosphere*, *14*,
 921 3707–3729. doi: 10.5194/tc-14-3707-2020
- 922 Hollands, T., & Dierking, W. (2016). Dynamics of the Terra Nova Bay Polynya:
 923 The potential of multi-sensor satellite observations. *Remote Sens. Environ.*,
 924 *187*, 30–48. doi: 10.1016/j.rse.2016.10.003
- 925 Holthuijsen, L. (2007). *Waves in oceanic and coastal waters*. Cambridge Univ. Press.
 926 (387 pp.)
- 927 Janssen, P., & Bidlot, J.-R. (2023). Wind–wave interaction for strong winds. *J.*
 928 *Phys. Oceanogr.*, *53*, 779–804. doi: 10.1175/JPO-D-21-0293.1
- 929 Janssen, P., Lionello, P., & Zambresky, L. (1989). On the interaction of wind and
 930 waves. *Phil. Trans. Royal Soc. A*, *329*, 289–301. doi: 10.1098/rsta.1989.0077
- 931 Kohout, A., Smith, M., Roach, L., Williams, G., Montiel, F., & Williams, M. (2020).
 932 Observations of exponential wave attenuation in Antarctic sea ice during the
 933 PIPERS campaign. *Ann. Glaciology*, *61*, 196–209. doi: 10.1017/aog.2020.36
- 934 Komen, G., Hasselmann, S., & Hasselmann, K. (1984). On the existence of a fully
 935 developed wind-sea spectrum. *J. Phys. Oceanogr.*, *14*, 1271–1285. doi: 10
 936 .1175/1520-0485(1984)014(1271:OTEOAF)2.0.CO;2
- 937 Li, J., Kohout, A., & Shen, H. (2015). Comparison of wave propagation through ice
 938 covers in calm and storm conditions. *Geophys. Res. Lett.*, *42*, 5935–5941. doi:
 939 10.1002/2015GL064715
- 940 Liu, Q., Rogers, W., Babanin, A., Li, J., & Guan, C. (2020). Spectral modeling of
 941 ice-induced wave decay. *J. Phys. Oceanogr.*, *50*, 1583–1604. doi: 10.1175/JPO
 942 -D-19-0187.1
- 943 Lüpkes, C., & Birnbaum, G. (2005). Surface drag in the Arctic marginal sea-ize
 944 zone: Comparison of different parameterisation concepts. *Bound. Layer Meteoro-*
 945 *rol.*, *117*, 179–211.
- 946 Lüpkes, C., Gryanik, V., Hartmann, J., & Andreas, E. (2012). A parametrization,
 947 based on sea ice morphology, of the neutral atmospheric drag coefficients for
 948 weather prediction and climate models. *J. Geophys. Res.*, *117*, D13112. doi:
 949 10.1029/2012JD017630
- 950 Mchedlishvili, A., Lüpkes, C., Petty, A., Tsamados, M., & Spreen, G. (2023).
 951 New estimates of the pan-Arctic sea ice-atmosphere neutral drag coeffi-
 952 cients from ICESat-2 elevation data. *EGUsphere, preprint*. doi: 10.5194/
 953 egusphere-2023-187
- 954 Meylan, M., Bennetts, L., & Kohout, A. (2014). In situ measurements and analy-
 955 sis of ocean waves in the Antarctic marginal ice zone. *Geophys. Res. Lett.*, *41*,
 956 5046–5051. doi: 10.1002/2014GL060809
- 957 Meylan, M., Bennetts, L., Mosig, J., Rogers, W., Doble, M., & Peter, M. (2018).
 958 Dispersion relations, power laws, and energy loss for waves in the marginal ice
 959 zone. *J. Geophys. Res.*, *123*, 3322–3335. doi: 10.1002/2018JC013776
- 960 Montiel, F., Kohout, A., & Roach, L. (2022). Physical drivers of ocean wave attenu-
 961 ation in the marginal ice zone. *J. Phys. Oceanogr.*, *52*, 889–906. doi: 10.1175/
 962 JPO-D-21-0240.1
- 963 Morales Maqueda, M., Willmott, A., & Biggs, N. (2004). Polynya dynamics: A re-
 964 view of observations and modeling. *Rev. Geophys.*, *42*, RG1004. doi: 10.1029/
 965 2002RG000116
- 966 Nakata, K., Ohshima, K., & Nihashi, S. (2021). Mapping of active frazil for Antarc-
 967 tic coastal polynyas, with an estimation of sea-ice production. *Geophys. Res.*
 968 *Lett.*, *48*, e2020GL091353. doi: 10.1029/2020GL091353
- 969 Powers, J., Manning, K., Bromwich, D., Cassano, J., & Cayette, A. (2012). A
 970 decade of Antarctic science support through AMPS. *Bull. Am. Meteorol. Soc.*,
 971 *93*(11), 1699–1712. doi: 10.1175/BAMS-D-11-00186.1
- 972 Roach, L., Bitz, C., Horvat, C., & Dean, S. (2019). Advances in modeling inter-

- 973 actions between sea ice and ocean surface waves. *J. Advances Mod. Earth Sys-*
 974 *tems*, *11*, 4167–4181. doi: 10.1029/2019MS001836
- 975 Roach, L., Horvat, C., Dean, S., & Bitz, C. (2018). An emergent sea ice floe size
 976 distribution in a global coupled ocean–sea ice model. *J. Geophys. Res.*, *123*,
 977 4322–4337. doi: 10.1029/2017JC013692
- 978 Rogers, W. (2019). *Implementation of sea ice in the wave model SWAN* (Tech. Rep.
 979 Nos. NRL/MR/7322–19-9874). Naval Research Laboratory, USA. (25 pp.)
- 980 Rogers, W., Hwang, P., & Wang, D. (2003). Investigation of wave growth and decay
 981 in the SWAN model: three regional-scale applications. *J. Phys. Oceanogr.*, *33*,
 982 366–389. doi: 10.1175/1520-0485(2003)033<0366:IOWGAD>2.0.CO;2
- 983 Rogers, W., Meylan, M., & Kohout, A. (2018). *Frequency distribution of dissipation*
 984 *of energy of ocean waves by sea ice using data from Wave Array 3 of the ONR*
 985 *“sea state” field experiment* (Tech. Rep. Nos. NRL/MR/7322–18-9801). Naval
 986 Research Laboratory, USA. (32 pp.)
- 987 Rogers, W., Meylan, M., & Kohout, A. (2021). Estimates of spectral wave attenua-
 988 tion in Antarctic sea ice, using model/data inversion. *Cold Regions Sci. Tech.*,
 989 *182*, 103198. doi: 10.1016/j.coldregions.2020.103198
- 990 Rogers, W., Posey, P., Li, L., & Allard, R. (2018). *Forecasting and hindcasting waves*
 991 *in and near the marginal ice zone: wave modeling and the ONR “sea state”*
 992 *field experiment* (Tech. Rep. Nos. NRL/MR/7320–18-9786). Naval Research
 993 Laboratory, USA. (183 pp.)
- 994 Rogers, W., Thomson, J., Shen, H., Doble, M., Wadhams, P., & Cheng, S. (2016).
 995 Dissipation of wind waves by pancake and frazil ice in the autumn Beaufort
 996 Sea. *J. Geophys. Res.*, *121*, 7991–8007. doi: 10.1002/2016JC012251
- 997 Shen, H. (2022). Wave-in-ice: theoretical bases and field observations. *Phil. Trans.*
 998 *Royal Soc. A*, *380*, 20210254. doi: 10.1098/rsta.2021.0254
- 999 Smith, M., & Thomson, J. (2016). Scaling observations of surface waves in the Beau-
 1000 fort Sea. *Elementa*, *4*, 000097. doi: 10.12952/journal.elementa.000097
- 1001 Smith, M., & Thomson, J. (2019a). Ocean surface turbulence in newly formed
 1002 marginal ice zones. *J. Geophys. Res.*, *124*, 1382–1398. doi: 10.1029/
 1003 2018JC014405
- 1004 Smith, M., & Thomson, J. (2019b). Pancake sea ice kinematics and dynamics us-
 1005 ing shipboard stereo video. *Annals Glaciology*, *61*, 1–11. doi: 10.1017/aog.2019
 1006 .35
- 1007 Squire, V. (2018). A fresh look at how ocean waves and sea ice interact. *Phil. Trans.*
 1008 *R. Soc. A*, *376*, 20170342. doi: 10.1098/rsta.2017.0342
- 1009 Squire, V. (2020). Ocean wave interactions with sea ice: A reappraisal. *Annu. Rev.*
 1010 *Fluid Mech.*, *52*, 37–60. doi: 10.1146/annurev-fluid-010719-060301
- 1011 Stopa, J., Ardhuin, F., Thomson, J., Smith, M., Kohout, A., Doble, M., & Wad-
 1012 hams, P. (2018). Wave attenuation through an Arctic marginal ice zone on 12
 1013 October 2015. 1. Measurement of wave spectra and ice features from Sentinel
 1014 1A. *J. Geophys. Res.*, *123*. doi: 10.1029/2018JC013791
- 1015 Stopa, J., Sutherland, P., & Ardhuin, F. (2018). Strong and highly variable push of
 1016 ocean waves on Southern Ocean sea ice. *Proc. Nat. Acad. Sci.*, *115*, 5861–5865.
 1017 doi: 10.1073/pnas.1802011115
- 1018 SWAN Team. (2022). *SWAN Cycle III, version 41.45, Scientific and Technical Doc-*
 1019 *umentation* (Tech. Rep.). Delft University of Technology, Faculty of Civil Engi-
 1020 neering and Geosciences.
- 1021 Thompson, L., Smith, M., Thomson, J., Stammerjohn, S., Ackley, S., & Loose,
 1022 B. (2020). Frazil ice growth and production during katabatic wind
 1023 events in the Ross Sea, Antarctica. *The Cryosphere*, *14*, 3329–3347. doi:
 1024 10.5194/tc-14-3329-2020
- 1025 Van der Westhuijsen, A., Zijlema, M., & Battjes, J. (2007). Nonlinear saturation-
 1026 based whitening dissipation in SWAN for deep and shallow water.
 1027 *Coastal Engng.*, *54*, 151–170. doi: 10.1016/j.coastaleng.2006.08.006

- 1028 Van Vledder, G. P. (2006). The WRT method for the computation of non-linear
1029 four-wave interactions in discrete spectral wave models. *Coastal Engng*, *53*,
1030 223–242. doi: 10.1016/j.coastaleng.2005.10.011
- 1031 Voermans, J., Babanin, A., Thomson, J., Smith, M., & Shen, H. (2019). Wave atten-
1032 uation by sea ice turbulence. *Geophys. Res. Lett.*, *46*, 6796–6803. doi: 10.1029/
1033 2019GL082945
- 1034 Wadhams, P., Aulicino, G., Parmiggiani, F., Persson, P., & Holt, B. (2018). Pancake
1035 ice thickness mapping in the Beaufort Sea from wave dispersion observed in
1036 SAR imagery. *J. Geophys. Res.*, *123*, 2213–2237. doi: 10.1002/2017JC013003
- 1037 Yan, L. (1987). *An improved wind input source term for third generation ocean wave*
1038 *modelling* (Tech. Rep. Nos. 87–8). Royal Dutch Meteor. Inst. (20 pp.)
- 1039 Zhao, X., & Zhang, C. (2020). A theoretical model of wind-wave growth over an ice-
1040 covered sea. *Boundary Layer Meteorol.*, *178*, 1–19. doi: 10.1007/s10546-020-
1041 -00552-7
- 1042 Zheng, Y., Bourassa, M., & Hughes, P. (2013). Influence of sea surface temper-
1043 ature gradients and surface roughness changes on the motion of surface oil:
1044 a simple idealized study. *J. Applied Meteorol. Clim.*, *52*, 1561–1575. doi:
1045 10.1175/JAMC-D-12-0211.1
- 1046 Zijlema, M., van Vledder, G., & Holthuijsen, L. (2012). Bottom friction and wind
1047 drag for wave models. *Coastal Engng*, *65*, 19–26. doi: 10.1016/j.coastaleng
1048 .2012.03.002

Abstract

Sea ice–waves interactions have been widely studied in the marginal ice zone, at relatively low wind speeds and wave frequencies. Here, we focus on very different conditions typical of coastal polynyas: extremely high wind speeds and locally-generated, short, steep waves. We overview available parameterizations of relevant physical processes (nonlinear wave–wave interactions, energy input by wind, whitecapping and ice-related dissipation) and discuss modifications necessary to adjust them to polynya conditions. We use satellite-derived data and spectral modelling to analyze waves in ten polynya events in the Terra Nova Bay, Antarctica. We estimate the wind-input reduction factor over ice in the wave-energy balance equation at 0.56. By calibrating the model to satellite observations we show that exact treatment of quadruplet wave–wave interactions (as opposed to the default Discrete Interaction Approximation) is necessary to fit the model to data, and that the power $n > 4$ in the sea-ice source term $S_{\text{ice}} \sim f^n$ (where f denotes wave frequency) is required to reproduce the observed very strong attenuation in spectral tail in frazil streaks. We use a very-high resolution satellite image of a fragment of one of the polynyas to determine whitecap fraction. We show that there are more than twofold differences in whitecap fraction over ice-free and ice-covered regions, and that the model produces realistic whitecap fractions without any tuning of the whitecapping source term. Finally, we estimate the polynya-area-integrated wind input, energy dissipation due to whitecapping, and whitecap fraction to be on average below 25%, 10% and 30%, respectively, of the corresponding open-water values.

Plain Language Summary

As ocean waves propagate through areas covered with sea ice, they both affect and are affected by the ice. Until recently, wave–ice interactions have been analyzed in the so-called marginal ice zone (MIZ), the external part of sea ice cover neighboring the open ocean. In this work, we study a largely unexplored case of wave–ice interactions that take place in Antarctic coastal polynyas at extremely high wind speeds (often exceeding 100 kph) and low air temperatures (often below -20°C). These waves are very different from those in the MIZ and therefore allow us to learn new aspects of the physics of wave growth and dissipation in sea ice. In our study we use numerical wave modeling and satellite data analysis, and seek optimal combinations of model settings to reproduce the observations. For example, we determine a scaling factor that describes how the energy input from wind is reduced over polynyas due to the presence of the ice. We also show that sea ice reduces wave breaking – and that the model is able to reproduce this effect. Taken together, our results contribute not only to a better understanding of polynya dynamics, but also to more reliable modeling of waves in sea ice in general.

1 Introduction

Interactions between sea ice and ocean surface waves have been in recent years extensively studied theoretically, observationally and numerically (Squire, 2018, 2020; Liu et al., 2020; Shen, 2022, and references there). Significance of waves–ice interactions for short-term dynamics of sea ice and the upper ocean, and for longer-term evolution of sea ice cover in (sub)polar regions has been demonstrated in a number of studies (e.g., Roach et al., 2018, 2019; Boutin et al., 2020). The main focus of waves-in-ice research has been on attenuation of ocean waves in sea ice, caused by energy-conserving scattering and/or dissipation within and under the ice. Importantly, the evolution of wave energy spectra in sea ice is usually analyzed on a component-by-component basis, that is, attenuation coefficients are estimated from pairs of observed spectra at two different locations separately for individual frequency bins (e.g., Cheng et al., 2017; Stopa, Sutherland, & Ardhuin, 2018; Kohout et al., 2020; Alberello et al., 2022), disregarding energy exchange between spectral components that is crucial for evolution of ocean surface waves in open

64 water (e.g., Holthuijsen, 2007). These empirically determined apparent attenuation co-
 65 efficients are then implemented in spectral wave models (e.g., Collins & Rogers, 2017;
 66 Rogers, 2019). Not surprisingly, measurements made in different ice types (frazil, grease
 67 ice, pancakes, ice floes, etc.) and ice thickness lead to different estimations of those co-
 68 efficients (see Rogers, Meylan, & Kohout, 2018, for an overview). A more serious prob-
 69 lem with this approach is that the apparent attenuation represents not only sea-ice re-
 70 lated scattering and dissipation, but is a net effect of all processes involved, including
 71 wind-wave growth, dissipation unrelated to ice, and nonlinear wave-wave interactions.
 72 Arguably, disentangling sea ice effects from the net attenuation requires a combination
 73 of process-oriented observations and theoretical models capturing the underlying physics.
 74 In spite of some recent progress in this respect (see, e.g., Voermans et al., 2019; Smith
 75 & Thomson, 2019a, 2019b; Herman, 2021), the goal of making the spectral wave mod-
 76 els in sea ice comparably versatile as they are in open water remains a big challenge.

77 In attempts to achieve that goal it is important to collect data from a wide range
 78 of waves-in-ice conditions. At present, a serious limitation is the fact that our understand-
 79 ing of sea ice-waves interactions is based exclusively on data from and models of the marginal
 80 ice zone (MIZ; Dumont, 2022). The focus on the MIZ implies that our observations and
 81 modelling efforts are limited to a certain range of conditions typical for this environment.
 82 In particular, waves in the MIZ tend to have low u_*/c ratios (where u_* denotes the fric-
 83 tion velocity of the wind at the sea surface, and c is wave phase speed; the ratio u_*/c
 84 is an inverse of the wave age). In the MIZ typically $u_*/c \ll 0.1$ for wave frequencies
 85 at and close to the spectral peak. This means that these waves are weakly forced by wind
 86 (Janssen et al., 1989) and, consequently, have low steepness and do not break. As a re-
 87 sult, in the spectral energy balance the wind input and wave breaking terms are domi-
 88 nated by terms representing dissipation and scattering in sea ice. It is noteworthy that
 89 situations deviating from that picture (e.g., those with negative apparent attenuation
 90 indicating dominance of wave growth over dissipation) are often removed from the ob-
 91 servations prior to the analysis (e.g., Cheng et al., 2017).

92 As a step towards broadening the picture and extending wave-ice interactions anal-
 93 yses to a wider range of conditions, we turn our attention towards a setting with features
 94 that in many ways are the opposite of the MIZ-typical conditions described above: coastal
 95 (or latent heat) polynyas during catabatic wind events (Morales Maqueda et al., 2004).
 96 Polynya openings are associated with very high wind speeds, often exceeding $30 \text{ m}\cdot\text{s}^{-1}$,
 97 and advection of very cold and dry continental air masses, resulting in offshore drift of
 98 the ice pack and extremely high ocean-atmosphere turbulent heat and moisture fluxes
 99 (up to $2000 \text{ W}\cdot\text{m}^{-2}$; Guest, 2021a, 2021b). All these factors combined lead to strong tur-
 100 bulance and convective, wind- and wave-induced mixing in the ocean mixed layer (OML;
 101 Herman et al., 2020), and to intense frazil ice formation (Thompson et al., 2020; Nakata
 102 et al., 2021). Crucially for this study, waves in coastal polynyas are young, fetch-limited,
 103 strongly forced ($u_*/c > 0.1$), and therefore short and steep, with a strong tendency to
 104 break. Over most of polynya area, energy input from the wind dominates over the net
 105 dissipation, so that the wave energy grows with offshore distance in spite of increasing
 106 ice concentration. Moreover, the sea surface in polynyas is a complex mosaic of open-
 107 water areas and patches of young (frazil, grease and shuga) ice forming characteristic elon-
 108 gated streaks (Eicken & Lange, 1989; Ciappa & Pietranera, 2013; Hollands & Dierking,
 109 2016; Thompson et al., 2020). The properties of those streaks in one of the most widely
 110 studied Antarctic coastal polynyas, the Terra Nova Bay Polynya (TNBP; Fig. 1), have
 111 been recently analyzed by Bradtke and Herman (2023). One of the findings of this pre-
 112 vious study was a significant slowdown of the observed wave growth in the analyzed polynya
 113 events in comparison to the expected open-water wave growth under given wind condi-
 114 tions, an effect that can be attributed only to wave-ice interactions. Inspired by this find-
 115 ing, in this work we conduct an extensive analysis of wave evolution in a series of TNBP
 116 events, based on the results from Bradtke and Herman (2023), an additional satellite data
 117 source providing information on wave breaking patterns, and spectral wave modelling.

118 The overall influence of frazil streaks on waves and, more generally, on the sea sur-
 119 face properties has been described in several earlier studies based on qualitative visual
 120 observations (e.g., Ciappa & Pietranera, 2013; Hollands & Dierking, 2016; Ackley et al.,
 121 2022). Rapid attenuation of short waves in streaks, attributable to a high bulk viscos-
 122 ity of grease ice, leads to a reduction of surface roughness (and thus wind friction veloc-
 123 ity u_*), decrease of the mean wave steepness, and weakening of wave breaking and white-
 124 cap generation (Ackley et al., 2022), thus reducing the sea spray generation and the spray-
 125 associated component of the ocean-atmosphere turbulent heat flux (Guest, 2021b). The
 126 question how to quantify and parameterize these effects and, crucially, how they influ-
 127 ence the spatial evolution of the polynya wave field – with feedbacks to sea ice thermo-
 128 dynamics and dynamics – remains to be answered. In this study, we make the first at-
 129 tempt at estimating the role of individual source terms in the wave-energy balance in
 130 shaping the polynya wave fields. We use the satellite-derived ice concentration and wave
 131 data from Bradtke and Herman (2023), combined with wind fields from a regional weather
 132 model, to set up and calibrate a spectral wave model of the TNBP, for ten polynya events
 133 from the period 2016–2021. We review the available formulations of the relevant source
 134 terms – wind input, deep-water dissipation, quadruplet wave-wave interactions, and at-
 135 tenuation in sea ice – and seek the combination of model settings that best reproduces
 136 observations. We also discuss the (numerous) uncertainties and limitations of the avail-
 137 able observations and models. In our analysis, we pay particular attention to the influ-
 138 ence of frazil streaks on wave breaking. To this end, we adopted an image filtering tech-
 139 nique for detection of breakers in very-high resolution (0.5 m) visible satellite images of
 140 the sea surface. We then compare the spatial variability of two different, but closely re-
 141 lated variables – the satellite-derived surface area fraction covered by breakers, and the
 142 simulated wave energy dissipation due to whitecapping – and estimate the reduction of
 143 the total (polynya-surface-integrated) energy dissipation due to the presence of sea ice.

144 2 Data Sources and Processing

145 2.1 Ice concentration, wave properties and wind data

146 As mentioned in the introduction, this analysis is based on the data and results of
 147 Bradtke and Herman (2023). From the set of satellite images analyzed there, ten have
 148 been selected for the present study (Table 1, Supplementary Fig. S1), based on their suf-
 149 ficiently large spatial extent (given the images’ resolution of 10 m, no reliable wave in-
 150 formation can be obtained from nearshore areas and from relatively small polynyas due
 151 to too small wavelength-to-pixel-size ratios). The ten images were obtained with two satel-
 152 lite sensors: OLI (Operational Land Imager) and MSI (Multispectral Instrument) on board
 153 Landsat-8 and Sentinel-2 satellites, respectively. All details related to image processing
 154 and analysis can be found in Bradtke and Herman (2023) and are not repeated here. The
 155 data used in this study include, for each polynya, maps of polynya extent, ice concen-
 156 tration A , and peak wavelength L_p (and the corresponding deep-water wave period T_p
 157 and frequency $f_p = T_p^{-1}$). As discussed in Bradtke and Herman (2023), the peak wave-
 158 length, together with wave direction at the spectral peak (not considered here), are two
 159 spectral characteristics that can be robustly determined from visible satellite imagery.
 160 Indisputably, the lack of information on wave heights and the shape of the tails of the
 161 spectra is a serious limitation. However, as the analysis in the following sections will show,
 162 spatial variability of T_p alone provides valuable insight into the properties of the under-
 163 lying wave field and, crucially, constrains the possible combinations of the adjustable pa-
 164 rameters in spectral modelling, thus allowing inferences about individual physical pro-
 165 cesses at play.

166 The results of the Antarctic Mesoscale Prediction System (AMPS; Powers et al.,
 167 2012, <https://www.earthsystemgrid.org/project/amps.html>) are used as a source
 168 of surface atmospheric data. Results from a nested subdomain (the so called Ross Island
 169 grid) are used, with resolution of 1.1 km in 2016 and 0.89 km in 2019–2021. For each

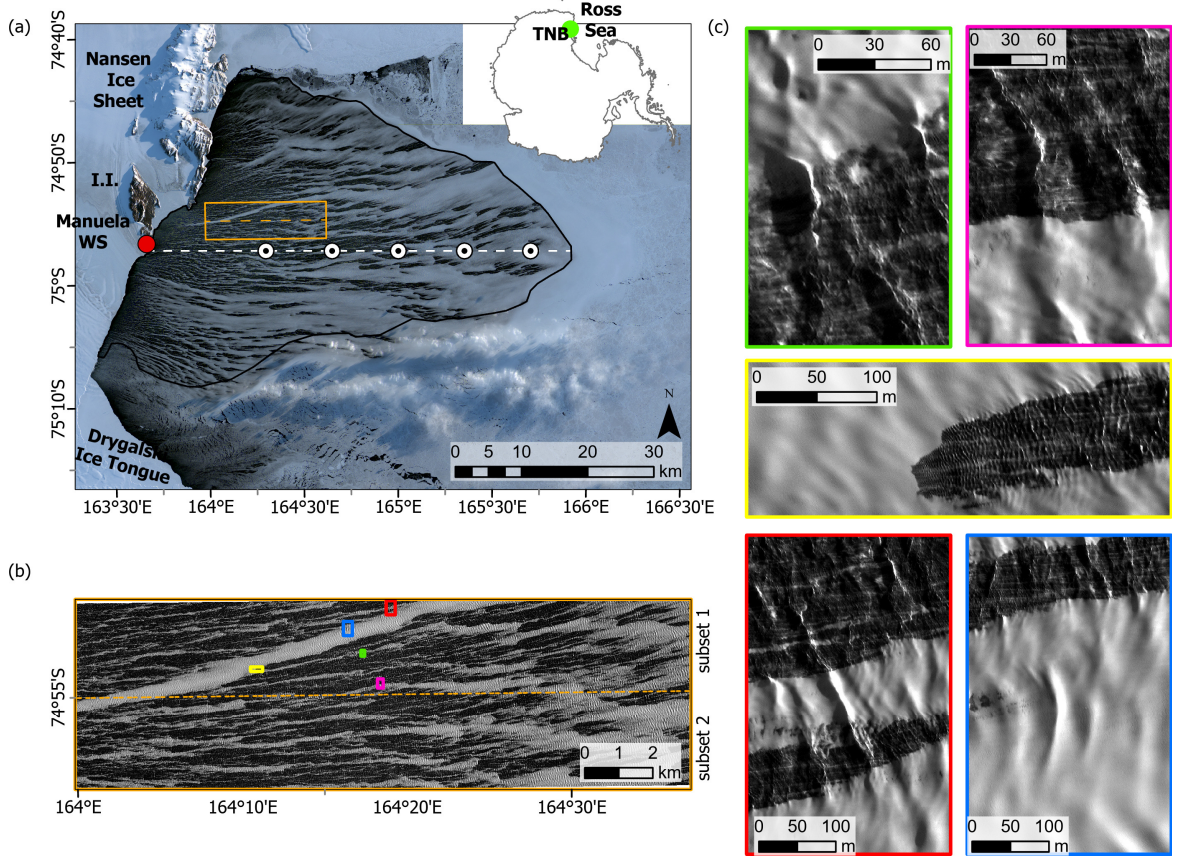


Figure 1. (a) Location of the TNBP and spatial distribution of sea ice on 19 Sep. 2019 on the Sentinel-2 MSI RGB composite (Copernicus Sentinel data 2019); the outline of the polynya and the location of the Manuela weather station on Inexpressible Island (I.I.) are marked with the black polygon and red dot, respectively. The orange rectangle shows extent of the analyzed subsets of WorldView-2 Panchromatic image (imagery © 2019 Maxar Technologies), fragments of which are zoomed in panels (b) and (c). The dashed white line and white dots in (a) show the location of the transect and points at which the results are analyzed in section 4.

Table 1. Summary of polynya events analyzed in this study

Date	Time (UTC)	Sensor	$T_{a,M}$ (°C)	$U_{w,M}$ (m·s ⁻¹)	$\theta_{w,M}$ (degr)	S_p (km ²)	L_e (km)	L_c (km)
2016-10-05	2120	MSI	-22.5	24.1	260	1043	36.2	63.7
2016-10-06	2050	MSI	-24.6	25.4	262	740	40.8	62.3
2016-10-17	2050	OLI	-21.4	28.4	261	1110	33.8	46.7
2016-10-22	2110	MSI	-22.3	21.3	259	975	28.3	46.8
2016-10-24	2100	OLI	-17.4	28.7	257	1762	53.3	55.2
2019-09-19	2100	MSI	-26.5	33.8	258	1920	56.3	50.0
2019-09-29	2110	OLI	-23.4	32.4	250	1729	45.4	57.9
2020-10-19	2100	OLI	-26.2	23.5	261	674	36.2	46.9
2020-10-26	2100	OLI	-20.6	23.3	266	1648	39.5	65.7
2021-10-07	2130	MSI	-23.2	28.1	272	736	35.5	52.2

$T_{a,M}$, $U_{w,M}$, $\theta_{w,M}$ – air temperature, wind speed and direction, respectively, at the Manuela weather station; S_p – polynya surface area; L_e and L_c – polynya extent in cross-shore and along-shore direction, respectively.

170 polynya, 9-hour forecasts from 12 UTC valid for 21 UTC were selected, i.e., the time clos-
 171 est to the acquisition time of the satellite scenes (Table 1). The 2-m AMPS wind vec-
 172 tors were recomputed onto the 10-m height with the algorithm based on the Monin–Obukhov
 173 similarity theory, as described in Guest (2021b). (Note that the measured wind data from
 174 the Manuela weather station in Table 1 are provided for informative purpose only; the
 175 wave modelling is based exclusively on the spatially-variable AMPS wind fields.)

176 2.2 Wave breaking patterns

177 The only additional source of satellite data used here, but not in Bradtke and Her-
 178 man (2023), is a very-high resolution panchromatic (PAN) satellite image taken by the
 179 WorldView-2 (WV2) satellite (imagery © 2019 Maxar Technologies) showing a fragment
 180 of the polynya from 19. Sep. 2019 (see Figs. 1 and 2 for a location and for zoomed frag-
 181 ments). The image was acquired at 21:22 UTC, i.e., 22 minutes after the correspond-
 182 ing MSI image, but considering the stable wind and air temperature forcing on that day
 183 it is reasonable to assume that the wave and sea ice conditions were very similar as well.
 184 We analyze a fragment of the scene taken by the satellite which covers an area of $18.3 \times 5.5 \text{ km}^2$.
 185 We use the standard LV2A product, without atmospheric correction, georeferenced and
 186 resampled to a grid of 0.5-m (the viewing geometry provides effective resolution of 0.53 m)
 187 in UTM zone 58S projection. Due to the small size of the analyzed area and cloudless
 188 sky, it can be assumed that the influence of the atmosphere on the image brightness is
 189 spatially homogeneous. During the satellite overpass the sea surface was illuminated by
 190 the Sun from a direction of 54.1° (azimuth angle) and an elevation angle of 7.7° . With
 191 the predominant direction of wave propagation towards the east (see Supplementary Fig.
 192 S1), this geometry of illumination causes shadowing of the windward slopes of steep waves.
 193 This makes it easier to identify them on a satellite image. However, the limited avail-
 194 ability of light makes it impossible to analyze features occurring in shadowed areas of
 195 open water.

196 As can be seen on the WV2 image (Fig. 2), whitecaps strongly contrast with darker
 197 water, even if the water reflectance is raised by frazil ice. The lighting conditions make
 198 also the very bright crests of steep waves clearly visible against the background of the
 199 frazil streaks. Therefore, in order to detect potential breakers in the analyzed image, we
 200 were looking for sharp contrast between neighboring pixels by applying a moving-window
 201 filter that calculates the sum of differences between a given pixel and the eight nearest
 202 pixels in the directions between 225° and 315° (SW to NW). Initially, the panchromatic
 203 image was de-noised with an edge-preserving filter. Pixels for which the calculated con-
 204 trast value was higher than the image average by more than 3 standard deviations (the
 205 same threshold for the whole image) were identified as sharply contrasted objects. To
 206 limit false alarms, only those objects that met the size criterion (more than 3 pixels con-
 207 nected by sides or corners) and contained bright pixels (the brightness threshold was de-
 208 termined by unsupervised ISODATA classification of the de-noised PAN image) were con-
 209 sidered as potential breakers (Fig. 2). In the next step, the surface area of pixels recog-
 210 nized as breakers was used to calculate whitecap fraction W within $200 \times 200 \text{ m}^2$ grid cells
 211 snapped to the grid of the wave model (see further section 3.3); and zonal fraction W_X
 212 was calculated in vertical zones 200 m wide, oriented perpendicularly to the x_{UTM} axis.
 213 Due to differences in spatial patterns of frazil streaks in the upper and lower parts of the
 214 PAN image, it was divided into 2 subsets (see Fig. 1b) and zonal statistics were calcu-
 215 lated for each of them separately. Finally, ice–water mask derived from WV2 data was
 216 used to calculate whitecap fraction W_X separately for ice-free and ice-covered regions,
 217 respectively.

218 Due to the lack of independent observations that could be used to validate our al-
 219 gorithm, its adjustable parameters have been selected in such a way that, first, the out-
 220 lines of detected breakers (Fig. 2) correspond as close as possible to a visual assessment
 221 by a human observer, and second, if any bias in the results is present, it is towards overde-

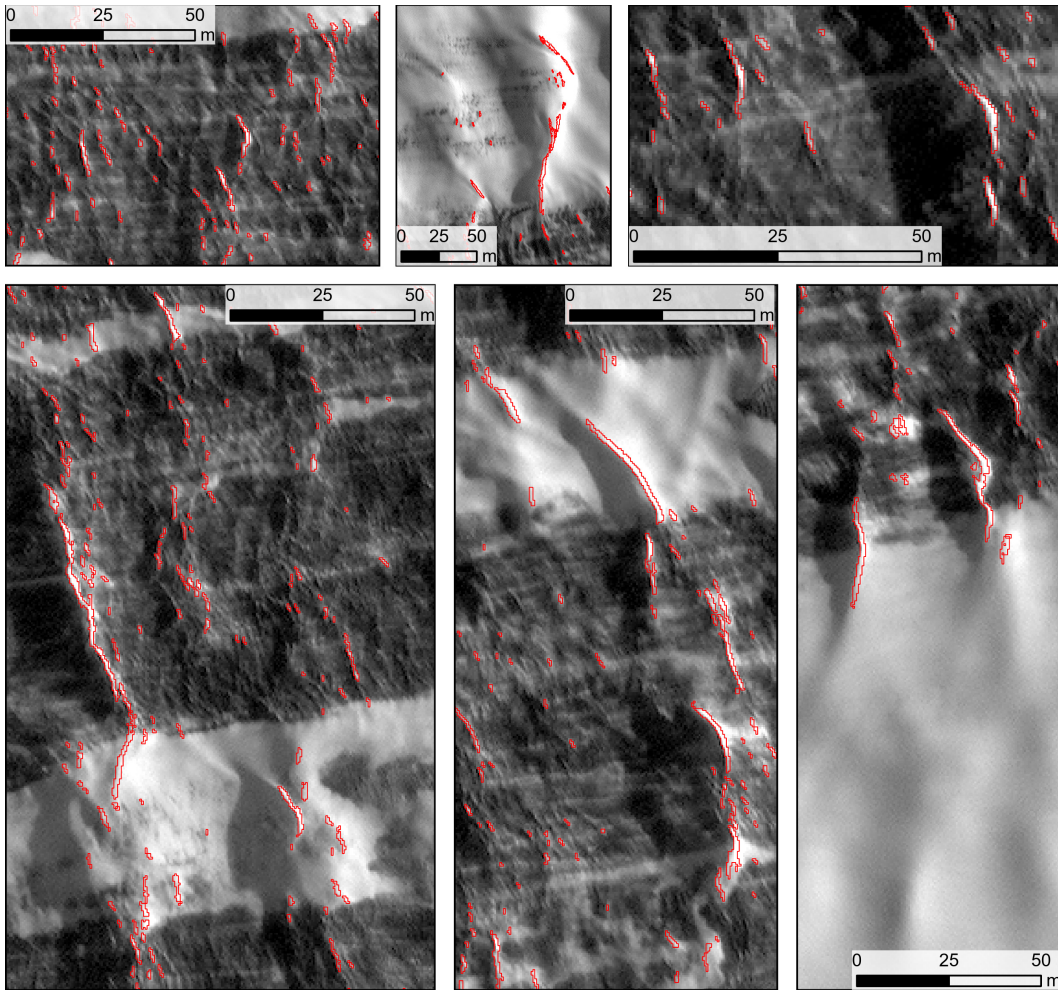


Figure 2. Zoomed fragments of WorldView-2 Panchromatic image (Imagery ©2019 Maxar Technologies) showing variability in pixel brightness due to the presence of frazil ice, waves and effects of their breaking. Outlines of detected breakers are marked in red.

222 tecton in ice and underdetection in water rather than *vice versa*. Thus, in spite of un-
 223 avoidable uncertainties, the differences between ice-covered and ice-free regions can be
 224 treated as reliable and under- rather than overestimated.

225 Image processing and visualization was performed with the Trimble eCognition De-
 226 veloper and ESRI ArcGIS Pro software.

227 3 Spectral Wave Modeling

228 3.1 Definitions and assumptions

229 Let us consider a stationary wave field described by spatially variable wave energy
 230 spectra $E(\mathbf{x}, f, \theta)$, where \mathbf{x} is location in horizontal space, and f, θ are wave frequency
 231 and propagation direction, respectively. Let us further assume that the waves are forced
 232 by time-independent wind with 10-m speed $u_{10}(\mathbf{x})$ and direction $\theta_w(\mathbf{x})$, and that the wa-
 233 ter depth is large, so that refraction, bottom friction and other processes related to wave-

234 bottom interactions can be omitted. The wind-induced, tidal and other currents are omit-
 235 ted as well. Finally, let the sea ice concentration be described by $A(\mathbf{x})$.

236 Under these assumptions, the wave energy conservation equation (e.g., Holthuijsen,
 237 2007) reduces to:

$$\mathbf{c}_g \cdot \nabla E = [1 - A + a_{\text{in}}A]S_{\text{in}} + S_{\text{ds}} + S_{\text{nl}} + AS_{\text{ice}}, \quad (1)$$

238 where $\mathbf{c}_g = c_g[\cos \theta, \sin \theta]$, $c_g = d\sigma/dk$ is the group velocity, and the angular frequency
 239 $\sigma = 2\pi f$ and wave number k fulfill the deep-water dispersion relation $\sigma^2 = gk$, with
 240 g gravitational acceleration. No changes of the dispersion relation due to the presence
 241 of frazil/grease ice are considered here – an assumption consistent with that of a low thick-
 242 ness and low Reynolds number of frazil/grease ice in streaks (e.g., Collins et al., 2017,
 243 note that observations and models of wave dispersion in frazil ice referred to in this and
 244 similar papers are limited to frazil/pancakes mixtures typical for freezing conditions in
 245 the MIZ – ice type that can be found in the outermost regions of polynyas, but not in
 246 their central parts of interest here). The source terms on the right-hand side of (1) de-
 247 scribe energy generation by wind S_{in} , deep-water dissipation S_{ds} , quadruplet wave–wave
 248 interactions S_{nl} , and attenuation by sea ice S_{ice} . As can be seen in (1), S_{ice} is scaled with
 249 ice concentration A . The coefficient $a_{\text{in}} \in [0, 1]$ allows for analogous scaling of S_{in} : the
 250 wind input is unaffected by ice if $a_{\text{in}} = 1$ and it equals zero over ice if $a_{\text{in}} = 0$. The
 251 two remaining source terms, S_{ds} , S_{nl} , are unaffected by the presence of the ice. Justi-
 252 fication for this treatment of source terms is provided below.

253 3.2 Overview of source terms formulations

254 In most spectral wave models (e.g., SWAN, WaveWatchIII, or WAM), several dif-
 255 ferent formulations of each source term in (1) are implemented. Their optimal choice de-
 256 pends on a particular application (domain size, water depth, expected u_*/c ratios, pres-
 257 ence of swell, etc.). Reviewing those formulations is out of the scope of this paper. In-
 258 stead, we concentrate here on selected parameterizations suitable for polynya conditions,
 259 with focus on those available in SWAN (Simulating Waves Nearshore; Booij et al., 1999),
 260 which is the model used in our simulations. Whenever several choices seem adequate,
 261 the more widely used ones (or, preferably, default) are selected.

262 3.2.1 S_{nl}

263 Starting with the S_{nl} term, it is important to recall that the nonlinear wave–wave
 264 interactions are inherently related to the dispersion relation of waves or, more precisely,
 265 to the existence of certain combinations of wavenumber vectors and wave frequencies among
 266 the components of the wave energy spectra (resonance conditions; see, e.g., Holthuijsen,
 267 2007). Therefore, as long as the assumptions made in section 3.1 hold (large water depth
 268 and validity of the open-water dispersion relation in frazil streaks), it is reasonable to
 269 assume that the quadruplet wave–wave interactions remain “active” and can be com-
 270 puted in the same way in ice-covered and ice-free areas (it should be noted, however,
 271 that in different ice types different types of nonlinear interactions may occur, e.g. tri-
 272 ads in fields of large floes in which hydroelastic effects are significant, see, e.g., Deike et
 273 al., 2017).

274 In SWAN and other spectral wave models, the DIA (discrete interaction approx-
 275 imation) by Hasselmann et al. (1985) is the default way of computing S_{nl} . Out of the
 276 very large number of quadruplet combinations in a given energy spectrum, DIA consid-
 277 ers only two quadruplets for each spectral component (see SWAN Team, 2022, for de-
 278 tails of DIA and its implementation in SWAN). Without making premature references
 279 to our model setup and simulations, we remark here that in spite of many attempts, we
 280 were unable to calibrate SWAN to the data when using DIA: the simulated wave peri-
 281 ods were strongly biased in a way that could not be reduced by any reasonable combi-

282 nation of tunable coefficients. Replacing the DIA with the near-exact method (Van Vled-
 283 der, 2006) removed the problems, suggesting that a careful treatment of quadruplet in-
 284 teractions is crucial for reproducing wave growth in polynyas (and in similar settings)
 285 with spectral wave models. This finding is not surprising if one considers the crucial role
 286 of nonlinear wave–wave interactions in modifying waves propagating through oil spills.
 287 Although energy dissipation within the oil layer is limited to very short waves, with fre-
 288 quencies well over 1 Hz (with particularly strong attenuation in the range 3.5–6.8 Hz due
 289 to Marangoni resonance), transfer of energy from lower frequencies to that highly dis-
 290 sipative frequency range by quadruplets leads to a very effective dissipation mechanism,
 291 attenuating waves with frequencies as low as 0.7 Hz (Alpers & Hühnerfuss, 1989; Bene-
 292 tazzo et al., 2019). How relevant similar combinations of processes are for sea ice remains
 293 to be studied. Notably, the importance of nonlinear interactions (combined with wind
 294 input) in reproducing the observed apparent attenuation rates of high-amplitude waves
 295 in the MIZ under storm conditions has been shown by Li et al. (2015).

296 3.2.2 S_{in} and S_{ds}

297 For S_{in} and S_{ds} – the two source terms that are very closely related in spectral wave
 298 models (Holthuijsen, 2007) – the formulation of Van der Westhuijsen et al. (2007) is se-
 299 lected. It combines wind input of Yan (1987) with nonlinear saturation-based whitecap-
 300 ping based on Alves and Banner (2003) and dissipation due to non-breaking waves based
 301 on Komen et al. (1984). Contrary to earlier models of whitecapping, which computed
 302 breaking probability from spectral-mean wave steepness (Komen et al., 1984), the for-
 303 mulation of Alves and Banner (2003) and the modified version of Van der Westhuijsen
 304 et al. (2007) used in SWAN make use of the observed links between wave breaking and
 305 wave groups. Accordingly, the so-called spectral saturation $B(k)$ – a measure of wave
 306 steepness – is computed from directionally-integrated spectrum $\bar{E}(f) \equiv \int_{\theta=0}^{2\pi} E(f, \theta) d\theta$
 307 within narrow frequency bands. Thus, dissipation is local in the wavenumber space. This
 308 is particularly relevant for the present case: it allows for breaking of short, steep, fast-
 309 growing waves in open-water patches between frazil streaks, even if the longer waves at
 310 the peak of the spectrum have milder slopes, so that the spectral-average wave steep-
 311 ness does not exceed the critical value. The older algorithms fail to reproduce this case
 312 of breaking limited to the narrow frequency range of the spectrum. Importantly as well,
 313 although S_{ds} is routinely referred to as the ‘whitecapping source term’, it is in fact sup-
 314 posed to represent all (largely unknown) deep-water dissipation mechanisms, including
 315 turbulence. S_{ds} is thus computed as a weighted sum of two contributions, whitecapping
 316 S_{wc} and dissipation unrelated to wave breaking S_{nbr} :

$$S_{\text{ds}} = f_{\text{br}} S_{\text{wc}} + (1 - f_{\text{br}}) S_{\text{nbr}}, \quad (2)$$

317 where $f_{\text{br}} \in [0, 1]$. For S_{wc} we have:

$$S_{\text{wc}} = -C_{\text{ds}} \left[\frac{B(k)}{B_r} \right]^{p/2} (gk)^{1/2} E(f, \theta), \quad (3)$$

318 where the saturation $B(k) = c_g k^3 \bar{E}(f)$, and C_{ds} , B_r and p are tuning coefficients (see
 319 SWAN Team, 2022, for their treatment in SWAN). Details of calculation of S_{nbr} and f_{br}
 320 can be found in the SWAN documentation. Crucially, in strongly forced, short waves an-
 321 alyzed here, $f_{\text{br}} \simeq 1$ over the whole energy-carrying wave frequency range (f between,
 322 approximately, 0.13 and 0.6 Hz), i.e., both around the peak and in the tail of the spec-
 323 trum (0.13 Hz is the lowest peak frequency found in satellite images analyzed in this study).
 324 Thus, $S_{\text{ds}} \simeq S_{\text{wc}}$. Under different conditions, when $f_{\text{br}} < 1$ and the contribution of
 325 S_{nbr} to S_{ds} is substantial, it might be suitable to multiply S_{nbr} by ice concentration A
 326 in order to turn off S_{nbr} over ice (reflecting the fact that frazil and grease ice suppresses
 327 turbulence due to its large viscosity). In our simulations it did not produce any notice-
 328 able differences in the results.

329 In general, very little is known about wave breaking in frazil and grease ice. As dis-
 330 cussed further in section 4.2 and as can be seen in Figs. 1 and 2, long waves do occasion-
 331 ally break within ice streaks in TNBP, although much less frequently than in the sur-
 332 rounding open water. As in the case of S_{nl} , we may seek analogies with oil slicks, for which
 333 available observations suggest that the oil’s high (and legendary) effectiveness in sup-
 334 pressing wave breaking is a secondary effect of other processes rather than a direct me-
 335 chanical response of the waves to the oil presence (e.g., Cox et al., 2017). For spectral
 336 modelling it means that – provided other source terms are properly computed – the ef-
 337 fect of reduced whitecap dissipation in ice-covered areas should be obtained as a mod-
 338 elling result in spite of S_{wc} being computed in the same way everywhere (note that this
 339 is the default setting in SWAN).

340 As for the wind input term S_{in} , its general form is:

$$S_{\text{in}} = \beta_{\text{in}} E, \quad \text{where} \quad \beta_{\text{in}} \equiv \beta_{\text{in}}(u_*/c, \theta_{\text{rel}}) \quad (4)$$

341 and where θ_{rel} is the angle between wind direction and propagation direction of the given
 342 spectral component. In the model of Yan (1987):

$$\beta_{\text{in}} = \max \left\{ \left[a_1 \left(\frac{u_*}{c} \right)^2 + a_2 \frac{u_*}{c} + a_3 \right] \cos \theta_{\text{rel}} + a_4, 0 \right\}. \quad (5)$$

343 The coefficients used in SWAN (recalibrated from the original ones by Van der West-
 344 huijsen et al., 2007) are: $a_1 = 4.0 \cdot 10^{-2}$, $a_2 = 5.52 \cdot 10^{-3}$, $a_3 = 5.2 \cdot 10^{-5}$, $a_4 = -3.02 \cdot$
 345 10^{-4} . An important advantage of this model is that, contrary to the earlier ones formu-
 346 lated for low wind speeds, it is suitable for strongly forced waves as well. As will be shown
 347 below, in polynyas this condition is fulfilled over most of both geographic and spectral
 348 space (i.e., the majority of polynya surface area, and energy-carrying wave frequency range),
 349 with an exception of the longest waves at the downwind end of the polynya.

350 For a given 10-m wind speed u_{10} , change in S_{in} due to the presence of sea ice may
 351 result from three factors: (i) change of the form of the β_{in} function (5); (ii) change of the
 352 wave phase speed c due to a modified dispersion relation in ice; and (iii) change of u_*
 353 due to a modified roughness of the surface. If we assume that expression (5) remains valid
 354 – to the best of our knowledge there are no data available that could be used to verify
 355 this assumption – and if we keep the assumption made earlier about the dispersion re-
 356 lation in polynyas, the only factor that remains is the surface drag. (Note that the in-
 357 flunce of the dispersion relation in sea ice on wind wave growth has been analyzed by
 358 Zhao & Zhang, 2020)

359 The relationship between u_* and u_{10} is $u_*^2 = C_{\text{D}} u_{10}^2$, where C_{D} is the 10-m drag
 360 coefficient. In spectral wave models, $C_{\text{D}} = C_{\text{Dn}}$, i.e. it represents the neutral drag co-
 361 efficient and it is a function of u_{10} only. The default $C_{\text{Dn}}(u_{10})$ relationship used in SWAN
 362 is by Zijlema et al. (2012), which reproduces the observed drop of surface drag at very
 363 high wind speeds (Janssen & Bidlot, 2023):

$$C_{\text{Dn}} = (0.55 + 2.97\tilde{u} - 1.49\tilde{u}^2) \cdot 10^{-3}, \quad \text{where} \quad \tilde{u} = u_{10}/u_{\text{ref}} \quad (6)$$

364 and $u_{\text{ref}} = 31.5 \text{ m}\cdot\text{s}^{-1}$ is a reference wind speed at which C_{Dn} reaches maximum. This
 365 formulation disregards possible spatial variability in surface properties, as well as effects
 366 of atmospheric stability – both factors which very likely are important in polynyas, with
 367 complicated spatial patterns of frazil–open water patches, and at air temperature T_{a} of-
 368 ten 20–30°C lower than the sea surface temperature $T_{\text{s}} \simeq -1.7^\circ\text{C}$ (see Table 2.1 for T_{a}
 369 during the analyzed events).

370 The wind drag over open ocean has been analyzed for many years under a wide range
 371 of wind and sea state conditions. Over vast areas of the oceans, especially far from the
 372 coasts and frontal zones, the assumption $C_{\text{D}} \simeq C_{\text{Dn}}$ is justified, because the air–sea tem-
 373 perature differences tend to be small. At very low air temperatures, however, the neg-

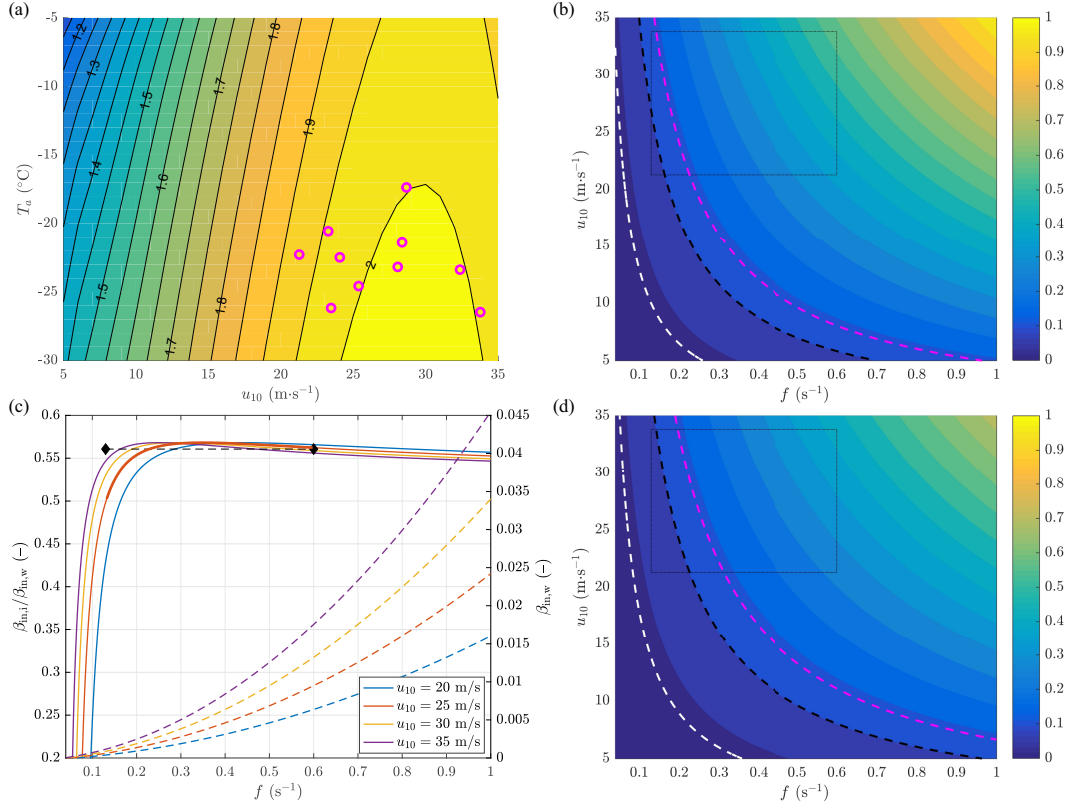


Figure 3. Surface drag and wind input over open water and sea ice. In (a), colors show the open-water surface drag coefficient $C_D(u_{10}, T_a)$ (in 10^3); magenta symbols mark the ten (u_{10}, T_a) combinations in the analyzed TNBP events (Table 1). In (b), colors show the open-water u_*/c ratio (–) in function of wave frequency f and wind speed u_{10} . The dashed contours mark: the value of $\beta_{in,w} = 0$ (white), $u_*/c = 0.1$ (black) and $u_*/c = a_2/a_1 \simeq 0.14$ (magenta). The dotted rectangle marks the approximate boundary of a region relevant for polynyas (see text for details). In (c), the ratio $\beta_{in,i}/\beta_{in,w}$ is shown for four selected values of wind speed (continuous lines; left axis), together with the corresponding curves for $\beta_{in,w}$ (dashed lines; right axis). The black line with diamonds shows the mean ratio $\beta_{in,i}/\beta_{in,w}$ at $u_{10} = 25$ m s $^{-1}$ within the frequency range $f \in [0.13, 0.6]$ Hz (thick red line). Panel (d) is analogous to (b), but for sea ice instead of open water. Note that all results in (a)–(d) are for $\theta_{rel} = 0$; they change very little for $|\theta_{rel}| < 30^\circ$.

374 active vertical stability of the lower atmosphere leads to a stronger ocean–atmosphere cou-
 375 pling and increased drag at the surface (an effect that, over polynyas, is partially reduced
 376 by very high wind speeds). For C_{Dn} given by (6), $C_D(u_{10}, T_a)$ can be determined using
 377 the Monin–Obukhov stability theory. The result is shown in Fig. 3a, together with the
 378 combinations of u_{10} and T_a in the analyzed polynya events (magenta symbols). As they
 379 all cluster at the plateau of relatively constant values of C_D , in the rest of this analy-
 380 sis we set, for the sake of simplicity, the open-water drag to $C_{Dw} = 2 \cdot 10^{-3}$.

381 Studies on the surface drag over an ice-covered ocean concentrate mainly on the
 382 Arctic ice pack and the MIZ, i.e., conditions where the surface morphology and the as-
 383 sociated form drag play an important role (e.g., Garbrecht et al., 2002; Lüpkes & Birn-
 384 baum, 2005; Lüpkes et al., 2012; Mchedlishvili et al., 2023). Observations for frazil and
 385 grease ice are rare and limited to low-wind and mildly-sloped wave conditions (see Guest,
 386 2021b, and references there). For frazil and grease ice, drag coefficients between $0.7 \cdot 10^{-3}$

387 and $1.3 \cdot 10^{-3}$ have been reported. No formula relating wind speed to surface drag, anal-
 388 ogous to (6) and valid for frazil/grease sea ice has been proposed so far. In polynyas, the
 389 sea surface in ice-covered areas is characterized by the presence of long waves (with length
 390 and amplitude similar to those in the surrounding open water) and absence of high-frequency
 391 waves (Fig. 1). It is an open question how these unique surface properties – very smooth
 392 at length scales of centimeters to meters, undulating at length scales of tens of meters
 393 – modify the bulk drag coefficient. Aware of uncertainties behind this assumption, we
 394 select the middle value from the range reported above ($1 \cdot 10^{-3}$), increase it by 5% to ac-
 395 count for stability effects analogous to those in open water (Fig. 3a), and arrive at the
 396 value $C_{Di} = 1.05 \cdot 10^{-3}$ for ice-covered parts of the polynyas.

397 With these C_{Dw} and C_{Di} , the ratio u_*/c can be computed for a range of (f, u_{10})
 398 combinations over open water and ice (Fig. 3b,d). When the wind speed is low and the
 399 waves are long (MIZ-typical conditions), u_*/c is small and, consequently, in equation (5),
 400 the second term in square brackets is larger than the first one (regions to the left of the
 401 dashed magenta lines in Fig. 3b,d). Thus, β_{in} is approximately linearly proportional to
 402 u_*/c and its values are very low (they equal zero to the left of the dashed white lines in
 403 Fig. 3b,d). Conversely, for short waves and high wind speeds, β_{in} is large and propor-
 404 tional to $(u_*/c)^2$. Crucially, over both ice and open water, most of the combinations of
 405 f and u_{10} relevant for polynyas lie in the strongly-forced regime (dotted rectangles in
 406 Fig. 3b,d). For wind speeds between, say, 20 and 35 $\text{m} \cdot \text{s}^{-1}$, the ratio $\beta_{in,i}/\beta_{in,w}$ decreases
 407 slowly with f (it approaches C_{Di}/C_{Dw} as $f \rightarrow \infty$), but it remains fairly constant for
 408 wave frequencies $f > 0.2$ Hz (Fig. 3c). It drops rapidly to very low values as f drops
 409 below 0.2 Hz, but for those long waves β_{in} itself is very small (dashed lines in Fig. 3c)
 410 – if these waves grow, its due to nonlinear wave–wave interactions and not due to direct
 411 energy input from the wind. Therefore, for the sake of simplicity, we set a_{in} in (1) to a
 412 constant value, equal to the mean $\beta_{in,i}/\beta_{in,w}$ over frequency range $f \in [0.13, 0.6]$ Hz at
 413 wind speed $u_{10} = 25 \text{ m} \cdot \text{s}^{-1}$ (a typical value for our set of TNBP events). Thus, $a_{in} =$
 414 0.56 in all our simulations, as marked with the black line in Fig. 3c.

415 By drawing an analogy to oil slicks once again, we notice that the observed ratios
 416 of u_* over slicks to that over open water are close to 0.8 (e.g., Alpers & Hühnerfuss, 1989),
 417 leading to the ratios $\beta_{in,i}/\beta_{in,w}$ of 0.66–0.67, higher than but comparable to our estimate.

418 3.2.3 S_{ice}

419 Finally, for the ice dissipation term S_{ice} in (1), an empirical expression used in both
 420 SWAN and WaveWatchIII wave models (Collins & Rogers, 2017; Rogers, 2019) has the
 421 form of a sum:

$$422 \quad S_{ice} = \alpha_{ice} E = \sum_{n=0}^{n_m} \alpha_{ice,n} f^n E, \quad (7)$$

423 where $\alpha_{ice,n}$ for $n = 1, \dots, n_m$ are coefficients that can be tuned to a particular situ-
 424 ation or set to values from one of the published studies (see, e.g., Rogers, Meylan, & Ko-
 425 hout, 2018; Rogers, Posey, et al., 2018, for an overview of available formulae). The de-
 426 fault settings in SWAN are from Meylan et al. (2014), with $\alpha_{ice,2} = 1.06 \cdot 10^{-3} \text{ s}^2 \text{ m}^{-1}$,
 427 $\alpha_{ice,4} = 2.3 \cdot 10^{-2} \text{ s}^4 \text{ m}^{-1}$ and the remaining $\alpha_{ice,n}$ equal to zero. With this set of coef-
 428 ficients, the energy attenuation in ice gradually changes slope from f^2 for long waves to
 429 f^4 in the tail of the spectrum. Several subsequent studies use this form of S_{ice} with re-
 430 tuned $\alpha_{ice,2}$ and $\alpha_{ice,4}$ (e.g., Rogers, Meylan, & Kohout, 2018; Rogers et al., 2021). Gen-
 431 erally, their values in frazil and grease ice are even a few times lower than in pancakes
 432 and ice floes. Some observations provide evidence for f^5 or f^6 in the spectral tail (Rogers
 433 et al., 2021, and references there), leading to a different combination of zero and non-
 zero coefficients in (7).

434 Notably, S_{ice} in (7), being purely empirical, does not differentiate between various
 435 physical energy dissipation mechanisms that are relevant in different ice types. The change

of slope of $\alpha_{\text{ice}}(f)$ from low to high wave frequency, described above, is often attributed to different (combinations of) physical attenuation mechanisms dominating in the long-wave and short-wave parts of the spectrum. In frazil and grease ice analyzed here, however, it seems reasonable to assume that viscous dissipation is the only relevant process and that, at least within the relatively narrow frequency range carrying most energy, a single exponent n can be used for all f .

Additional formulations of S_{ice} with dependence on ice thickness have been proposed and are implemented in SWAN. They are not considered here. As this study concentrates on the active-frazil parts of polynyas, i.e., before the ice consolidates into a relatively compact ice cover, no significant effects of ice thickness are expected. Analogously, we do not consider here a source term describing wave scattering in sea ice, as this process is not relevant in frazil and grease ice.

3.3 Model setup and simulations

The simulations in this analysis are performed with SWAN version 41.45 (<http://www.swan.tudelft.nl>). In accordance with the assumptions formulated in section 3.1, several simplifications are made in the model setup. A rectangular model domain with 200 m spatial resolution is used, with realistic coastlines, but a constant water depth of 500 m. For each polynya, two sea ice maps have been prepared, one with ice concentration within the polynya $A = 0$ (for reference, open-water model runs; see below), and one with ice concentration obtained by averaging the values of A determined in Bradtko and Herman (2023) within each 200×200 m² grid cell of the model. In both cases, the ice pack surrounding the polynya has ice concentration $A = 1$. The model is run in a stationary mode and forced with wind fields from AMPS (section 2). No currents are taken into account. In spectral space, directional resolution of 10° and 52 frequency bins logarithmically spaced between 0.05 and 1.576 Hz are used. Thus, the maximum frequency is close to six times the highest expected peak frequency (~ 0.25 Hz), and the frequency increment factor equals 1.07, as recommended for simulations with the near-exact quadruplet wave-wave interaction algorithm (SWAN Team, 2022).

In the simulations, several combinations of a_{in} , and α_{ice} are considered, as listed in Table 2. Setup S0, with $a_{\text{in}} = 1$ and $\alpha_{\text{ice}} = 0$ provides a reference, open-water test case. In setup S1, wind input over sea ice is turned off ($a_{\text{in}} = 0$) and this is the only effect ice has on waves ($S_{\text{ice}} = 0$). In setup group S2, $a_{\text{in}} = 0.56$, as determined in section 3.2. S2_0 is analogous to S1. In S2_f24 (M14) the default SWAN settings for S_{ice} are used, based on Meylan et al. (2014). In the remaining four setups the sea ice source term is fitted to observations by running the model several times with different combinations of coefficients and selecting the version that results in the best agreement between satellite-derived and simulated peak wave periods. Among many possible criteria of ‘the best’ agreement, the mean bias has been selected, as this is the main deficiency of setup S0 that we aim at removing. Thus, the optimization is stopped when the relative bias, defined as the average ratio $(T_{p,\text{obs}} - T_{p,\text{mod}})/T_{p,\text{obs}}$, does not exceed 1% (Table 2). The resulting $\alpha_{\text{ice}}(f)$ are shown in Fig. 4.

Obviously, many more combinations of non-zero $\alpha_{\text{ice},n}$ than those considered here could be tested, including those that are predicted by various theoretical models of viscous and viscoelastic dissipation in sea ice (Meylan et al., 2018). However, as we have no means to extract quantitative information on spectral tails from the available satellite imagery, insight gained from additional simulations would be rather limited. As we demonstrate in the next section, setups S2_f4, S2_f5 and S2_f6 are sufficient to illustrate the sensitivity of the model to ice-related dissipation at high wave frequencies and to formulate some important conclusions regarding frequency dependence of S_{ice} in polynyas.

Table 2. Summary of SWAN simulations: sea-ice related model parameters and model performance

Setup ID	Model parameters		Statistics of T_p			
	a_{in}	$\alpha_{ice,n}$	c.c.	bias	rel. bias	s.d.d.
S0	1	0 for all n	0.87	1.15 s	0.19	0.49 s
S1	0	0 for all n	0.80	-0.06 s	-0.01	0.39 s
S2_0	0.56	0 for all n	0.85	0.66 s	0.11	0.42 s
S2_f24 (M14)	0.56	$\alpha_{ice,2} = 1.06 \cdot 10^{-3}, \alpha_{ice,4} = 0.230 \cdot 10^{-1}$	0.84	0.34 s	0.06	0.40 s
S2_f24 (fitted)	0.56	$\alpha_{ice,2} = 0.53 \cdot 10^{-3}, \alpha_{ice,4} = 1.035 \cdot 10^{-1}$	0.80	-0.02 s	-0.003	0.43 s
S2_f4 (fitted)	0.56	$\alpha_{ice,4} = 1.2 \cdot 10^{-1}$	0.87	0.07 s	0.01	0.37 s
S2_f5 (fitted)	0.56	$\alpha_{ice,5} = 0.66$	0.86	0.04 s	0.01	0.40 s
S2_f6 (fitted)	0.56	$\alpha_{ice,6} = 3.2$	0.83	0.05 s	0.01	0.45 s

c.c. – correlation coefficient, s.d.d. – standard deviation of differences

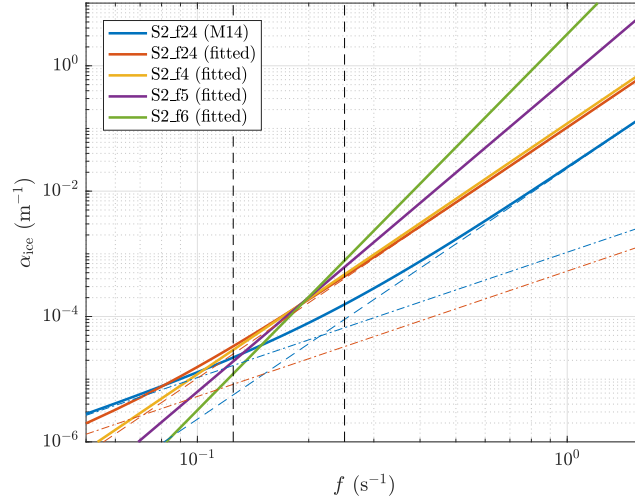


Figure 4. The five $\alpha_{ice}(f)$ curves considered in model version S2. Blue and red thin dashed lines show the components of the two versions of S2_f24 (M14 and fitted), and the black vertical lines mark the range of wave frequencies corresponding to the observed peak periods.

4 Results

In the following, we first compare the performance of the tested model setups (Table 2) in terms of their ability to reproduce the observed patterns of peak periods T_p in all ten polynya events. Subsequently, we perform a detailed analysis of the satellite observations and modelling results for the polynya from 19. Sep. 2019. It is selected for this purpose for two reasons. First, due to its very large size, it covers the whole range of observed wave periods in the analyzed dataset. Second, it is the only image for which the (nearly) simultaneous wave breaking patterns could be obtained from the WV2 image, as described in section 2.2. The whitecap fraction W and energy dissipation S_{wc} within the WV2 scene and over the whole polynya are discussed in section 4.3. Finally, in section 4.4, we return to the whole dataset of 10 polynyas and analyze global (polynya-surface averaged) statistics of individual source terms.

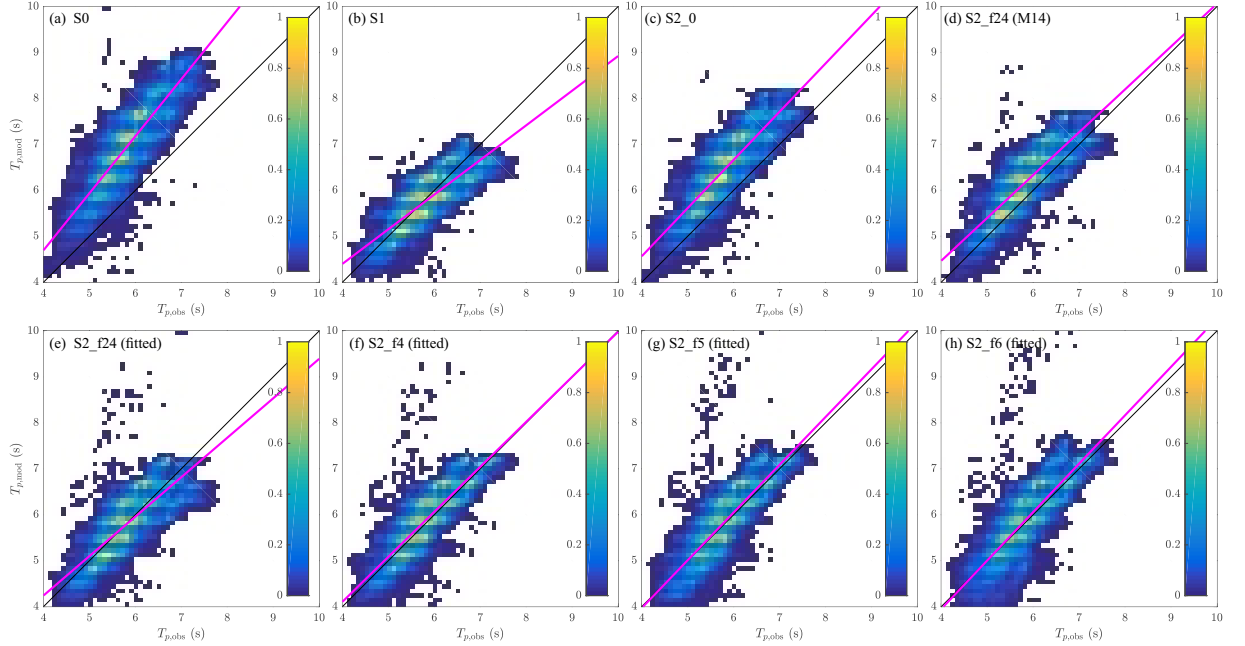


Figure 5. Scatterplots of observed and modelled peak periods, $T_{p,obs}$ and $T_{p,mod}$, from the simulations listed in Table 2. The color scale shows values in percent of the total number of data points (i.e., all values in each plot sum up to 100), and magenta lines show the linear regression to the data.

497

4.1 Performance of the tested model setups

498

499

500

501

For the purpose of model–observations comparison, the satellite-derived maps of T_p from the 10 polynyas are averaged within the meshes of the SWAN grid, resulting in a dataset of over $2.3 \cdot 10^5$ values. The observed peak periods have values between 4 and 8 s, with the mean and median equal to 5.87 s and 5.81 s, respectively.

502

503

504

505

506

507

508

509

510

511

As expected from the results of a simple one-dimensional (1D) model in Bradtke and Herman (2023), setup S0 significantly overestimates the wave periods – on average by 1.15 s or close to 20% (Table 2 and Fig. 5a). This effect occurs in spite of the well documented tendency of SWAN and other spectral models to underestimate wave periods (see, e.g., Rogers et al., 2003). Moreover, the AMPS wind speeds used as model input generally tend to be slightly lower than the wind speeds measured at the Manuela station, i.e., if there is a bias in the model forcing, it is towards too weak rather than too strong winds. Thus, as already concluded in Bradtke and Herman (2023), sea ice is the only likely factor responsible for the discrepancy between the observed wave periods and those expected in open water.

512

513

514

515

516

517

518

519

520

521

Not surprisingly, the bias is reduced in setup S1, with $a_{in} = 0$, even though no energy dissipation in sea ice is assumed. In fact, the mean bias in S1 is close to zero, and the standard deviation of differences is reduced relative to S0. However, these improvements are achieved at the cost of lowered correlation coefficients; moreover, the model clearly underestimates the large wave periods (Fig. 5b), i.e., the wave growth is inhibited in downwind parts of polynyas with high ice concentration. Obviously, the assumption behind S1 that the influence of frazil streaks is strong enough to completely shut down the wind input, but at the same time that the ice has no direct influence on waves through dissipation, seems unrealistic. However, adding to S1 any $\alpha_{ice} > 0$ would lead to an even worse model performance and to a negative bias. Hence, the lack of wind in-

522 put over ice-covered areas is an unlikely explanation for the observations and, accord-
 523 ingly, ‘deactivation’ of S_{in} over ice is not a good choice.

524 As can be seen in Table 2, setting a_{in} to 0.56 as in S2.0 reduces approximately half
 525 of the mean bias of S0 (Fig. 5c), with a still further reduction in setup S2_f24 (M14), i.e.,
 526 when the default S_{ice} SWAN setting is used (Fig. 5d). The performance can be improved
 527 further by fitting $\alpha_{\text{ice},2}$ and $\alpha_{\text{ice},4}$. However, the fitted value of $\alpha_{\text{ice},2}$ is twice as low as
 528 in the corresponding setup with M14, and $\alpha_{\text{ice},4}$ is over four times higher, meaning that
 529 the fitted α_{ice} is dominated by the f^4 term: the change of slope towards f^2 takes place
 530 at frequencies well below 0.1 Hz, i.e., outside of the range of wave frequencies found in
 531 our dataset (compare blue and red curves in Fig. 4). Indeed, dropping the $\alpha_{\text{ice},2}$ term
 532 as in S2_f4 results in the fitted value of $\alpha_{\text{ice},4}$ very close to that in S2_f24 (Table 2). More-
 533 over, although setup S2_f4 has only one fitted coefficient as opposed to two in S2_f24, it
 534 gives the best global statistics not only in terms of the mean bias, but also the correla-
 535 tion coefficient and standard deviation of differences – and it performs well in the whole
 536 range of the observed values of T_p (Fig. 5f). Therefore, the simpler version S2_f4 is pre-
 537 ferred over S2_f24.

538 Finally, the last two tested setups are S2_f5 and S2_f6, which, as expected, leads
 539 to a stronger (weaker) attenuation of the lowest (highest) wave periods (Fig. 5f–h). With
 540 increasing power n the scatter gets slightly higher and the correlation coefficient lower
 541 (Table 2), but, arguably, the differences between the global statistical measures of set-
 542 ups S2_f4, S2_f5 and S2_f6 are rather subtle. This is not surprising as the analysis so
 543 far is limited to the peak periods, i.e., the frequency range in which the strength of dis-
 544 sipation in S2_f4, S2_f5 and S2_f6 is very similar (Fig. 4). The differences between these
 545 setups can be expected to be more substantial in the tails of the wave energy spectra.
 546 Unfortunately, as stated earlier, we cannot perform any quantitative comparison between
 547 the observed and modelled spectral tails. However, as we will see in the next section, large
 548 qualitative differences between the results of S2_f4, S2_f5 and S2_f6 allow for some (care-
 549 ful) conclusions.

550 4.2 The polynya from 19. Sep. 2019

551 The polynya from 19. Sep. 2019 (Fig. 1) is the largest among the ten polynyas anal-
 552 ysed here (see S_p in Table 1). At the time the analysed satellite image was acquired, the
 553 area had been subject to prolonged strong WNW winds with speeds exceeding $20 \text{ m}\cdot\text{s}^{-1}$
 554 for ~ 36 hours, and exceeding $30 \text{ m}\cdot\text{s}^{-1}$ for close to 24 hours (not shown). As the polynya
 555 has a relatively regular, symmetric shape, it is useful to examine the wind forcing, and
 556 the observed and simulated wave properties on a transect along its central axis (white
 557 dashed line in Fig. 1; corresponding maps can be found in Supplementary Figs. S2 and
 558 S3). At 21 UTC the AMPS wind (Fig. 6a) along that line oscillates between 30 and $35 \text{ m}\cdot\text{s}^{-1}$
 559 up to a distance x of ~ 50 km from shore, and drops to 25 – $30 \text{ m}\cdot\text{s}^{-1}$ only within the last
 560 ~ 10 km of the polynya. It also gradually changes direction from WNW to WSW, but
 561 this change is not fast, in the order of 10° per 30 km. In terms of ice concentration (Fig. 6b),
 562 two clearly different regions can be distinguished: for x below and above 40 km. In the
 563 first region, the ice concentration varies strongly as the analyzed profile crosses sea-ice
 564 and open-water patches, but on average it remains rather low (mean value 0.41). In the
 565 second region, it rarely drops below one (mean value 0.98).

566 As can be seen in Fig. 6c, the no-ice setup of SWAN (S0) significantly overpredicts
 567 the peak wave period (by almost 2 s, i.e., close to 30%, in the offshore part of the polynya).
 568 It also predicts significant wave heights H_s exceeding 5 m (see Supplementary Fig. S3
 569 for corresponding maps of T_p and H_s). The three ‘best’ setups identified in section 4.1,
 570 S2_f4–S2_f6, produce almost indistinguishable $T_p(x)$ and $H_s(x)$ curves. In agreement with
 571 observations, T_p at the downwind end of the polynya exceeds 7 s (corresponding to peak
 572 wavelengths of 75–80 m). Notably, H_s reaches maximum at the end of the varying-ice-

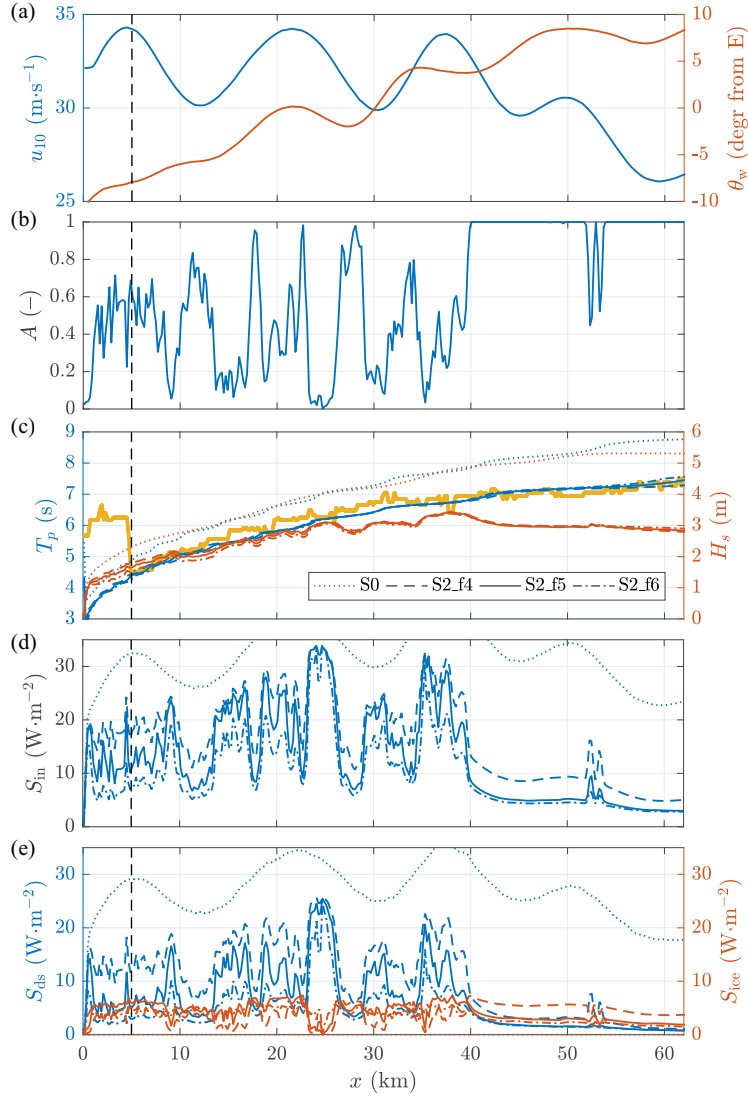


Figure 6. Wind speed u_{10} and direction θ_w (a), ice concentration A (b), significant wave height H_s and peak period T_p (c), wind input S_{in} (d), and dissipation due to wave breaking S_{ds} and in sea ice S_{ice} (e) along the central line of the polynya from 19. Sep. 2019 (see Fig. 1 for transect location). In (c)–(e), the modelling results are shown for four model setups: S0 (dotted lines), S2_f4 (dashed lines), S2_f5 (continuous lines) and S2_f6 (dash-dotted lines); thick yellow line in (c) shows the observed T_p . The black vertical dashed lines at $x = 5$ km mark the boundary of the nearshore region where no reliable wave properties could be determined from the satellite data.

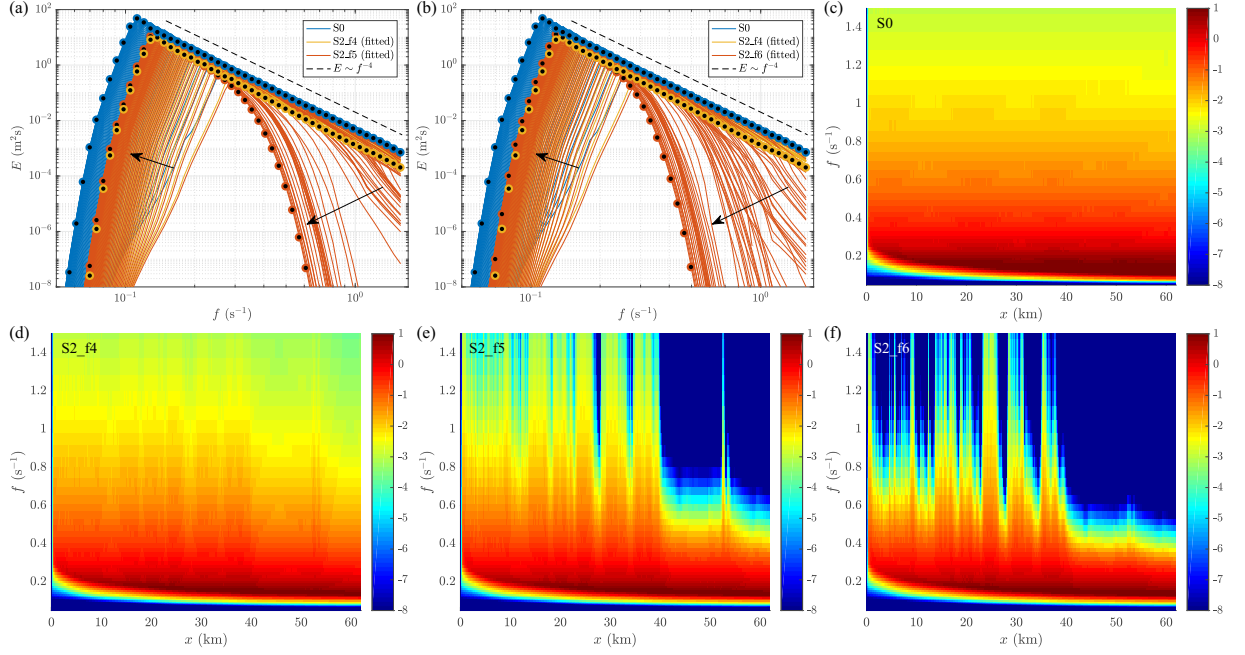


Figure 7. Wave energy spectra $\bar{E}(f)$ along the central line of the polynya from 19. Sep. 2019 (see Fig. 1 for transect location) from four model setups: S0, S2_f4, S2_f5 and S2_f6. In (a,b), every 5th spectrum along the transect is drawn for each setup (S0, S2_f4 and S2_f5 in a, S0, S2_f4 and S2_f6 in b); black arrows mark the direction of increasing x , and the dashed black line has the slope f^{-4} . In (c)–(f), colors show $\log_{10} \bar{E}$ ($\text{n m}^2\text{s}$) for S0 (c), S2_f4 (d), S2_f5 (e) and S2_f6 (f).

573 concentration zone, close to $x = 40$ km, and then stays roughly constant at ~ 3 m, in-
 574 dicated an approximate balance between wind input and dissipation.

575 In spite of very similar evolution of the spectral peaks, however, the results of the
 576 three setups differ substantially from each other for frequencies above ~ 0.4 Hz (Fig. 7).
 577 In S2_f4, the tails of the spectra remain very close those in the open-water case S0, even
 578 at the downwind end of the polynya. That is, $E \sim f^{-4}$ in the tail (Fig. 7a). In open
 579 water it is a signature of the balance between wind input and whitecapping dissipation
 580 (red and yellow curves in Fig. 8a–e; see also Fig. 6d,e). Indeed, in S2_f4 \tilde{S}_{in} and S_{ds} dom-
 581 inate in the spectral tail wherever the ice concentration is relatively low (Fig. 8h). At
 582 higher A , \tilde{S}_{ice} is comparable to S_{ds} (Fig. 8f,g) or even higher (Fig. 8i,j), but the frequency
 583 dependence of both source terms is the same – in terms of their mathematical form they
 584 are interchangeable. In S2_f5 and S2_f6, to the contrary, ice-induced dissipation of the
 585 high-frequency waves is strong enough so that they are almost entirely removed from the
 586 spectra as soon as the ice concentration exceeds ~ 0.5 . This produces spectral shapes sim-
 587 ilar to those observed in the MIZ (compare brown curves in Fig. 5a,b with, e.g., Fig. 6
 588 of Rogers et al. (2016) or Fig. 2 of Montiel et al. (2022)). As the waves propagate through
 589 the patches of grease ice and open water in the central parts of the polynya, the short
 590 waves in the spectral tail disappear and reappear as in Fig. 7e,f – an aspect of the re-
 591 sults that qualitatively agrees with what is seen in the WV2 image (Figs. 1 and 2).

592 The consequences of very strong dissipation of short waves in S2_f5 and, especially,
 593 S2_f6 are clearly seen in the plots of source terms in Fig. 8k–u. As the wave energy at
 594 frequencies higher than ~ 0.4 Hz is zero or close to zero in ice-covered locations, the wind
 595 input there is close to zero as well – as are all other source terms. Remarkably, in these

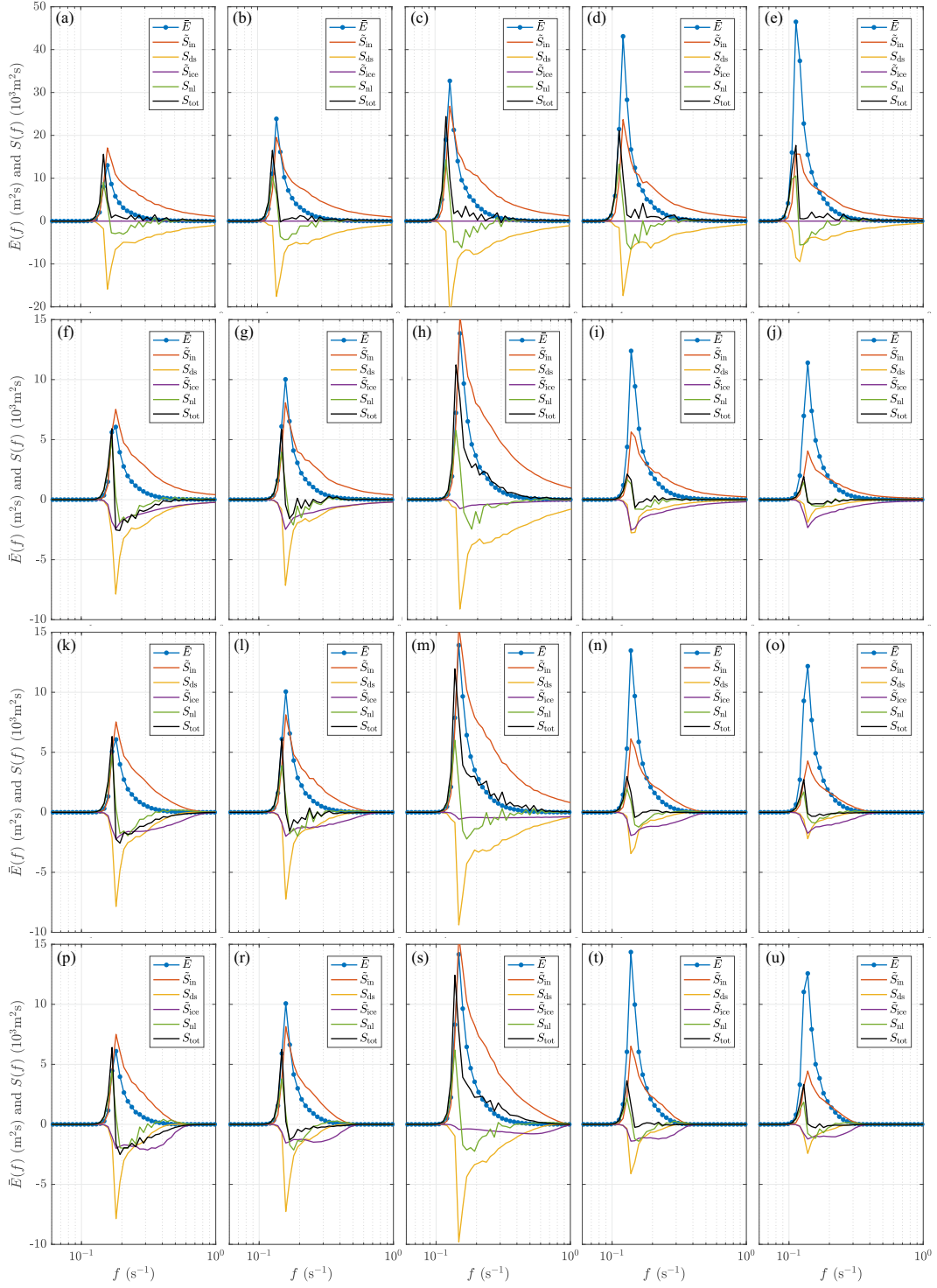


Figure 8. One-dimensional wave energy spectra $\bar{E}(f)$ and source terms at 5 locations along the central line of polynya from 19. Sep. 2019 (white dots in Fig. 1a), from model setups S0 (a–e), S2_f4 (f–j), S2_f5 (k–o) and S2_f6 (p–u). For wind input and sea ice source terms, $\tilde{S}_{in} = [1 - A + a_{in}A]S_{in}$ and $\tilde{S}_{ice} = AS_{ice}$ are shown (see equation 1). The black lines show S_{tot} , the sum of all source terms. Note different y -axis scales in (a–e) and (f–u). The ice concentration A at points 1–5 equals 0.72, 0.85, 0.29, 1.00 and 1.00, respectively.

596 areas the dissipation in sea ice is particularly strong in the range 0.2–0.4 Hz, i.e., just
 597 below the no-energy range. If the ice concentration is not too high (Fig. 8k,l,p,r), this
 598 energy sink is strengthened by whitecapping, leading to a negative overall energy bal-
 599 ance in spite of energy input from wind and, to a lesser extent, from quadruplets. At ice
 600 concentration close to 1 (Fig. 8n,o,t,u), the role of whitecapping and quadruplets becomes
 601 less significant, and the first-order energy balance is between wind input and ice dissi-
 602 pation. As a net effect, the energy spectra evolve towards narrow, swell-like shapes (see
 603 maps of directional spreading in Supplementary Fig. S3).

604 4.3 Wave breaking

605 The total surface area of breaking waves estimated from the WV2 data covers 1.08%
 606 of the whole area of the analyzed image. Their spatial distribution is inversely correlated
 607 with sea ice concentration (Fig. 9a). Considering the whole area of the WV2 image, the
 608 contribution of breaking waves to the open-water surface is 1.5%, more than twice as much
 609 as in the ice-covered areas, where it is 0.6%. Locally, however, this difference depends
 610 on the spatial pattern of frazil streaks – which can be seen when the two subsets of the
 611 WV2 area are analyzed separately (Fig. 10).

612 Over much of the lower part of the WV2 image (subset 2), the average ice concen-
 613 tration calculated in vertical sections is relatively low and remains between 0.2 and 0.4
 614 with no visible spatial trend (Fig.10). This subset shows narrow streaks of frazil ice that
 615 only begin to increase in width and merge near the center of the image and gradually
 616 form a more compact ice cover. Under these conditions, the average whitecap fraction
 617 W_X changes similarly in open water and in ice, with W_X reaching a maximum at the
 618 distance of about 14–16 km from the ice sheet. In this area, the difference between W_X
 619 in water and ice remains roughly constant. Only when the average ice concentration in-
 620 creases to about 0.5, at the distance of 21.5 km from shore, a rapid decrease of W_X in
 621 streaks and a corresponding increase in open water is observed, producing an order-of-
 622 magnitude difference between the W_X in open-water and ice-covered areas.

623 In the upper part of the image (subset 1), the variability of whitecap fraction in
 624 open water are similar (Fig. 10), with a maximum at an approximately the same distance
 625 from shore. However, the difference between W_X in open water and ice in subset 1 is gen-
 626 erally larger than in subset 2, which can be at least partly explained by the presence of
 627 the very wide and long (width ~ 500 m) ‘mega-streak’ – a dominating feature in subset 1.
 628 As can be seen in Fig. 9a, it contains almost no whitecaps, contributing to reduced W_X
 629 values.

630 The satellite-based wave breaking patterns cannot be directly compared with mod-
 631 elling results, because spectral wave models do not produce whitecap fraction as output.
 632 Therefore, a relationship between W and energy dissipation rate S_{wc} is necessary. To
 633 this end, we use formulae derived by Anguelova and Hwang (2016). Assuming that the
 634 water is deep, we have:

$$W = c_W \omega_p^4 S_{wc}, \quad (8)$$

635 where $\omega_p = 2\pi/T_p$ denotes the peak wave frequency and the coefficient c_W is a com-
 636 bination of several empirical constants: $c_W = t_b [4b\rho_w g^3 \log(c_{\max}/c_{\min})\alpha_c^4]^{-1}$. Their val-
 637 ues vary strongly between different field and laboratory experiments. Here, without any
 638 tuning, we adopt the values from Anguelova and Hwang (2016) for three out of the four
 639 coefficients: the bubble persistence time $t_b = 2$ s, the breaking strength parameter $b =$
 640 0.013, and the ratio of maximum to minimum breaker speed $c_{\max}/c_{\min} = 10$. The fourth
 641 one, $\alpha_c \in (0, 1)$, denotes the ratio of the threshold breaker speed to the peak wave phase
 642 speed. In Anguelova and Hwang (2016), $\alpha_c = 0.3$ is used based on the average from
 643 experiments analyzed in Gemmrich et al. (2008). Here, we instead use the modal value
 644 of the α_c distribution from the case in Gemmrich et al. (2008) with the highest u_*/c ra-
 645 tio, as it represents a situation closest to the one analyzed here. Thus, we set $\alpha_c = 0.35$.

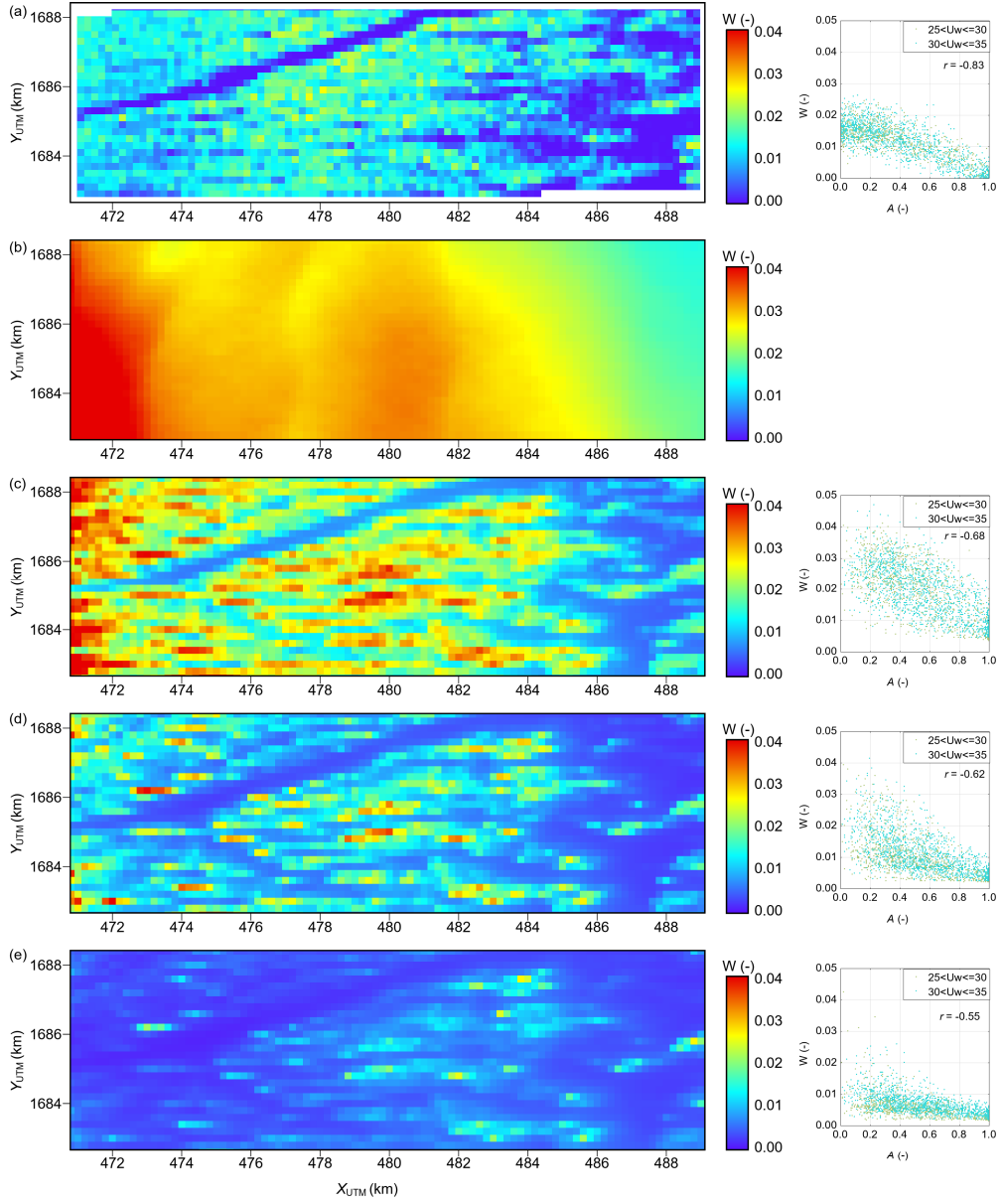


Figure 9. Observed and modelled wave breaking patterns in the area covered by the WV2 image (orange rectangle in Fig. 1). The left panels show maps of whitecap fraction W from the WV2 image (a) and from SWAN simulations with model setup S0 (b), S2_f4 (c), S2_f5 (d) and S2_f6 (e). Right panels show scatterplots of W against ice concentration A for wind speeds below and above $30 \text{ m}\cdot\text{s}^{-1}$ (green and blue dots).

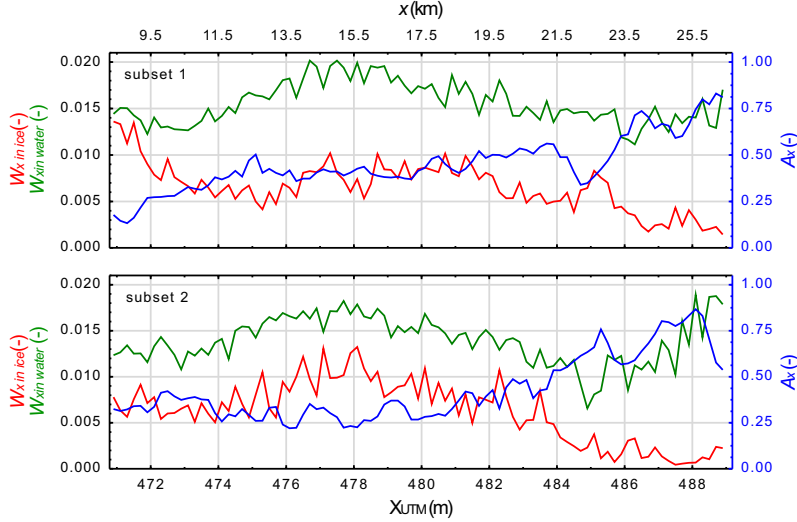


Figure 10. Average ice concentration A_X (right axes) and whitecap fraction W_X computed separately over ice-covered and ice-free regions (left axes) of subsets 1 and 2 of the analyzed WV2 image. X_{UTM} and x denote the UTM coordinates and the distance from the ice sheet, respectively.

646 The resulting maps of W in the WV2 region from model setups S0, S2_f4, S2_f5
 647 and S2_f6 are shown in Fig. 9b–e. Not surprisingly, the results of the no-ice setup S0 are
 648 completely different from satellite observations. However, the remaining three setups pro-
 649 duce spatial patterns which are very similar to the observed one – and, at a general level,
 650 very similar to each other (this is also true for the whole polynya; see Supplementary Figs.
 651 S4 and S5). The best agreement is obtained for S2_f5, which also produces very simi-
 652 lar range of values, generally with $W < 0.03$. In S2_f6, wave breaking is very weak, mostly
 653 with $W < 0.01$ and with only isolated hotspots of whitecap fractions reaching 0.02. In
 654 S2_f4, to the contrary, values exceeding 0.03 are not rare, especially in the leftmost part
 655 of the region (a feature absent in satellite-derived data).

656 It is noteworthy that that the spatial patterns of W and S_{ds} are markedly differ-
 657 ent (Supplementary Fig. S5) due to the strong wave-frequency dependence of W in equa-
 658 tion (8). For the same whitecap fraction W , energy dissipation is lower in long waves
 659 than in short waves, and *vice versa*, the same energy dissipation is associated with higher
 660 values of W when the waves are shorter. This is responsible for the clearly fetch
 661 dependence of W in our simulations: the largest values of W can be found nearshore (in
 662 all model versions, including S0), when they exceed 0.1. In the case of S_{ds} , it is predom-
 663 inantly influenced by wind speed u_{10} and ice concentration A (Supplementary Figs. S6
 664 and S7). Indeed, as Supplementary Fig. S7 shows for the example of setup S2_f5, $S_{ds}(u_{10}, A)$
 665 can be easily fit to the data, with the dependence on wind speed being $S_{ds} \sim u_{10}^{2.88}$, which
 666 is very close to the relationship $S_{ds} \sim u_{10}^3$ reported in the literature (Anguelova & Hwang,
 667 2016).

668 4.4 Global source terms statistics

669 Although the differences between setups S2_f4–S2_f6 manifest themselves mainly
 670 in the tails of the spectra, their effects are clearly visible in spectrally integrated source
 671 terms as well (see Fig. 6d,e and maps in Supplementary Fig. S4). The overall spatial pat-
 672 terns remain similar, as they are dictated by the variability of ice concentration, but the
 673 amplitude of all source terms varies strongly between setups. Consequently, the total (polynya-

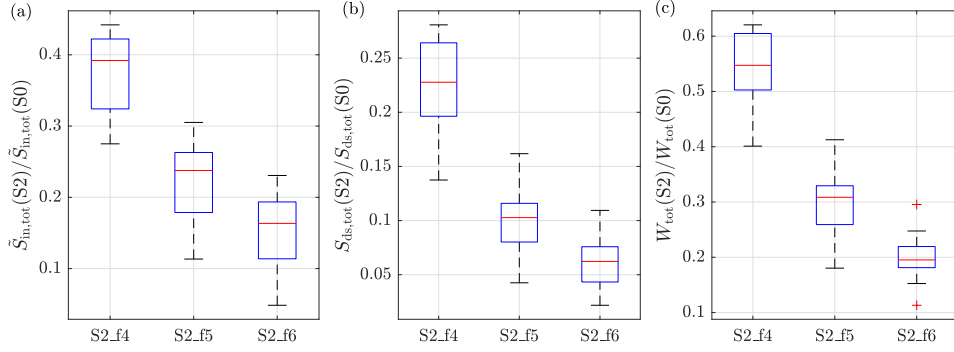


Figure 11. Box plots showing statistics of the ratios $\tilde{S}_{\text{in,tot}}(\text{S2})/\tilde{S}_{\text{in,tot}}(\text{S0})$ (a), $S_{\text{ds,tot}}(\text{S2})/S_{\text{ds,tot}}(\text{S0})$ (b) and $W_{\text{tot}}(\text{S2})/W_{\text{tot}}(\text{S0})$ (c) for the three model versions S2_f4, S2_f5 and S2_f6 and for the ten polynyas analyzed. Red lines show the median values and blue boxes mark the interquartile range.

674 integrated) energy input from wind, $\tilde{S}_{\text{in,tot}}$, as well as dissipation within sea ice $\tilde{S}_{\text{ice,tot}}$
 675 and due to whitecapping $S_{\text{ds,tot}}$ (with the associated W_{tot}), exhibit very large differences
 676 between the ice-free and ice-influenced model versions, hinting at the crucial role of sea
 677 ice in modifying polynyas' ocean–atmosphere interactions.

678 The box plots in Fig. 11 show statistics of the ratios of those global variables in
 679 ice-influenced and ice-free model runs, for the ten polynyas analyzed. Although some vari-
 680 ability between the ten cases is present, the results are fairly robust (notably, there is
 681 no significant correlation between the analyzed ratios and polynya size). Considering that,
 682 based on the analysis so far, model settings S2_f5 and S2_f6 best describe available ob-
 683 servations, it is save to conclude that the polynya-wide wind input is typically reduced
 684 to below 25% of that over open water, the energy dissipation due to whitecapping is re-
 685 duced to below 10%, and the corresponding coverage of sea surface by whitecaps is re-
 686 duced to below 30%. These (conservative) estimates decrease with increasing exponent
 687 n in the S_{ice} source term. Consequences of the lowered wind input and whitecapping are
 688 briefly discussed in the next section.

689 5 Discussion and conclusions

690 This study has shown that wind waves in coastal polynyas with frazil streaks are
 691 significantly modified by sea ice – and that the role of ice is much more complex than
 692 simply dissipating wave energy through viscous processes in a spectral-component-by-
 693 component manner. Rather, the net effect of sea ice is a combined result of dissipation,
 694 reduced wind input, reduced whitecapping, and modified nonlinear energy transfer within
 695 energy spectra. The ‘patchiness’ of the grease ice cover, typical of polynyas, and the as-
 696 sociated alternating removal and re-generation of short waves in the tail of the spectrum
 697 play here a particular role. Regarding the four relevant source terms in the wave energy
 698 balance equation, the main conclusions of this study are:

- 699 • Contrary to the common ‘binary’ treatment of S_{in} in waves-in-ice modelling (e.g.,
 700 Li et al., 2015; Cheng et al., 2017; Rogers et al., 2016, 2021), wind input over grease
 701 ice is neither equal to that over open water ($a_{\text{in}} = 1$) nor zero ($a_{\text{in}} = 0$). Un-
 702 der conditions of strongly forced waves analyzed here, a constant value of the wind
 703 reduction factor $a_{\text{in}} = 0.56$ has been determined based on theoretical arguments
 704 and led to a satisfactory model performance. However, as detailed in section 3.2,
 705 a_{in} is in fact a function of wind speed and wave frequency. Using a simple param-

eterization with constant α_{in} seems reasonable considering very limited observational data on wave growth in ice covered waters, but the analysis in this study provides a general framework for more complex formulations in the future, applicable over a wider range of wave ages and frequencies. Regarding the largely unknown variability of the surface drag coefficient C_{Dn} over grease ice in presence of waves, a promising direction of further research might be analogous to parameterizations of surface drag used in modelling of oil spills, in which the net roughness length is computed as a weighted sum of three components, associated with an aerodynamically smooth surface, long waves and short waves, respectively, and the weight of the last component is different over oil and water, reflecting very strong attenuation of short waves in oil-covered regions (Bourassa et al., 1999; Zheng et al., 2013; Blair et al., 2023).

- Whitecapping is strongly reduced in regions where frazil streaks are present – not only within streaks themselves, but also in open-water areas between them – confirming existing qualitative observations from TNBP (Guest, 2021a, 2021b; Ackley et al., 2022). Crucially, in the model this effect is obtained without any modifications to the formulation of the S_{ds} term. Rather, reduced whitecapping is a consequence of reduced wave steepness, which in turn results from reduced wind input and from dissipation in sea ice. This does not mean, however, that the open-water formulations of S_{ds} used in the present spectral wave models are fully adequate for grease ice regions. It seems likely that the critical steepness used to compute S_{wc} in equation (3) is slightly higher in water covered with grease ice than in open water. Moreover, at the same sea surface area fraction covered with breakers in open water and in grease ice, the amount of dissipated wave energy might be different due to suppressed turbulence and air bubble formation in the latter case.
- As long as the developing ice cover is thin and the open-water dispersion relation holds, the quadruplet wave–wave interactions remain unaffected and can be computed in the same way as in open water. However, in combination with strong ice-related dissipation in the high-frequency part of the spectrum, their role in regions covered with frazil streaks becomes particularly important. In our simulations, there were substantial differences between the results obtained with DIA and with the quasi-exact method. When using DIA, the very strong positive bias of the wave periods could not be reduced by any reasonable combination of adjustable coefficients. With the quasi-exact method, the bias was much smaller and the model calibration unproblematic. Obviously, considering the fact that the computational costs of computing quadruplets in an exact way are over 10^3 times higher than those of DIA, our finding cannot be treated as a recommendation for waves-in-ice modelling, especially in operational or climate applications. However, one should be aware of biases and uncertainties associated with the usage of DIA, and of the danger related to the interpretation of the results of DIA-based models, in which S_{ice} and possibly other source terms must compensate DIA-related biases.
- We did not find any evidence of the change of slope n of the sea ice source term with wave frequency. The most straightforward interpretation is that a single physical mechanism is responsible for energy dissipation in the analyzed case, with viscous or viscoelastic dissipation the most likely candidates. Crucially, although with the observational data at our disposal we were not able to determine the value of n , we show that $n > 4$ is necessary for a sufficiently strong attenuation in the tail of the spectrum, i.e., for preventing the slope in the tail from reaching the $E \sim f^{-4}$ shape, typical for open water. Very importantly, this finding does not contradict observations of $n < 4$ in earlier studies (Meylan et al., 2018, and references there), where it refers to the apparent attenuation from pairs of measured spectra.
- Considering the previous conclusion together with the comparison between the satellite-derived and modelled wave breaking patterns, $n = 5$ seems to produce the best

761 results – but this should be treated as an indication rather than a firm conclusion
 762 (and, obviously, n does not have to be a natural number).

- 763 • On average, the presence of frazil and grease ice in the analyzed polynyas leads
 764 to a reduction of the total wind input to less than 25% of that over open water,
 765 and to the reduction of whitecapping dissipation to less than 10%, with the cor-
 766 responding reduction of the surface area fraction covered with whitecaps to be-
 767 low 30%. Exact values of those ratios depend on the value of n in the S_{ice} term
 768 and thus on the intensity of sea ice dissipation.

769 Some of the above conclusions are specific for polynya conditions. As noted sev-
 770 eral times throughout this paper, waves in the MIZ typically have lower frequency, are
 771 weakly forced by wind, and propagate through a wider variety of ice types. Neverthe-
 772 less, at several locations where wave–ice interactions have been studied, the conditions
 773 are in between those of an ‘ideal’ MIZ and of a coastal polynya. The Beaufort Sea in the
 774 summer and autumn is a good example (Rogers et al., 2016; Smith & Thomson, 2016):
 775 the wind fetch is relatively short, frequent low pressure systems are associated with high
 776 wind speeds, and a typical ice type is a thin frazil-pancake mixture. Therefore, a proper
 777 treatment of the S_{in} and, close to the ice edge, S_{ds} terms is important for reliable spec-
 778 tral modelling, and the present study provides important clues to the formulation of those
 779 terms. On the other hand, some of the assumptions made here might be unsuitable for
 780 the MIZ. The contribution of nonbreaking-waves dissipation S_{nbr} to the total S_{ds} is just
 781 one example – it is negligible in a coastal polynya, where whitecapping dominates over
 782 other dissipation mechanisms ($f_{br} \simeq 1$ in equation (2)), but the opposite might be true
 783 for the MIZ, where the waves do not break, but turbulent dissipation in the under-ice
 784 boundary layer (Voermans et al., 2019; Herman, 2021) dominates the S_{ds} term.

785 Our study provides also a very good example of limitations for model development
 786 caused by the lack of sufficient observational data. Performing wave-in-ice measurements
 787 in the MIZ is very challenging. In coastal polynyas, it is even more difficult due to, first,
 788 extreme weather conditions (very high wind speeds, very low air temperatures), and sec-
 789 ond, short wavelengths, requiring higher spatial (in the case of satellite and airborne im-
 790 agery) and temporal (in the case of wave buoys and other in situ sensors) resolution. In
 791 the TNBP and other coastal polynyas, peak wavelengths only rarely exceed 80–90 m and
 792 are lower than that over most of the polynya area. Thus, the usage of many popular syn-
 793 thetic aperture radar (SAR) data sources to retrieve wave energy spectra (e.g., Stopa,
 794 Ardhuin, et al., 2018; Wadhams et al., 2018) becomes problematic, as their resolution
 795 is comparable with wavelength. Even if peak wavelengths can be determined with suf-
 796 ficient accuracy, estimation of the spectral tails is unreliable. This study has shown that,
 797 although spatial variability of peak periods (and other wave properties at the spectral
 798 peak) provides a very valuable information on the underlying physics, there are limita-
 799 tions to this approach and the knowledge of spectral tails is crucial for making inferences
 800 about the frequency dependence of physical processes shaping the energy spectra. No-
 801 tably, collecting *in situ* wave data from polynyas is challenging as well, e.g., in the case
 802 of wave buoys a serious problem is contamination of measured velocities from heavy buoy
 803 tilting, heaving, as well as very fast drift (exceeding 1 m/s; Ackley et al., 2022). In gen-
 804 eral, the question facing both observations and modelling is whether and how data anal-
 805 ysis methods, (semi)empirical parameterizations etc., formulated and tested under ‘typ-
 806 ical’ conditions, can be transferred to the extreme conditions of polynyas without vio-
 807 lating their underlying assumptions. In particular, in the case of spectral wave modelling,
 808 it is an open issue how expressions (4)–(6) can be made more adequate for polynya events.
 809 A related challenge is reconciling information from observations and models. In this study,
 810 we obtained two different measures of wave breaking in the analyzed area – one in the
 811 form of whitecap fraction W (from a visible satellite image), and one in the form of en-
 812 ergy dissipated per unit surface area S_{wc} (from a spectral wave model). The $W(S_{wc})$ for-
 813 mula from Anguelova and Hwang (2016) with default coefficients happens to produce
 814 model-based values of W very close to those determined from satellite data. However,

815 this and similar relationships suffer from the same problems as the ones mentioned above:
816 the wind speeds in this study are outside the range of observations used to formulate them.

817 Finally, it is worth commenting on the consequences of the significantly reduced
818 wind input and whitecapping dissipation due to the presence of sea ice in polynyas. One
819 of them are lower rates of sea spray production (due to both lower whitecap fractions
820 W and, likely, less intense bubble and spray generation in breaking waves when grease
821 ice is present), which has been shown to contribute large part of the total ocean–atmosphere
822 turbulent heat flux at high wind speeds. Thus, suppressed whitecapping should lead to
823 significantly lower ocean mixed layer heat loss and, consequently, lower sea ice produc-
824 tion rates.

825 Data Availability Statement

826 The code of SWAN model is freely available at <http://www.swan.tudelft.nl>. In-
827 put files necessary to reproduce our simulations, together with modeling results, can be
828 found at <https://zenodo.org/record/8308164> (Herman & Bradtke, 2023).

829 Acknowledgments

830 This work has been financed by Polish National Science Centre projects no. 2018/31/B/ST10/00195
831 (“Observations and modeling of sea ice interactions with the atmospheric and oceanic
832 boundary layers”) and 2022/47/B/ST10/01129 (“Sea ice, waves and turbulence – from
833 laboratory scale to improved large-scale modelling”), and by the University of Gdansk,
834 Laboratory of Physical Oceanography, DS 531-OA02-D425-23. All calculations were car-
835 ried out at the Academic Computer Centre (TASK) in Gdańsk, Poland.

836 References

- 837 Ackley, S., Smith, M., Guest, P., Herman, A., & Shen, H. (2022). Winds, waves and
838 ice formation in a coastal polynya. In *Proc. 26th iahr international symposium*
839 *on ice*. IAHR. (Montréal, Canada, 19–23 June 2022)
- 840 Alberello, A., Bennetts, L., Onorato, M., Vichi, M., MacHutchon, K., Eayrs, C.,
841 ... Toffoli, A. (2022). Three-dimensional imaging of waves and floes in
842 the marginal ice zone during a cyclone. *Nature Comm.*, *13*, 4590. doi:
843 10.1038/s41467-022-32036-2
- 844 Alpers, W., & Hühnerfuss, H. (1989). The damping of ocean waves by surface films:
845 a new look at an old problem. *J. Geophys. Res.*, *94*, 6251–6265. doi: 10.1029/
846 JC094iC05p06251
- 847 Alves, J., & Banner, M. (2003). Performance of a saturation-based dissipation-rate
848 source term in modelling the fetch-limited evolution of wind waves. *J. Phys.*
849 *Oceanogr.*, *33*, 1274–1298. doi: 10.1175/1520-0485(2003)033<1274:POASDS>2.0
850 .CO;2
- 851 Anguelova, M., & Hwang, P. (2016). Using energy dissipation rate to obtain active
852 whitecap fraction. *J. Phys. Oceanogr.*, *46*, 461–481. doi: 10.1175/JPO-D-15
853 -0069.1
- 854 Benetazzo, A., Cavaleri, L., Ma, H., Jiang, S., Bergamasco, F., Jiang, W., ...
855 Qiao, F. (2019). Analysis of the effect of fish oil on wind waves and im-
856 plications for air–water interaction studies. *Ocean Sci.*, *15*, 725–743. doi:
857 10.5194/os-15-725-2019
- 858 Blair, D., Zheng, Y., & Bourassa, M. (2023). The effect of surface oil on ocean wind
859 stress. *Earth*, *4*, 345–364. doi: 10.3390/earth4020019
- 860 Booij, N., Ris, R., & Holthuijsen, L. (1999). A third-generation wave model for
861 coastal regions: 1. Model description and validation. *J. Geophys. Res.*, *104C*,
862 7649–7666. doi: 10.1029/98JC02622

- 863 Bourassa, M., Vincent, D., & Wood, W. (1999). A flux parameterization including
 864 the effects of capillary waves and sea state. *J. Atmos. Sci.*, *56*, 1123–1139. doi:
 865 10.1175/1520-0469(1999)056<1123:AFPITE>2.0.CO;2
- 866 Boutin, G., Lique, C., Arduin, F., Rousset, C., Talandier, C., Accensi, M., &
 867 Girard-Arduin, F. (2020). Towards a coupled model to investigate wave–sea
 868 ice interactions in the Arctic marginal ice zone. *The Cryosphere*, *14*, 709–735.
 869 doi: 10.5194/tc-14-709-2020
- 870 Bradtke, K., & Herman, A. (2023). Spatial characteristics of frazil streaks in the
 871 Terra Nova Bay polynya from high-resolution visible satellite imagery. *The*
 872 *Cryosphere*, *17*, 2073–2094. doi: 10.5194/tc-17-2073-2023
- 873 Cheng, S., Rogers, W., Thomson, J., Smith, M., Doble, M., Wadhams, P., . . . Shen,
 874 H. (2017). Calibrating a viscoelastic sea ice model for wave propagation in
 875 the Arctic fall marginal ice zone. *J. Geophys. Res.*, *122*, 8740–8793. doi:
 876 10.1002/2017JC013275
- 877 Ciappa, A., & Pietranera, L. (2013). High resolution observations of the Terra Nova
 878 Bay polynya using COSMO-SkyMed X-SAR and other satellite imagery. *J.*
 879 *Marine Systems*, *113–114*, 42–51. doi: 10.1016/j.jmarsys.2012.12.004
- 880 Collins, C., & Rogers, W. (2017). *A source term for wave attenuation by sea ice in*
 881 *WAVEWATCH III: IC4* (Tech. Rep. Nos. NRL/MR/7320–17-9726). Naval Re-
 882 search Laboratory. (25 pp.)
- 883 Collins, C., Rogers, W., & Lund, B. (2017). An investigation into the dispersion of
 884 ocean surface waves in sea ice. *Ocean Dynamics*, *67*, 263–280. doi: 10.1007/
 885 s10236-016-1021-4
- 886 Cox, C., Zhang, X., & Duda, T. (2017). Suppressing breakers with polar oil films:
 887 Using an epic sea rescue to model wave energy budgets. *Geophys. Res. Lett.*,
 888 *44*, 1414–1421. doi: 10.1002/2016GL071505
- 889 Deike, L., Berhanu, M., & Falcon, E. (2017). Experimental observation of hydroe-
 890 lastic three-wave interactions. *Phys. Rev. Fluids*, *2*, 064803. doi: 10.1103/
 891 PhysRevFluids.2.064803
- 892 Dumont, D. (2022). Marginal ice zone dynamics: history, definitions and research
 893 perspectives. *Phil. Trans. Royal Soc. A*, *380*, 20210253. doi: 10.1098/rsta.2021
 894 .0253
- 895 Eicken, H., & Lange, M. (1989). Development and properties of sea ice in the coastal
 896 regime of the Southeastern Weddell Sea. *J. Geophys. Res.*, *94*, 8193–8206. doi:
 897 10.1029/JC094iC06p08193
- 898 Garbrecht, T., Lüpkes, C., Hartmann, J., & Wolff, M. (2002). Atmospheric drag co-
 899 efficients over sea ice – validation of a parameterisation concept. *Tellus*, *54A*,
 900 205–219.
- 901 Gemmrich, J., Banner, M., & Garrett, C. (2008). Spectrally resolved energy dissipa-
 902 tion rate and momentum flux of breaking waves. *J. Phys. Oceanogr.*, *38*, 1296–
 903 1312. doi: 10.1175/2007JPO3762.1
- 904 Guest, P. (2021a). Inside katabatic winds over the Terra Nova Bay Polynya: 1.
 905 Atmospheric jet and surface conditions. *J. Geophys. Res.: Atmospheres*, *126*,
 906 e2021JD034902. doi: 10.1029/2021JD034902
- 907 Guest, P. (2021b). Inside katabatic winds over the Terra Nova Bay Polynya: 2.
 908 Dynamic and thermodynamic analyses. *J. Geophys. Res.: Atmospheres*, *126*,
 909 e2021JD034904. doi: 10.1029/2021JD034904
- 910 Hasselmann, S., Hasselmann, K., Allender, J., & Barnett, T. (1985). Compu-
 911 tations and parameterizations of the nonlinear energy transfer in a grav-
 912 ity wave spectrum. Part II: Parameterizations of the nonlinear transfer
 913 for application in wave models. *J. Phys. Oceanogr.*, *15*, 1378–1391. doi:
 914 10.1175/1520-0485(1985)015<1378:CAPOTN>2.0.CO;2
- 915 Herman, A. (2021). Spectral wave energy dissipation due to under-ice turbulence. *J.*
 916 *Phys. Oceanogr.*, *51*, 1177–1186. doi: 10.1175/JPO-D-20-0171.1
- 917 Herman, A., & Bradtke, K. (2023). *SWAN wave model simulations of the Terra*

- 918 *Nova Bay Polynya*. Data set, Zenodo. doi: 10.5281/zenodo.8308164
- 919 Herman, A., Dojczman, M., & Świszcz, K. (2020). High-resolution simulations of in-
 920 teractions between surface ocean dynamics and frazil ice. *The Cryosphere*, *14*,
 921 3707–3729. doi: 10.5194/tc-14-3707-2020
- 922 Hollands, T., & Dierking, W. (2016). Dynamics of the Terra Nova Bay Polynya:
 923 The potential of multi-sensor satellite observations. *Remote Sens. Environ.*,
 924 *187*, 30–48. doi: 10.1016/j.rse.2016.10.003
- 925 Holthuijsen, L. (2007). *Waves in oceanic and coastal waters*. Cambridge Univ. Press.
 926 (387 pp.)
- 927 Janssen, P., & Bidlot, J.-R. (2023). Wind–wave interaction for strong winds. *J.*
 928 *Phys. Oceanogr.*, *53*, 779–804. doi: 10.1175/JPO-D-21-0293.1
- 929 Janssen, P., Lionello, P., & Zambresky, L. (1989). On the interaction of wind and
 930 waves. *Phil. Trans. Royal Soc. A*, *329*, 289–301. doi: 10.1098/rsta.1989.0077
- 931 Kohout, A., Smith, M., Roach, L., Williams, G., Montiel, F., & Williams, M. (2020).
 932 Observations of exponential wave attenuation in Antarctic sea ice during the
 933 PIPERS campaign. *Ann. Glaciology*, *61*, 196–209. doi: 10.1017/aog.2020.36
- 934 Komen, G., Hasselmann, S., & Hasselmann, K. (1984). On the existence of a fully
 935 developed wind-sea spectrum. *J. Phys. Oceanogr.*, *14*, 1271–1285. doi: 10
 936 .1175/1520-0485(1984)014(1271:OTEOAF)2.0.CO;2
- 937 Li, J., Kohout, A., & Shen, H. (2015). Comparison of wave propagation through ice
 938 covers in calm and storm conditions. *Geophys. Res. Lett.*, *42*, 5935–5941. doi:
 939 10.1002/2015GL064715
- 940 Liu, Q., Rogers, W., Babanin, A., Li, J., & Guan, C. (2020). Spectral modeling of
 941 ice-induced wave decay. *J. Phys. Oceanogr.*, *50*, 1583–1604. doi: 10.1175/JPO
 942 -D-19-0187.1
- 943 Lüpkes, C., & Birnbaum, G. (2005). Surface drag in the Arctic marginal sea-ize
 944 zone: Comparison of different parameterisation concepts. *Bound. Layer Meteoro-*
 945 *rol.*, *117*, 179–211.
- 946 Lüpkes, C., Gryanik, V., Hartmann, J., & Andreas, E. (2012). A parametrization,
 947 based on sea ice morphology, of the neutral atmospheric drag coefficients for
 948 weather prediction and climate models. *J. Geophys. Res.*, *117*, D13112. doi:
 949 10.1029/2012JD017630
- 950 Mchedlishvili, A., Lüpkes, C., Petty, A., Tsamados, M., & Spreen, G. (2023).
 951 New estimates of the pan-Arctic sea ice-atmosphere neutral drag coeffi-
 952 cients from ICESat-2 elevation data. *EGUsphere, preprint*. doi: 10.5194/
 953 egusphere-2023-187
- 954 Meylan, M., Bennetts, L., & Kohout, A. (2014). In situ measurements and analy-
 955 sis of ocean waves in the Antarctic marginal ice zone. *Geophys. Res. Lett.*, *41*,
 956 5046–5051. doi: 10.1002/2014GL060809
- 957 Meylan, M., Bennetts, L., Mosig, J., Rogers, W., Doble, M., & Peter, M. (2018).
 958 Dispersion relations, power laws, and energy loss for waves in the marginal ice
 959 zone. *J. Geophys. Res.*, *123*, 3322–3335. doi: 10.1002/2018JC013776
- 960 Montiel, F., Kohout, A., & Roach, L. (2022). Physical drivers of ocean wave attenu-
 961 ation in the marginal ice zone. *J. Phys. Oceanogr.*, *52*, 889–906. doi: 10.1175/
 962 JPO-D-21-0240.1
- 963 Morales Maqueda, M., Willmott, A., & Biggs, N. (2004). Polynya dynamics: A re-
 964 view of observations and modeling. *Rev. Geophys.*, *42*, RG1004. doi: 10.1029/
 965 2002RG000116
- 966 Nakata, K., Ohshima, K., & Nihashi, S. (2021). Mapping of active frazil for Antarc-
 967 tic coastal polynyas, with an estimation of sea-ice production. *Geophys. Res.*
 968 *Lett.*, *48*, e2020GL091353. doi: 10.1029/2020GL091353
- 969 Powers, J., Manning, K., Bromwich, D., Cassano, J., & Cayette, A. (2012). A
 970 decade of Antarctic science support through AMPS. *Bull. Am. Meteorol. Soc.*,
 971 *93*(11), 1699–1712. doi: 10.1175/BAMS-D-11-00186.1
- 972 Roach, L., Bitz, C., Horvat, C., & Dean, S. (2019). Advances in modeling inter-

- actions between sea ice and ocean surface waves. *J. Advances Mod. Earth Systems*, *11*, 4167–4181. doi: 10.1029/2019MS001836
- Roach, L., Horvat, C., Dean, S., & Bitz, C. (2018). An emergent sea ice floe size distribution in a global coupled ocean–sea ice model. *J. Geophys. Res.*, *123*, 4322–4337. doi: 10.1029/2017JC013692
- Rogers, W. (2019). *Implementation of sea ice in the wave model SWAN* (Tech. Rep. Nos. NRL/MR/7322–19-9874). Naval Research Laboratory, USA. (25 pp.)
- Rogers, W., Hwang, P., & Wang, D. (2003). Investigation of wave growth and decay in the SWAN model: three regional-scale applications. *J. Phys. Oceanogr.*, *33*, 366–389. doi: 10.1175/1520-0485(2003)033<0366:IOWGAD>2.0.CO;2
- Rogers, W., Meylan, M., & Kohout, A. (2018). *Frequency distribution of dissipation of energy of ocean waves by sea ice using data from Wave Array 3 of the ONR “sea state” field experiment* (Tech. Rep. Nos. NRL/MR/7322–18-9801). Naval Research Laboratory, USA. (32 pp.)
- Rogers, W., Meylan, M., & Kohout, A. (2021). Estimates of spectral wave attenuation in Antarctic sea ice, using model/data inversion. *Cold Regions Sci. Tech.*, *182*, 103198. doi: 10.1016/j.coldregions.2020.103198
- Rogers, W., Posey, P., Li, L., & Allard, R. (2018). *Forecasting and hindcasting waves in and near the marginal ice zone: wave modeling and the ONR “sea state” field experiment* (Tech. Rep. Nos. NRL/MR/7320–18-9786). Naval Research Laboratory, USA. (183 pp.)
- Rogers, W., Thomson, J., Shen, H., Doble, M., Wadhams, P., & Cheng, S. (2016). Dissipation of wind waves by pancake and frazil ice in the autumn Beaufort Sea. *J. Geophys. Res.*, *121*, 7991–8007. doi: 10.1002/2016JC012251
- Shen, H. (2022). Wave-in-ice: theoretical bases and field observations. *Phil. Trans. Royal Soc. A*, *380*, 20210254. doi: 10.1098/rsta.2021.0254
- Smith, M., & Thomson, J. (2016). Scaling observations of surface waves in the Beaufort Sea. *Elementa*, *4*, 000097. doi: 10.12952/journal.elementa.000097
- Smith, M., & Thomson, J. (2019a). Ocean surface turbulence in newly formed marginal ice zones. *J. Geophys. Res.*, *124*, 1382–1398. doi: 10.1029/2018JC014405
- Smith, M., & Thomson, J. (2019b). Pancake sea ice kinematics and dynamics using shipboard stereo video. *Annals Glaciology*, *61*, 1–11. doi: 10.1017/aog.2019.35
- Squire, V. (2018). A fresh look at how ocean waves and sea ice interact. *Phil. Trans. R. Soc. A*, *376*, 20170342. doi: 10.1098/rsta.2017.0342
- Squire, V. (2020). Ocean wave interactions with sea ice: A reappraisal. *Annu. Rev. Fluid Mech.*, *52*, 37–60. doi: 10.1146/annurev-fluid-010719-060301
- Stopa, J., Ardhuin, F., Thomson, J., Smith, M., Kohout, A., Doble, M., & Wadhams, P. (2018). Wave attenuation through an Arctic marginal ice zone on 12 October 2015. 1. Measurement of wave spectra and ice features from Sentinel 1A. *J. Geophys. Res.*, *123*. doi: 10.1029/2018JC013791
- Stopa, J., Sutherland, P., & Ardhuin, F. (2018). Strong and highly variable push of ocean waves on Southern Ocean sea ice. *Proc. Nat. Acad. Sci.*, *115*, 5861–5865. doi: 10.1073/pnas.1802011115
- SWAN Team. (2022). *SWAN Cycle III, version 41.45, Scientific and Technical Documentation* (Tech. Rep.). Delft University of Technology, Faculty of Civil Engineering and Geosciences.
- Thompson, L., Smith, M., Thomson, J., Stammerjohn, S., Ackley, S., & Loose, B. (2020). Frazil ice growth and production during katabatic wind events in the Ross Sea, Antarctica. *The Cryosphere*, *14*, 3329–3347. doi: 10.5194/tc-14-3329-2020
- Van der Westhuijsen, A., Zijlema, M., & Battjes, J. (2007). Nonlinear saturation-based whitening dissipation in SWAN for deep and shallow water. *Coastal Engng.*, *54*, 151–170. doi: 10.1016/j.coastaleng.2006.08.006

- 1028 Van Vledder, G. P. (2006). The WRT method for the computation of non-linear
1029 four-wave interactions in discrete spectral wave models. *Coastal Engng*, *53*,
1030 223–242. doi: 10.1016/j.coastaleng.2005.10.011
- 1031 Voermans, J., Babanin, A., Thomson, J., Smith, M., & Shen, H. (2019). Wave atten-
1032 uation by sea ice turbulence. *Geophys. Res. Lett.*, *46*, 6796–6803. doi: 10.1029/
1033 2019GL082945
- 1034 Wadhams, P., Aulicino, G., Parmiggiani, F., Persson, P., & Holt, B. (2018). Pancake
1035 ice thickness mapping in the Beaufort Sea from wave dispersion observed in
1036 SAR imagery. *J. Geophys. Res.*, *123*, 2213–2237. doi: 10.1002/2017JC013003
- 1037 Yan, L. (1987). *An improved wind input source term for third generation ocean wave*
1038 *modelling* (Tech. Rep. Nos. 87–8). Royal Dutch Meteor. Inst. (20 pp.)
- 1039 Zhao, X., & Zhang, C. (2020). A theoretical model of wind-wave growth over an ice-
1040 covered sea. *Boundary Layer Meteorol.*, *178*, 1–19. doi: 10.1007/s10546-020-
1041 -00552-7
- 1042 Zheng, Y., Bourassa, M., & Hughes, P. (2013). Influence of sea surface temper-
1043 ature gradients and surface roughness changes on the motion of surface oil:
1044 a simple idealized study. *J. Applied Meteorol. Clim.*, *52*, 1561–1575. doi:
1045 10.1175/JAMC-D-12-0211.1
- 1046 Zijlema, M., van Vledder, G., & Holthuijsen, L. (2012). Bottom friction and wind
1047 drag for wave models. *Coastal Engng*, *65*, 19–26. doi: 10.1016/j.coastaleng
1048 .2012.03.002

Journal of Geophysical Research

Supporting Information for

**Fetch-limited, strongly forced wind waves in waters with frazil
and grease ice – spectral modelling and satellite observations
in an Antarctic coastal polynya**

Agnieszka Herman^{1*}, Katarzyna Bradtke²

¹ Institute of Oceanology, Polish Academy of Sciences, Sopot, Poland

² Institute of Oceanography, University of Gdansk, Gdynia, Poland

* corresponding author: agaherman@iopan.pl

Contents of this file

Figures S1 to S7

Introduction

This file contains additional figures presenting the results of satellite data analysis (Fig. S1) and spectral wave modelling (Figs. S2–S7), described in the main paper.

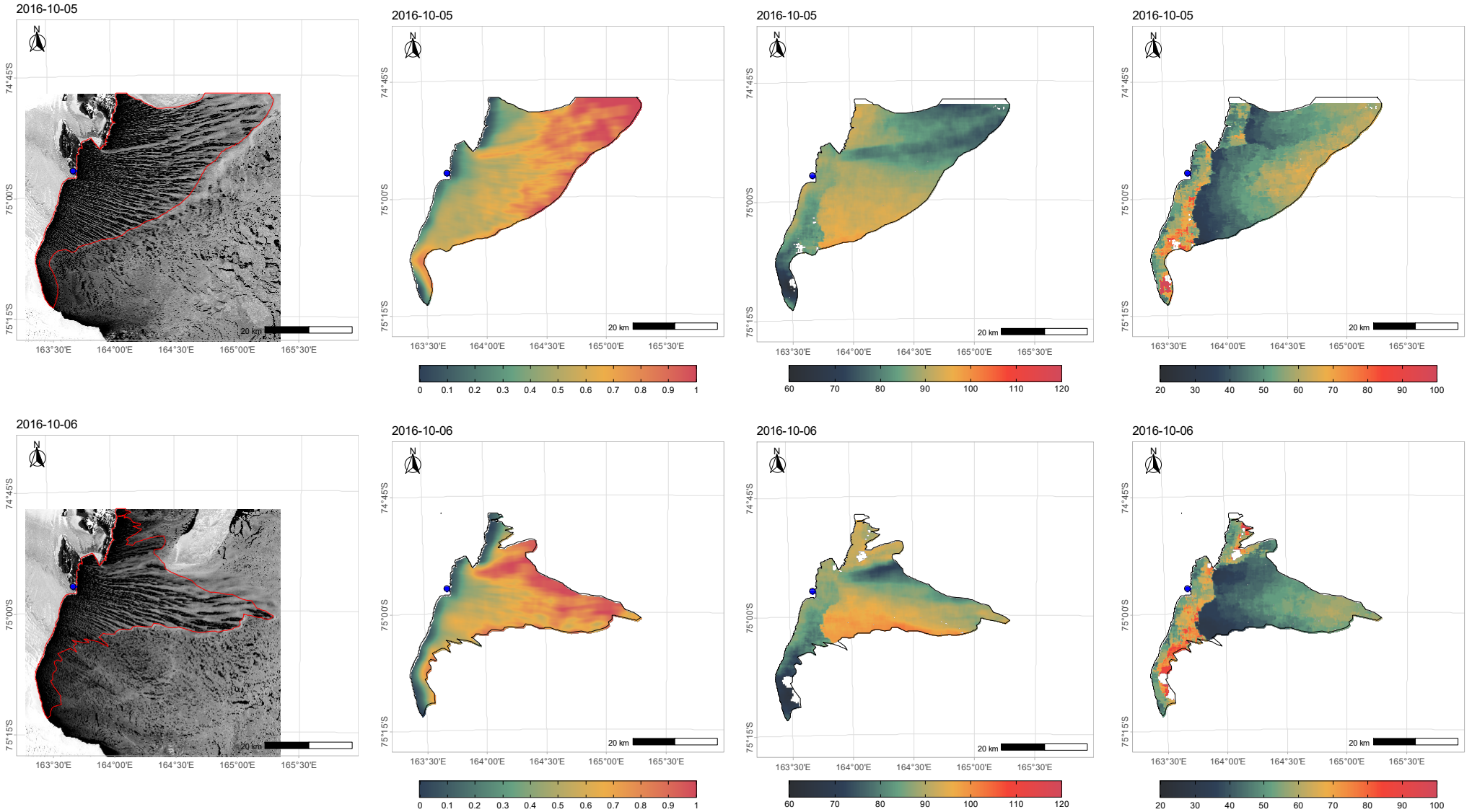


Figure S1 (continued on the following four pages): Satellite images analyzed in the study (panchromatic band reflectance; red lines mark the boundaries of regions classified as polynyas; blue dot mark the location of Manuela WS), frazil ice concentration A , mean wave direction at the peak frequency θ_p (degrees), and peak wavelength L_p (m).

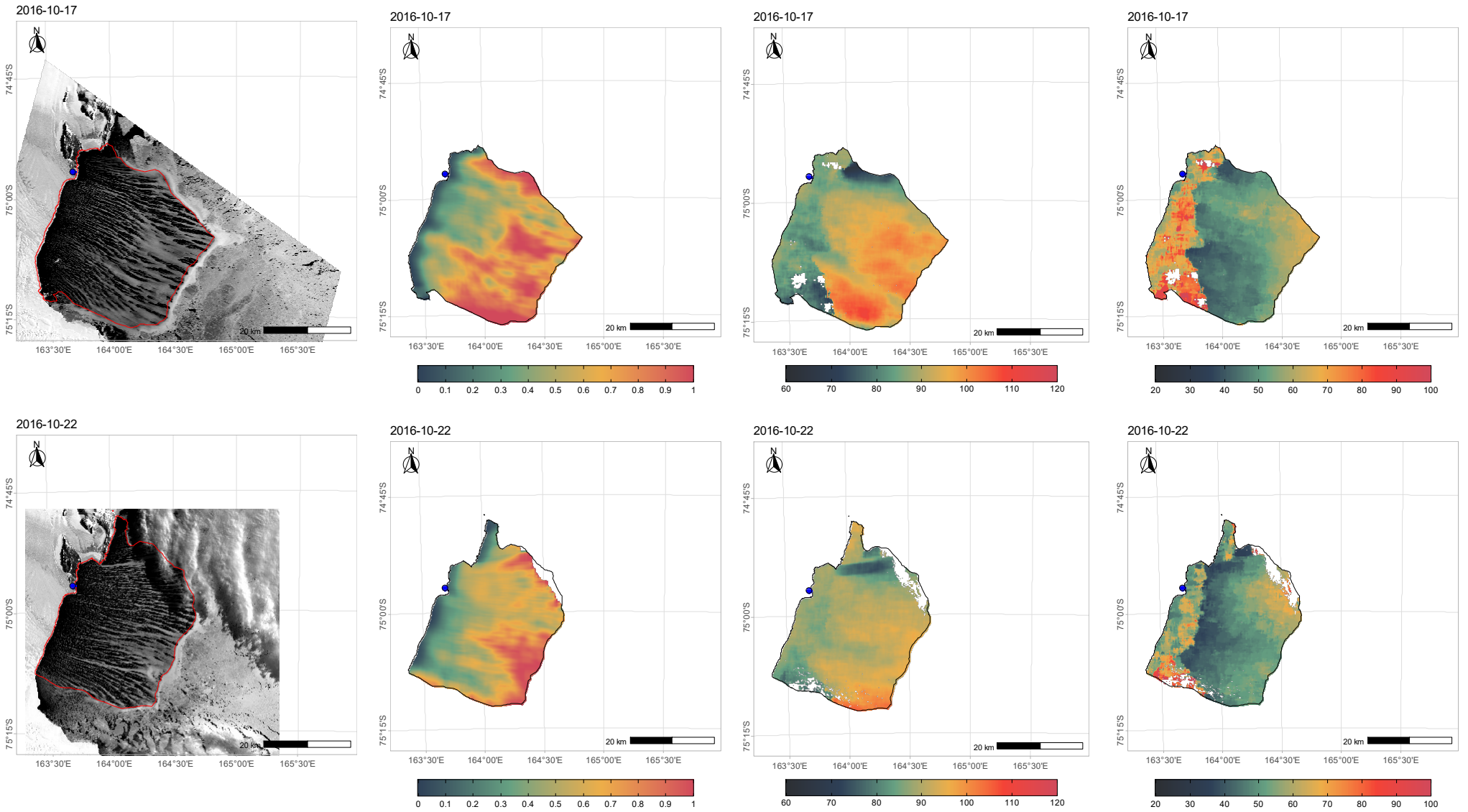


Figure S1 (continued)

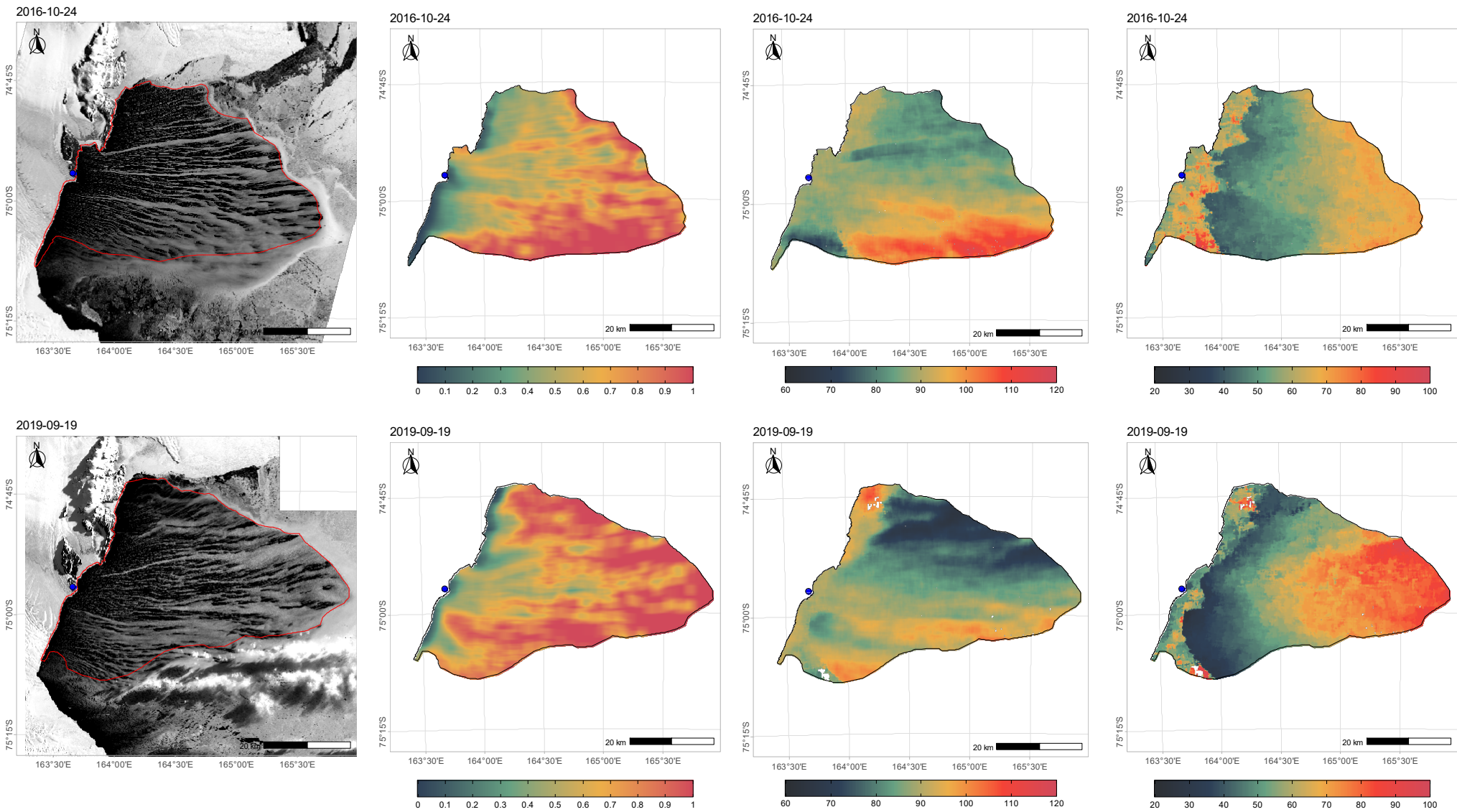


Figure S1 (continued)

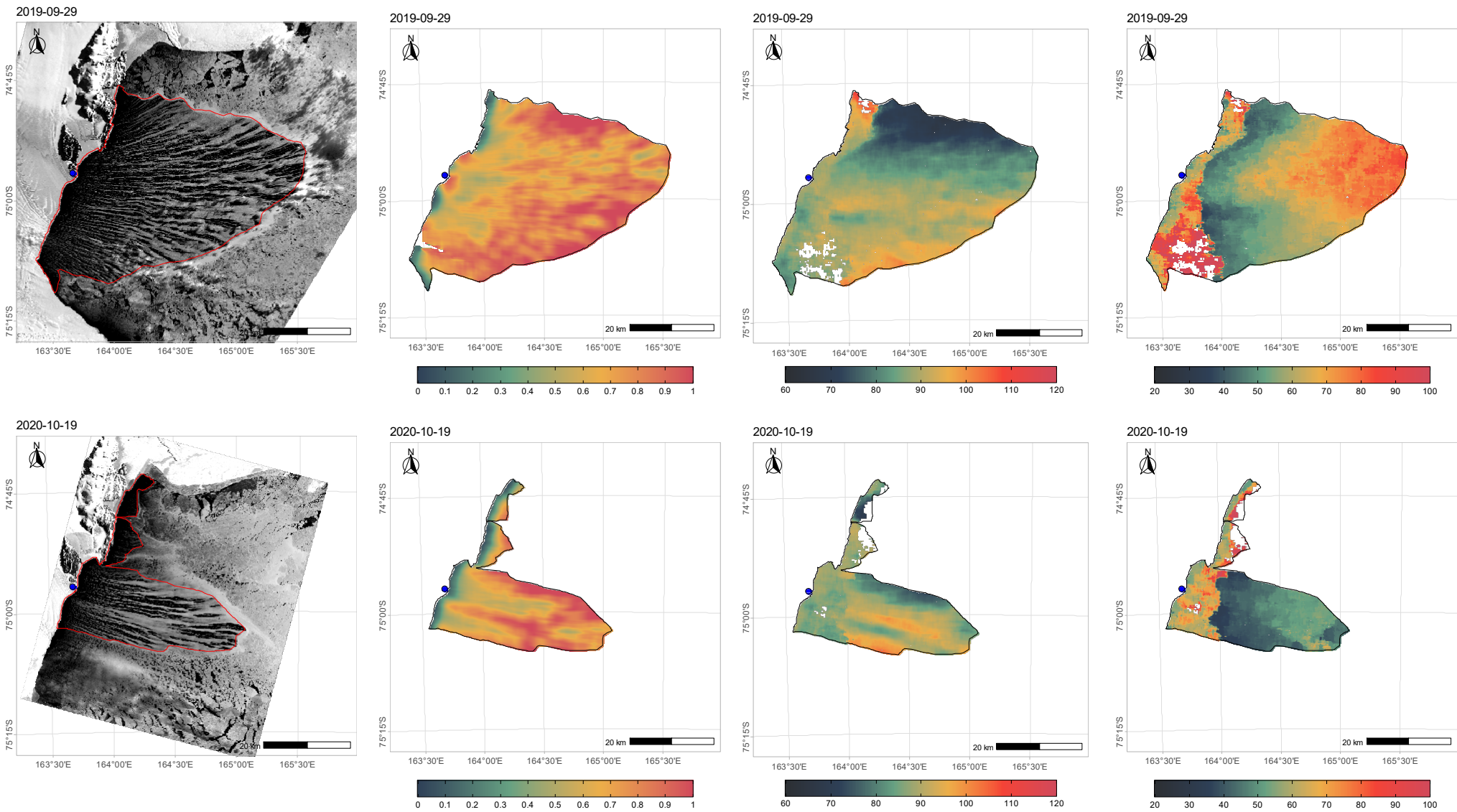


Figure S1 (continued)

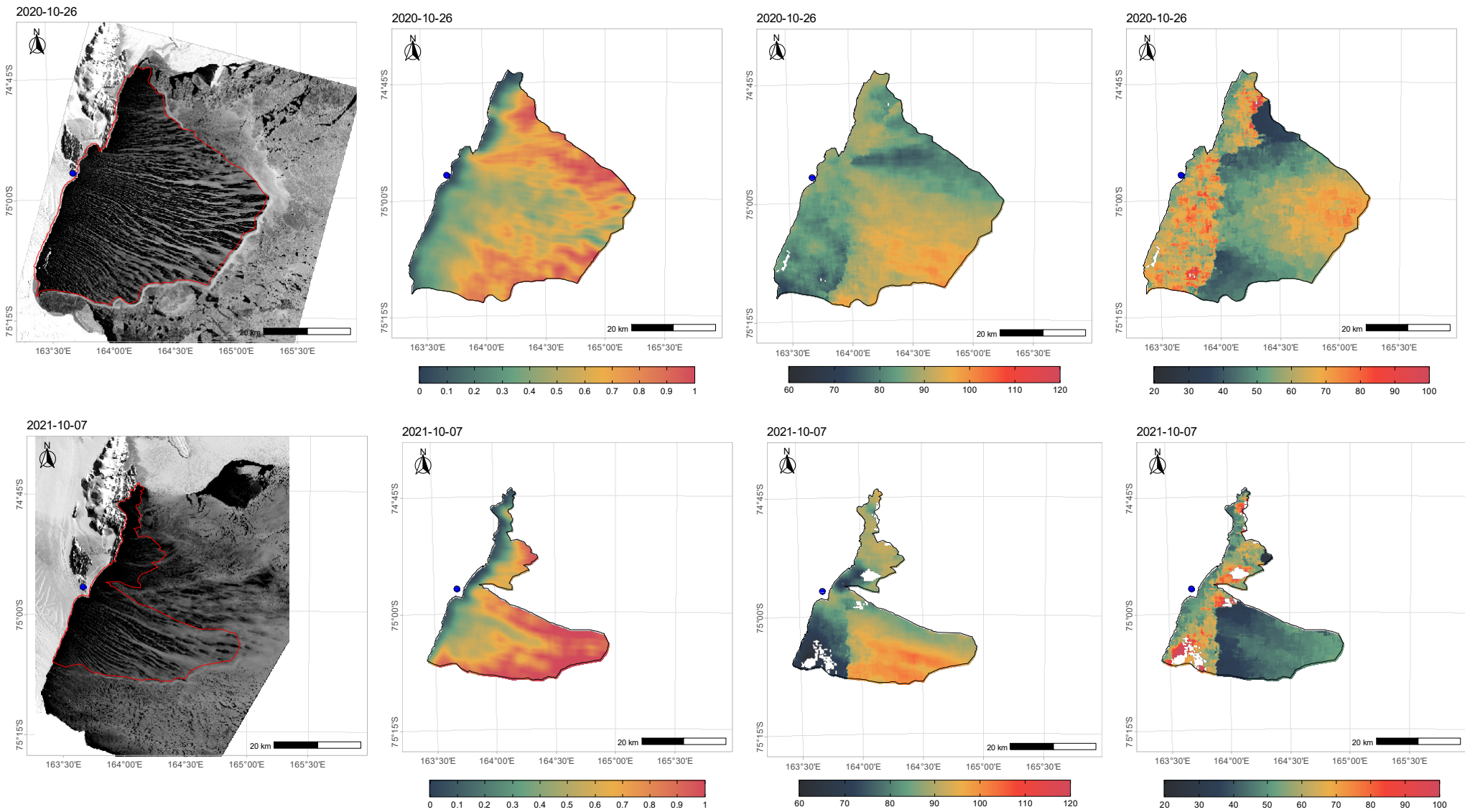


Figure S1 (continued)

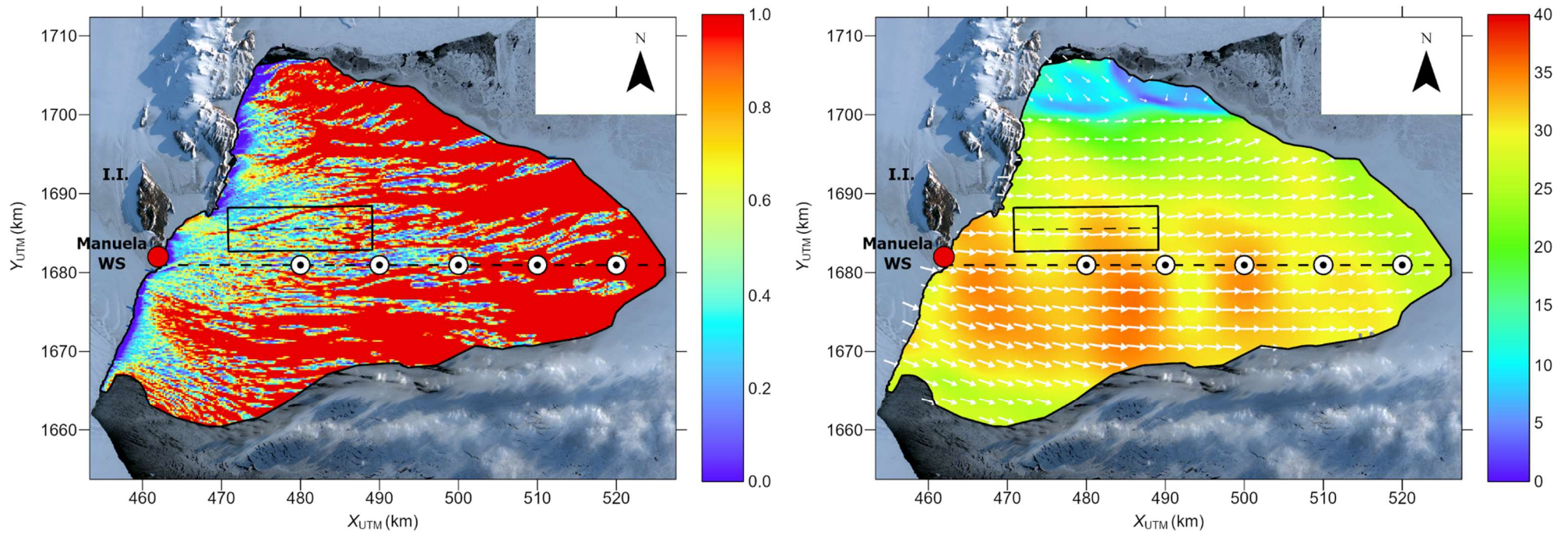


Figure S2. Maps of frazil ice concentration A and AMPS wind speed (m/s; colors) and direction (arrows) for the polynya from 19. Sep. 2019.

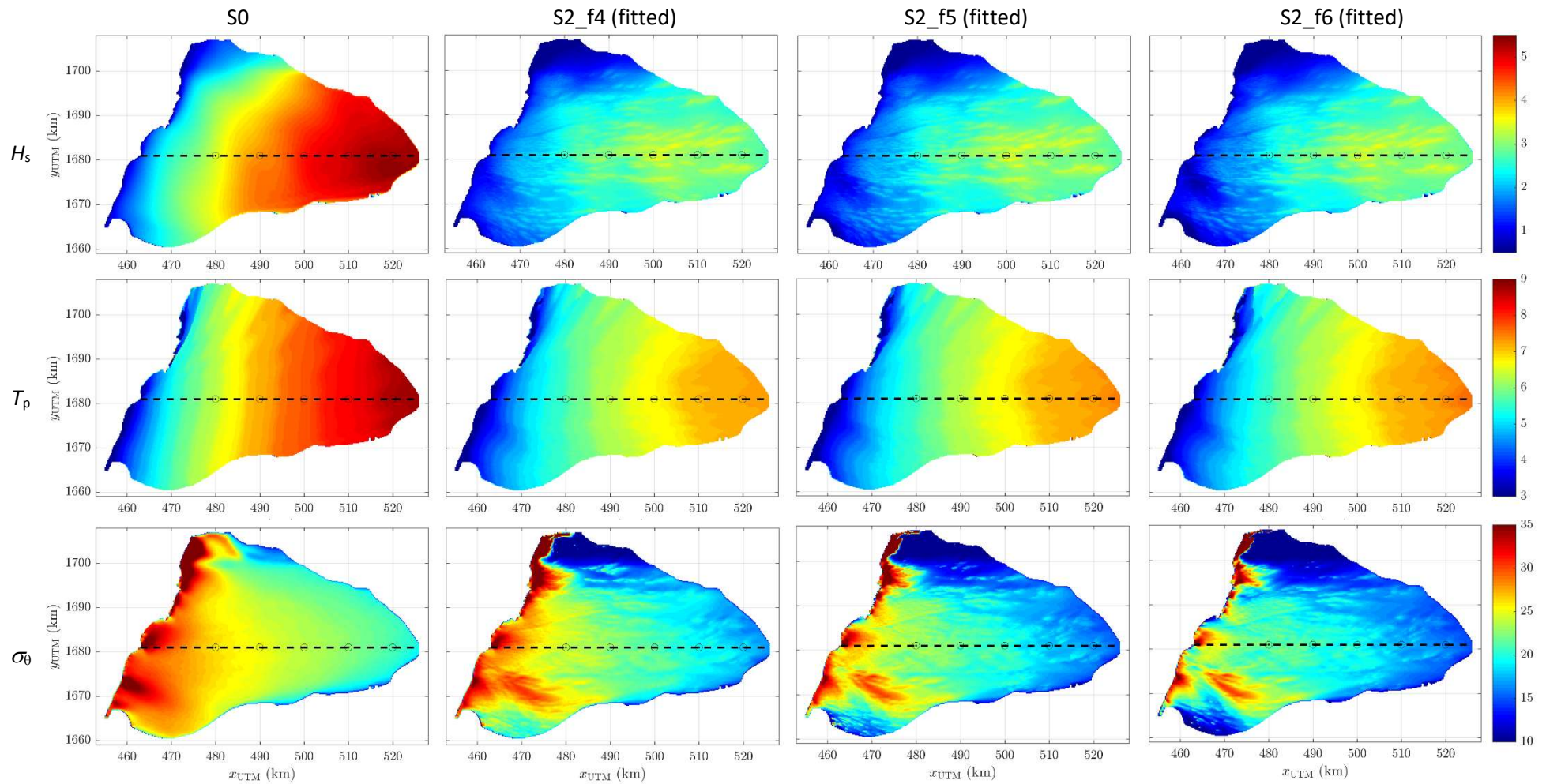


Figure S3. Maps of significant wave height H_s (m), peak wave period T_p (s) and directional spreading σ_0 (degr) for model setups S0, S2_f4 (fitted), S2_f5 (fitted) and S2_f6 (fitted). Polynya from 19.09.2019.

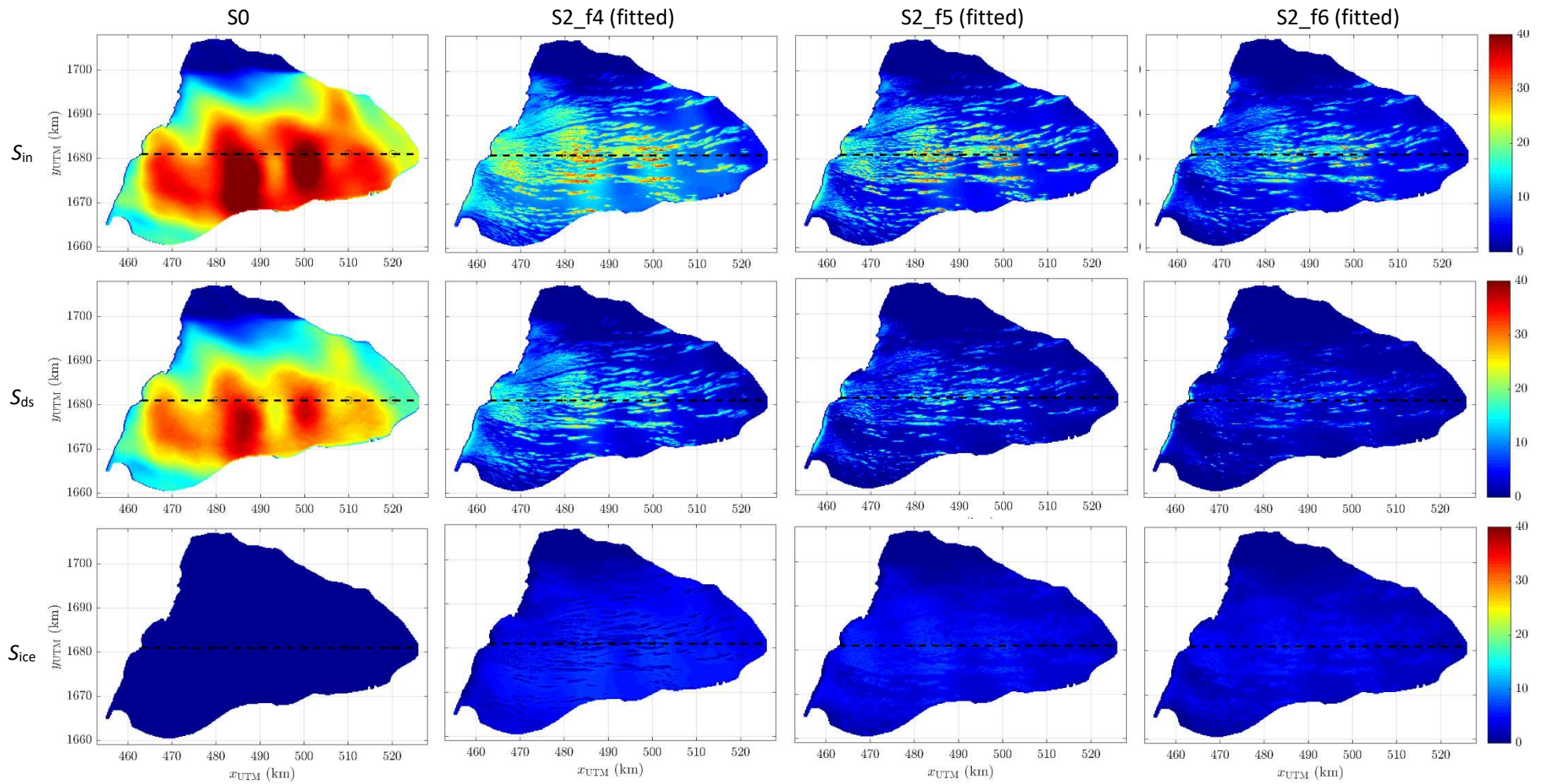


Figure S4. Maps of S_{in} , S_{ds} and S_{ice} (integrated over f and θ , in W/m^2) for model setups S0, S2_f4 (fitted), S2_f5 (fitted) and S2_f6 (fitted). Polynya from 19.09.2019.

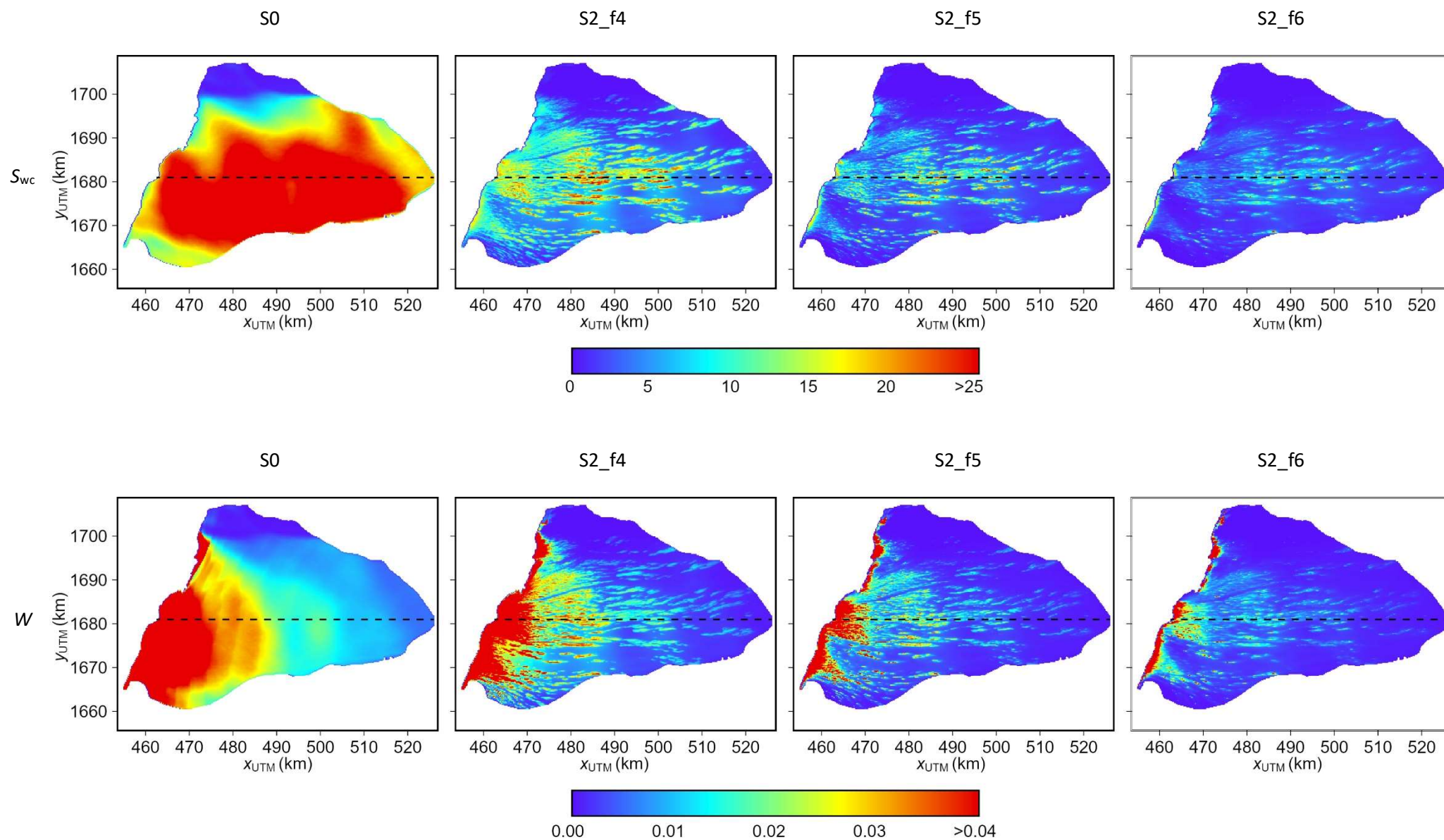


Figure S5. Maps of simulated S_{wc} (integrated over f and θ , in W/m^2) and W ($-$) for model setups S0, S2_f4 (fitted), S2_f5 (fitted), and S2_f6 (fitted). Polynya from 19. Sep. 2019.

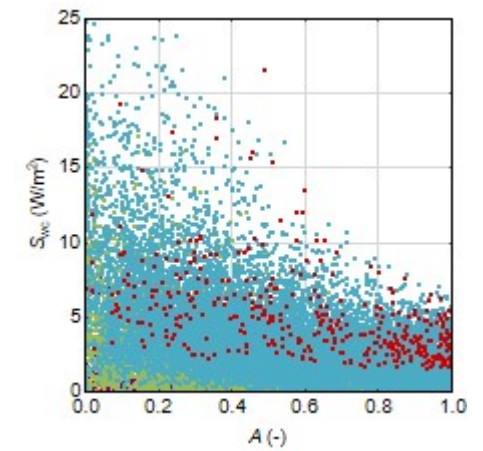
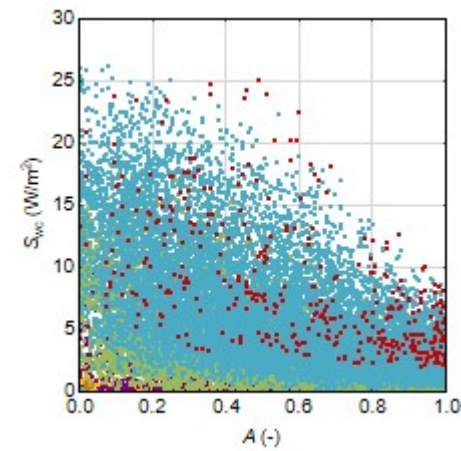
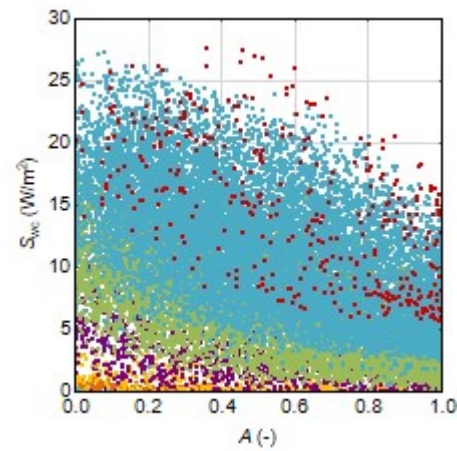
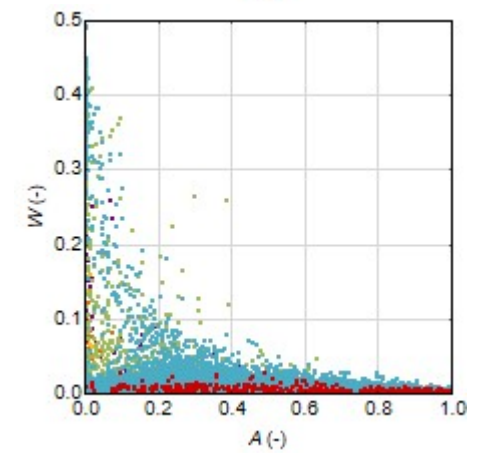
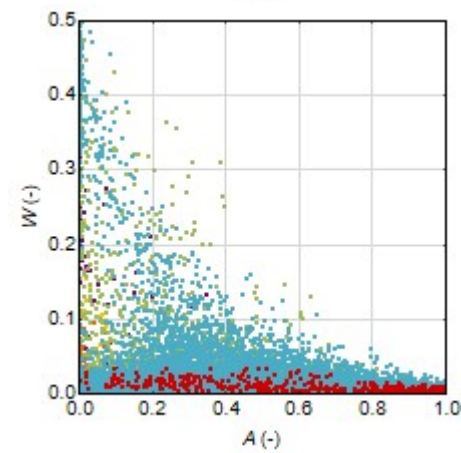
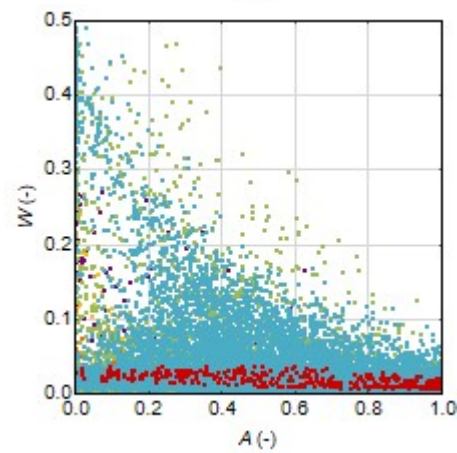
S_{wc}  W 

Figure S6. Scatterplots of simulated S_{wc} (top) and W (bottom) against ice concentration A for the polynya from 19 Sep. 2019. Colors show different wind speed classes (legend to the right; in m/s). Note different scales on the y axes in the top plots. Note also that no results for S0 are shown as in this case $A = 0$ everywhere.

- $U_w \leq 10$
- $10 < U_w \leq 15$
- $15 < U_w \leq 20$
- $20 < U_w \leq 25$
- $25 < U_w \leq 30$
- $30 < U_w \leq 35$
- $U_w > 35$

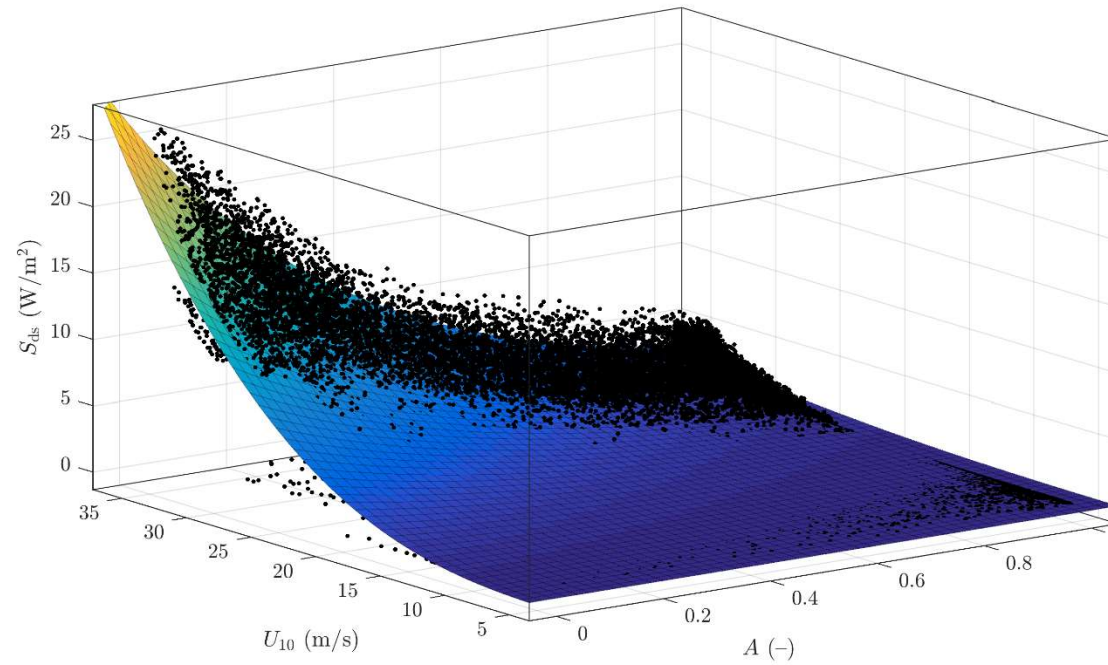


Figure S7. Scatterplot of simulated S_{ds} against ice concentration A and wind speed U_{10} , for the polynya from 19.09.2019 (model setupS2_f5). Black dots are modelling results, color surface shows the least-square fit of the function $S_{ds} = a(d-A)^b U_{10}^c$. The fitted coefficients are $a = 5 \cdot 10^{-9}$, $b = 8.55$, $c = 2.88$ and $d = 4.07$. The correlation coefficient between the fitted and original values equals 0.87 and the root-mean-square error 1.3 W/m².